

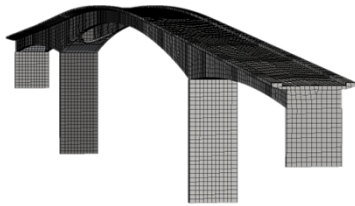
Amna Gonilovic
Simen Steinkjer Løken

Capacity Analysis of Herøysund Bridge with a Damaged Post- Tensioned System

Master's thesis in Civil and Environmental Engineering
Supervisor: Daniel Cantero
June 2023

Amna Gonilovic
Simen Steinkjer Løken

Capacity Analysis of Herøysund Bridge with a Damaged Post-Tensioned System



Master's thesis in Civil and Environmental Engineering
Supervisor: Daniel Cantero
June 2023

Norwegian University of Science and Technology
Faculty of Engineering
Department of Structural Engineering



MASTER THESIS 2023

SUBJECT AREA: Structural engineering	DATE: 09.06.2023	NO. OF PAGES: 80 + 30 appendix
---	---------------------	-----------------------------------

TITLE:

Capacity Analysis of Herøysund Bridge with a Damaged Post-Tensioned System

Kapasitetsanalyse av Herøysund bru med skadet spennarming

BY:

Amna Gonilovic

Simen Steinkjer Løken



SUMMARY:

The aim of this master's thesis is to conduct a capacity analysis of Herøysund Bridge. The objectives include developing a detailed bridge model using a finite element software, determining its midsection capacity, and investigating the impact of a damaged post-tension system on its capacity. The capacity control is carried out in the ultimate limit state (ULS) using regulations and standards applicable at the time of this thesis. By pursuing these objectives, this study seeks to enhance the understanding of the bridge's capacity and provide valuable insights into the effects of a damaged post-tension system.

The finite element program DIANA was employed to extract the design load effects. A detailed model of Herøysund Bridge was developed in DIANA, followed by a linear static analysis to determine the load effects on the bridge. To account for the nonlinear behavior of concrete, the cross-sectional capacity calculations were performed separately using manual calculations. After evaluating the capacity of the bridge without damage, a parametric study was conducted by successively removing central tendons from the bridge model to observe the effects on its capacity.

The capacity assessment at the midsection of an undamaged bridge in the ULS revealed a design moment of 3 892 kNm and an ultimate moment of resistance of 13 254 kNm, resulting in a utilization ratio of 29.4%. Furthermore, the investigation of the post-tensioning system with damage demonstrated that it is possible to remove four tendons spanning through the midsection without compromising its capacity.

Consequently, it can be concluded that the bridge, in its healthy state, can withstand service class Bk 10/50. Moreover, the midsection is found to be highly over-dimensioned. This study also highlights the ease of including damages and the feasibility of streamlining damage state assessments through systematic digitization of the modelling and assessment process.

RESPONSIBLE TEACHER: Associate Professor Daniel Cantero

SUPERVISOR(S): Associate Professor Daniel Cantero

CARRIED OUT AT: Department of Structural Engineering

Abstract

Norway is currently faced with a significant challenge regarding its aging infrastructure, particularly concerning the approximately 17 000 national and county road bridges. Among these bridges, the early constructed post-tension concrete bridges have emerged as a notable concern due to evident signs of poor execution and subsequent damage caused by corrosion. Herøysund Bridge, constructed in the late 1960s, serves as a prominent example, exhibiting significant corrosion damage in its post-tension system. Consequently, it has been determined that the current bridge must be dismantled, and construction of a new bridge has already commenced at the time of this thesis. As part of a broader initiative to extend the service life of such bridges, this research project focusing on Herøysund Bridge represents a dedicated effort to achieve this objective.

The aim of this master's thesis is to conduct a capacity analysis of Herøysund Bridge. The objectives include developing a detailed bridge model using a finite element software, determining its midsection capacity, and investigating the impact of a damaged post-tension system on its capacity. The capacity control is carried out in the ultimate limit state (ULS) using regulations and standards applicable at the time of this thesis. By pursuing these objectives, this study seeks to enhance the understanding of the bridge's capacity and provide valuable insights into the effects of a damaged post-tension system.

The finite element program DIANA was employed to extract the design load effects. To ensure the development of an accurate and detailed bridge model, an initial literature study and data collection were conducted. Subsequently, a comprehensive familiarization with the DIANA software was undertaken to ensure its effective utilization. With a thorough understanding of DIANA, a detailed model of Herøysund Bridge was developed, followed by a linear static analysis to determine the load effects on the bridge.

To account for the nonlinear behavior of concrete, the cross-sectional capacity calculations were performed separately using manual calculations. Firstly, the midsection of the undamaged bridge was evaluated in the ULS. Subsequently, a parametric study was conducted by successively removing central tendons from the bridge model to observe the effects on its capacity.

The capacity assessment at the midsection of an undamaged bridge in the ULS revealed a design moment of 3 892 kNm and an ultimate moment of resistance of 13 254 kNm, resulting in a utilization ratio of 29.4%. Furthermore, the investigation of the post-tensioning system with damage demonstrated that it is possible to remove four tendons spanning through the midsection without compromising its capacity.

Consequently, it can be concluded that the bridge, in its healthy state, can withstand service class Bk 10/50. Moreover, the midsection is found to be significantly over-dimensioned, as the removal of 50% of the tendons spanning through the midsection still provides sufficient capacity. It is further emphasized that the development of a detailed model incorporating damages is crucial for accurately assessing the service life of an existing bridge. This study highlights the ease of including damages and the feasibility of streamlining damage state assessments through systematic digitization of the modeling and assessment process, as exemplified by the implementation of Python scripting in this project.

Sammendrag

Norge står for øyeblikket overfor en betydelig utfordring når det gjelder sin aldrende infrastruktur, spesielt med tanke på de omtrent 17 000 broene på riks- og fylkesvegnettet. Blant disse broene er de eldre etteroppspente betongbruene blitt et bemerkelsesverdig bekymringsområde på grunn av tydelige tegn på dårlig utførelse og påfølgende skader forårsaket av korrosjon. Herøysund bru, som ble bygget på slutten av 1960-tallet, er et fremtredende eksempel på dette med omfattende korrosjon på spennarmeringen. Herav skal nåværende bro rives, og arbeidet med bygging av ny bro er i startfasen mens arbeidet med denne masteroppgaven pågår. Som en del av et større initiativ for å forlenge levetiden til eksisterende infrastruktur, representerer dette forskningsprosjektet, som fokuserer på Herøysund bru, en dedikert innsats for å oppnå dette målet.

Målet med denne masteroppgaven er å utføre en kapasitetsvurdering av Herøysund bru. Dette ble gjort ved å utvikle en detaljert bromodell i et elementprogram, regne ut broens momentkapasitet i midtseksjonen og til slutt undersøke virkningen av skader på spennarmeringen på broens kapasitet. Kapasitetskontrollen er utført i bruddgrensetilsand (ULS) ved hjelp av manualer og standarder som gjelder på tidspunktet for denne oppgaven. Dette gjøres for å forbedre forståelsen av broens kapasitet og gi innsikt i effektene av et skadet etteroppspent system.

Elementmetodeprogrammet DIANA er brukt til å beregne dimensjonerende lastvirkning. For å produsere en nøyaktig og detaljert brumodell, ble det først gjennomført et litteraturstudie. Deretter ble det gjennomført en omfattende innføring i DIANA for å sørge for riktig bruk av programvaren, spesielt med tanke på forspenning. Med god forståelse for programvaren ble det utviklet en presis modell av Herøysund bru. Deretter ble det utført en lineær analyse for å bestemme dimensjonerende lastvirkning.

For å ta hensyn til betongens ikke-lineære oppførsel, ble kapasitetsberegningene for tverrsnittet utført separat ved håndberegninger. Bruens midtseksjon i uskadet tilstand ble evaluert i bruddgrensetilstand, før en parametrisk studie på skadet bru ble utført. Skadene ble simulert ved at spennarmeringskablene, en etter en, ble fjernet fra bromodellen for å registrere effektene på bruens kapasitet.

Kapasitetsvurderingen av midtseksjonen i uskadet tilstand ga et dimensjonerende moment på 3 892 kNm og en momentkapasitet på 13 254 kNm. Dette resulterer i en utnyttelsesgrad på 29,4%. Videre viste undersøkelsen omhandlende skadet spennarmering at det er mulig å fjerne fire kabler som strekker seg gjennom midtseksjonen uten å overstige kapasiteten.

Følgelig kan det konkluderes med at bruene, i sin uskadde tilstand, tåler bruksklasse Bk 10/50. Dessuten er midtseksjonen betydelig overdimensjonert, ettersom fjerning av 50% av kablene fortsatt gir tilstrekkelig kapasitet. Det understrekes også at utviklingen av en detaljert modell som inkluderer skader, en digital tvilling, med andre ord, er vesentlig for å vurdere levetiden til en eksisterende bru nøyaktig. Dette studiet viser hvor enkelt det er å inkludere defekter, samt gjennomførbarheten av en effektivisering av skadevurdering, gjennom systematisk digitalisering av modellerings- og vurderingsprosessen. Dette er demonstrert gjennom implementeringen av Python-scripting i dette arbeidet.

Preface

This master's thesis represents the culmination of our five-year-long master's degree program at the Norwegian University of Science and Technology (NTNU). Over a period of 20 weeks in the spring of 2023, we, Amna Gonilovic and Simen Steinkjer Løken, collaborated on this thesis under the supervision of Associate Professor Daniel Cantero from the Department of Structural Engineering (KT).

Undertaking this thesis has been an enriching journey, filled with challenges and rewards. It has broadened our perspectives and deepened our appreciation for the field of structural engineering. Our work aligns with a larger project focused on extending the service life of bridges, giving us a strong sense of purpose and fulfillment.

We were driven to explore this subject for our thesis due to our fascination with bridge engineering. Throughout this project, our goals were to expand our knowledge and gain practical experience in utilizing finite element programs. The opportunity to employ Python programming in our research was particularly enticing, allowing us to explore innovative approaches.

By presenting this thesis, we aim to contribute to the advancement of bridge engineering practices and promote sustainable infrastructure management.

Acknowledgments

Throughout the course of this master's thesis, we have been fortunate to receive guidance and support from various individuals.

First and foremost, we would like to express our sincere gratitude to our supervisor, Daniel Cantero. His unwavering guidance, regular meetings, and dedicated support have been invaluable throughout this research. We are especially grateful for his efforts in fostering collaboration among different master's theses, allowing us to exchange insights, discoveries, and provide assistance with DIANA.

We would also like to acknowledge the contributions of Professor Terje Kanstad. His continuous availability and valuable assistance in addressing our academic inquiries have greatly enriched our research. His guidance and expertise have played a significant role in shaping the depth and quality of our work. Additionally, we are grateful to Professor Roy Johnsen for providing insightful information on the bridge damages, which has further enhanced our understanding and analysis.

Special thanks go to Håvard Johansen for his assistance and meticulous review of bridge loads. His guidance in understanding traffic loads, with a specific focus on the Norwegian Public Roads Administration's handbook V412, has significantly improved the quality of our work. We would also like to express our appreciation to Asmund Sveen for his support and for sharing essential information about the bridge. His willingness to explain his calculations for Herøysund Bridge has been instrumental in our work.

Furthermore, we are grateful to Per Ove Ravatsås for facilitating a memorable visit to Herøysund Bridge and Nordland County Municipality. The visit provided us with valuable perspectives and insights on the ongoing project.

Lastly, we would like to extend our thanks to our fellow students for engaging in meaningful discussions, which have contributed to our learning and development.

Trondheim, June 9, 2023



Anna Gonilovic



Simen Steinkjer Løken

Definitions

Abbreviations

Throughout this master's thesis, the following abbreviations have been used consistently:

- NS-EN 1992-1-1:2004 is referred to as Eurocode 2.
- The DIANA FEA software, version 10.6, developed by DIANA FEA BV, is referred to as DIANA.
- “Håndbok V412 - Bæreevneklassifisering av bruer, laster” and “Håndbok V413 - Bæreevneklassifisering av bruer, materialer” are referred to as V412 and V413 respectively.
- A calculation report was published on 09.11.2020 dealing with a load-bearing capacity assessment of Herøysund Bridge that was conducted by Asmund Sveen for Aas-Jakobsen AS. This report is referred to as Report A.J. 2020.

Concept Translations

Norwegian manuals have been used for load definition, among other things, and consequently, Norwegian concepts have had to be translated into English. The following Norwegian-English translations are undertaken:

bruksklasse	service class
føringsavstand	notional lane distance

Sign conventions

The same sign conventions used as standard in DIANA are used in this thesis:

- Tensile stresses and tensile forces are defined as positive.
- Bending moments that induce tension in the upper part of the superstructure are designated as positive. Note that this is opposite from Report A.J. 2020.
- Displacements are defined as positive when occurring in the same direction as the axes, indicating movement along the respective axes.

DIANA manual references

The pages that follow make use of the DIANA Manual, which has been cited in the format of (Reference, DIANA version, Chapter). For instance, (DIANA FEA_{BV}, 2022, 10.6, 10.1.3) refers to Chapter 10.1.3 of DIANA's User Manual version 10.6.

Symbols

Symbols and their corresponding definitions are in accordance with Eurocode 2. The following list defines symbols utilized throughout the main text, while symbols exclusively used in the appendix are defined within their respective sections.

Latin

A_p	Area of a prestressing tendon or tendons
b	Width
b_{eff}	Effective flange width
d	Effective depth of a cross-section
e	Eccentricity
E_{cm}	Secant modulus of elasticity of concrete
$E_{cm,0}$	Secant modulus of elasticity of concrete at the instant in time of first loading
$E_{c,eff}$	Effective modulus of elasticity of concrete
E_{middel}	Middle modulus of elasticity
E_p	Design value of modulus of elasticity of prestressing steel
E_s	Design value of modulus of elasticity of reinforcing steel
f_{cd}	Design value of concrete compressive strength
f_{ck}	Characteristic compressive cylinder strength of concrete at 28 days
f_{yk}	Characteristic yield strength of reinforcement
f_{pd}	Design tensile strength of prestressing steel (??)
f_{pk}	Characteristic tensile strength of prestressing steel
$f_{p0.2k}$	Characteristic 0,2% proof-stress of prestressing steel
$f_{p0.1k}$	Characteristic 0,1% proof-stress of prestressing steel
h	Element size
h_0	Effective cross-section thickness
k	Wobble parameter
k_h	Coefficient dependent on h_0
l_0	Distance between points of zero moments
M	Bending moment
M_{Ed}	Design bending moment
M_{Rd}	Bending moment capacity
n	Number of elements
P	Prestressing force
P_{max}	Maximum prestress force
P_{m0}	Prestress force at transfer
$P_{m,t}$	Effective prestress force
t	Thickness, Time being considered
t_0	The age of concrete at the time of loading
t_s	The age of concrete at the beginning of drying shrinkage
T	Temperature
x, y, z	Coordinates

Greek

α	Linear coefficient of thermal expansion
α_{cc}	Coefficient
$\beta_{d,s}(t, t_s)$	Function describing the drying shrinkage development with time
γ_c	Partial factor for concrete
γ_s	Partial factor for reinforcing or prestressing steel

ε	Strain
ε_{ca}	Autogenous shrinkage strain
ε_{cd}	Drying shrinkage strain
ε_{cs}	Total shrinkage strain
θ	Angle
μ	Friction coefficient, coefficient
ρ_{1000}	Relaxation loss in percentage at 1000 hours after tensioning
σ	Stress
σ_{cd}	Design compressive stress in concrete
σ_{pi}	Stress in post-tensioned tendon immediately after anchoring
$\Delta\sigma_{pr}$	Loss of stress in tendon due to relaxation
ϕ	Diameter of a reinforcing bar or a prestressing duct
φ	Creep coefficient

Table of Contents

Abstract	i
Sammendrag	ii
Preface	iii
Acknowledgments	iv
Definitions	v
Symbols	vii
1 Introduction	1
1.1 Background and Context	1
1.2 The Research Problem and Objectives	1
1.3 Methodology	2
1.4 The Structure	3
2 Theory	4
2.1 Post-Tensioning	4
2.2 Losses of Prestress	4
2.2.1 Elastic Deformation Losses	4
2.2.2 Friction Along the Tendon	5
2.2.3 Anchorage Losses	5
2.2.4 Time-Dependent Losses	6
2.3 Corrosion of Prestressed Reinforcing Steel	7
2.3.1 Corrosion of Steel in Concrete in General	7
2.3.2 Carbonation	7
2.3.3 The Effect of Chloride Ions	8
2.3.4 Voids	8
2.3.5 Stress Corrosion Cracking and Hydrogen Embrittlement	8
2.4 Modelling in DIANA	9
2.4.1 Finite Element Method	9
2.4.2 Modelling of Reinforcement	9

2.4.3	Mesh Order	10
3	Herøysund Bridge	11
3.1	Geometry	12
3.1.1	The Concrete Structure	12
3.1.2	Passive Reinforcement	13
3.1.3	Active Reinforcement	14
3.2	The Construction Process	16
3.3	Materials	16
3.3.1	Concrete	17
3.3.2	Passive Reinforcement	17
3.3.3	Active Reinforcement	18
3.4	Damages	18
3.5	Measures	20
4	Loads	21
4.1	Permanent Loads	21
4.2	Variable Loads	21
4.2.1	Traffic Load	21
4.2.1.1	Vertical Forces	22
4.2.1.2	Horizontal Forces	24
4.2.2	Thermal Actions	24
4.2.3	Wind Load	25
4.3	Deformation Loads	25
4.3.1	Creep	25
4.3.2	Shrinkage	26
4.3.3	Steel Relaxation	27
4.3.4	Prestressing Force	28
4.4	Design Load Combinations in ULS	29
5	Exploring Relevant Methods in DIANA Modelling	30
5.1	Composed Line Elements	30
5.2	Losses due to Friction	32
5.2.1	Including Angular Deviations Through the Wobble Factor	33

5.3	Phased Construction Analysis	35
6	Modelling Herøysund Bridge in DIANA	36
6.1	Reference System and Reference Line	36
6.2	Geometry	37
6.2.1	The Concrete Structure	37
6.2.2	Passive Reinforcement	38
6.2.3	Active Reinforcement	39
6.3	Properties	40
6.3.1	The Concrete Structure	40
6.3.2	Reinforcement	41
6.4	Loads	41
6.4.1	Self-Weight	41
6.4.2	Creep and Shrinkage	42
6.4.3	Traffic Load	44
6.4.4	Post-Tension Load	44
6.4.5	The Design Load Combination	45
6.5	The Python Script for the Post-Tensioning System	45
6.6	Boundary Conditions	47
6.7	Meshing	47
6.8	Post-Processing	50
7	Model Validation	52
7.1	Stage Construction Impact	52
7.2	Control of Model Results	52
7.2.1	Comparison with Measurements from Full-Scale Structural Testing	52
7.2.2	Comparison of Design Moments with Report A.J. 2020	55
8	ULS Capacity Assessment	58
8.1	Anlysis Results	58
8.2	Ultimate Moment of Resistance	58
8.3	Moment Capacity Assessment	60
9	Study of the Post-Tensioning System with Damage	62

9.1	Successive Tendon Breakages	63
9.1.1	Method	63
9.1.2	Results and Discussion	64
9.2	Refinement of the Damage Model	65
9.2.1	Method	65
9.2.2	Results	67
9.2.3	Exploratory Studies for Result Interpretation	70
9.2.3.1	Case 1 - Simply Supported	70
9.2.3.2	Case 2 - Three-Span Continuous Beam	71
9.2.3.3	Case 3 - Three-Span Continuous Beam Supported by Columns	73
9.2.3.4	Case 4 - Curved Tendon Layout	73
9.2.4	Discussion	74
10	Conclusion	76
11	Further Work	78
	Bibliography	79
	Appendix	I
A	Drawings	II
B	Cross-Section Parameters	XIII
C	Calculation of Loads	XIV
C.1	Calculation of the Shrinkage Strain	XV
C.2	Creep Effect	XVI
D	Calculation of Prestress Losses	XVII
D.1	Relaxation	XVIII
D.2	Elastic Shortening	XIX
E	Transfer of Prestress - Transmission Length	XX
F	Simple Beam - Cross-Section Forces	XXI
G	The Python Script for the Post-tensioning System	XXII
H	Reference System for the Post-Tensioning System	XXIX

1 Introduction

This master's thesis focuses on Herøysund Bridge, an infrastructure element within the broader research project titled *Green Management of Infrastructure Structures*. The bridge's deteriorating condition, particularly the severe damage to its post-tensioning system, necessitates an accurate study of its capacity and structural behaviour. By addressing the uncertainties associated with the bridge's capacity and the impact of damage on its design load effects, this research aims to provide valuable insights into the maintenance, rehabilitation, and management of ageing bridges. Through a combination of detailed modelling, capacity assessment, and analysis of damage scenarios, this study seeks to enhance our understanding of post-tensioned systems and contribute to the development of sustainable strategies for extending the service life of vital infrastructure.

1.1 Background and Context

In Norway, the ageing infrastructure poses a significant challenge, particularly with regard to the country's approximately 17 000 national and county road bridges. Many of these bridges are already 50 years old and exhibit substantial damages and deficiencies that can potentially lead to serious traffic incidents. Recent data from NRK in April 2022 highlights the alarming situation, indicating that the lack of maintenance puts the safety of around 5 600 bridges at risk (Siem, 2022). This pressing issue reflects the historic under-prioritization of infrastructure research in Norway (Staberg and Olaisen, 2022). However, Herøysund Bridge in Nordland serves as a significant case study within the broader research project titled *Green Management of Infrastructure Structures* (In Norwegian: Grønn forvaltning av konstruksjoner for infrastruktur).

The decision to construct a new bridge for Herøysund arose from a comprehensive condition assessment, which revealed severe damages to the prestressing reinforcement, compromising its structural integrity and safety. Nonetheless, insights from senior researcher Tor Arne Martius-Hammer from SINTEF emphasize that earlier and more robust condition assessments could have potentially prompted the consideration of rehabilitation rather than demolition and reconstruction. Such a shift in approach would have not only saved Nordland County Municipality at least 100 million NOK but also aligned with the project's overarching ambition of developing a model for the management, operation, and maintenance of concrete structures for infrastructure. The focus is on increasing the service life of existing structures, recognizing the cost-effective and environmentally friendly benefits of extending their lifespan (Brekkaus, 2023).

In addition to the financial advantages, extending the lifespan of existing structures carries significant environmental implications. By avoiding demolition and new construction, the project aims to minimize CO₂ emissions associated with the entire life cycle of infrastructure projects, including the energy-intensive processes of demolition, construction, and transportation. Consideration of these environmental aspects becomes particularly pertinent when contemplating the potential impact of Herøysund Bridge's rehabilitation, which could have prevented the emission of several thousand tons of CO₂ (Skoglund, 2022).

1.2 The Research Problem and Objectives

The research problem addressed in this study centres around the uncertainties associated with the capacity of Herøysund Bridge. The absence of original calculations and limited available information on the bridge's construction pose significant challenges. Furthermore, there is a lack of clarity on how design load effects and capacity are influenced by the bridge's state of damage.

The complexity is further amplified by the fact that Herøysund Bridge is a post-tensioned structure, where the grouting process holds critical importance during construction.

The research objectives of this study are defined as follows:

1. Develop a detailed model of Herøysund Bridge that incorporates accurate representations of its geometry, material properties, boundary conditions, and relevant loads. This detailed model will provide a reliable representation of the bridge's behaviour.
2. Determine the capacity of the bridge at its midsection. By evaluating the design moment against the section resistance, the study aims to quantify the bridge's capacity to withstand applied loads and assess its structural performance.
3. Investigate the impact of damage in the post-tensioning system on the design load effects and capacity of Herøysund Bridge. This investigation will involve developing and integrating damage models within the bridge model using finite element software. By incorporating these models, the study aims to explore how damage influences the bridge's structural behaviour, load-carrying capacity, and overall safety.

By addressing these research objectives, this study aims to significantly contribute to the understanding of Herøysund Bridge's behaviour, particularly with regard to its post-tensioned system. The findings will provide valuable insights into the bridge's capacity assessment.

1.3 Methodology

The methodology employed in this study involved several key steps to achieve a detailed analysis and assessment of Herøysund Bridge. These steps are outlined below:

1. **Data Collection:** To create an accurate model, relevant information about Herøysund Bridge was collected. This included gathering drawings, calculation basis, inspection logs, and other pertinent reports. Additionally, a literature study was conducted to review old standards and regulations.
2. **Familiarization with Analysis Program:** Before modelling, an exploration of the DIANA analysis program was undertaken. This included acquiring knowledge about finite element modelling principles in general. Understanding the capabilities and functionalities of DIANA allowed for the appropriate application of the software in this study.
3. **Model Development in DIANA:** The next step involved modelling Herøysund Bridge using DIANA. A thorough investigation and understanding of the modelling approach for post-tensioned systems within DIANA were undertaken. This encompassed exploring various possibilities and configurations available for accurately representing the bridge's post-tensioned system.
4. **Cross-Sectional Capacity Calculation:** To facilitate an accurate capacity assessment, the cross-sectional capacity of the bridge was calculated manually. This involved applying established engineering principles and calculations, like accounting for the nonlinear behaviour of concrete through design code procedures, to determine the capacity of the bridge at the midsection.
5. **Investigation of Damage Impact:** In order to investigate the impact of corrosion damage, fundamental knowledge of corrosion and its effects on post-tensioned systems were acquired.

1.4 The Structure

The assignment consists of 11 chapters that have been organized in a logical and coherent sequence, reflecting the natural progression of the research. The following overview provides a concise outline of each chapter, highlighting the key topics and objectives covered in the thesis:

Chapter 2 focuses on presenting highly relevant theoretical concepts that underpin the analysis and assessment of Herøysund Bridge.

Chapter 3 provides detailed information about the bridge's geometry, reinforcement, construction process, material specifications, and inspected damages.

Chapter 4 defines the relevant loads, encompassing permanent loads, variable loads, and deformation loads.

Chapter 5 explores the use of Composed Line Elements, DIANA's handling of prestress losses due to friction, and the significance of performing Phased Construction Analysis.

Chapter 6 describes the process of modelling Herøysund Bridge using a combination of Python scripting and DIANA's interface.

Chapter 7 focuses on validating the DIANA analysis by comparing results with field tests and a previous study on the bridge's capacity.

Chapter 8 presents the results of a static linear analysis in DIANA of Herøysund Bridge in its intact state, providing an assessment of its capacity under ultimate limit state conditions.

Chapter 9 delves into the behaviour of the bridge when subjected to damage in the post-tensioning system. It describes the development and analysis of various damage models within DIANA, focusing on the bridge's capacity at the midsection under successive tendon breakages and the effects of induced damages at different positions along a specific tendon.

Chapter 10 summarizes the main findings, highlights the contributions of the study, and discusses their implications.

Chapter 11 provides recommendations for future research.

2 Theory

2.1 Post-Tensioning

Post-tensioning represents one of the two methods utilized for prestressing concrete. The alternative method, known as pretensioning, is predominantly employed in factories equipped for producing precast concrete components. In post-tensioning, the concrete is first cast and allowed to harden before the prestressing steel is tensioned and anchored. This is possible when the concrete is cast with a duct surrounding the prestressing steel. By employing this technique, the tendon's layout can be designed with a desired curvature, constrained solely by the elasticity of the steel. This gives the possibility to design the tendon layout to counteract the moments arising from the external loading. For large on-site construction projects like bridges and large frame structures, post-tensioning is typically the preferred choice (Sørensen, 2013). Following the tensioning process, it is customary to inject the ducts with a cement-based grout to ensure bonding between the grout and the duct, thereby creating a bonded system. This differs from an unbonded system, where no adhesion exists between the concrete and the prestressing steel. Proper grouting is crucial as it not only establishes the bond but also provides essential protection against corrosion for the prestressing steel. Inadequate workmanship or the use of low-quality grouting materials can result in severe corrosion damage.

2.2 Losses of Prestress

The prestressing force applied at the anchorage will decrease along the tendon length as well as with time. These losses of prestress are categorized as either *immediate* or *time-dependent* losses and are illustrated in Figure 1. Immediate losses occur when the tendons are prestressed and prestress is transferred to the concrete at time t_0 . Immediate losses are the difference between the force imposed on the tendon by the hydraulic prestressing jack P_{max} and the force in the tendon immediately after transfer at a distance x from the active end of the tendon $P_{m0}(x)$. Subsequently, time-dependent losses come into play, which are the gradual losses that occur with time over the service life of the member (Gilbert, Mickleborough, and Ranzi, 2017).

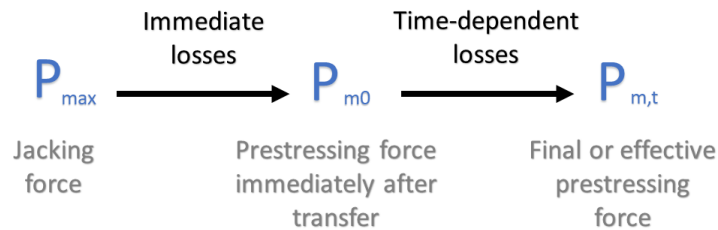


Figure 1: Prestress losses in the tendons (Gilbert, Mickleborough, and Ranzi, 2017).

In the following sections, anchorage set, friction, and elastic shortening will be explained in more detail, as they contribute to immediate losses. Moreover, the topic of time-dependent losses will be addressed.

2.2.1 Elastic Deformation Losses

In post-tensioned structures, the elastic deformation of the concrete occurs during the stressing operation, before the tendons are anchored. For members with a single tendon or multiple tendons

stressed simultaneously, there are no elastic shortening losses. However, in structures that contain multiple tendons and where the tendons are stressed sequentially, the stressing of a tendon leads to an elastic shortening loss in all previously stressed and anchored tendons. As a result, the first tendon to be stressed will experience the largest elastic shortening loss, and the last tendon to be stressed will experience no elastic shortening. Considering these elastic shortening losses is crucial in the design of post-tensioned structures to ensure their long-term durability and stability.

Calculating elastic shortening losses in an individual tendon of a post-tensioned structure can be a straightforward process when the stressing sequence is known. In most cases, determining the average loss of stress can be sufficient, and it can be calculated using the following equation:

$$\Delta\sigma_p = \frac{n-1}{2n} \frac{E_p}{E_{cm,0}} \frac{P}{A} \quad (1)$$

where n is the number of tendons, $E_{cm,0}$ is the secant modulus of elasticity of concrete at the instant in time of first loading, and P/A is the average concrete compressive stress (Gilbert, Mickleborough, and Ranzi, 2017).

2.2.2 Friction Along the Tendon

Friction is generated between the tendon and the duct during stressing operation in a post-tensioned member, causing a gradual reduction in force with the distance along the tendon x from the jacking end. This phenomenon is illustrated in Figure 2. The friction consists of a part due to the curvature of the tendon and another part due to local irregularities, also known as the wobble effect. An estimation of the prestress loss in the tendon at any distance x from the active end may be made using:

$$\Delta P_\mu(x) = P_{max} \cdot (1 - e^{-\mu(\theta+k \cdot x)}) \quad (2)$$

where θ represents the sum of the absolute values of angular deviations over the tendon length x . During construction, it is therefore important to ensure that the cable profile matches the one assumed in the design. The coefficient of friction μ depends on various factors, including the surface characteristics of the tendon and the duct, the presence of rust on the tendon's surface, and the elongation of the tendon. Eurocode 2 states that the value for μ shall be given in a European Technical Approval (ETA), but in the absence of this data, the values in Table 5.1 in Eurocode 2 may be assumed. Furthermore, the factor k represents the unintentional angular deviation per unit length due to wobble effects in both straight and curved segments of internal tendons. The value of k , also known as the wobble factor, depends on the rigidity of the sheaths, the spacing and fixing of their supports, the precision of tendon placement, the stiffness of the cables, and the precautions taken throughout the construction process. Like the friction coefficient, k shall be specified in an ETA. If ETA is absent, Eurocode 2 suggests that for internal tendons k will be in the range of $0.005 < k < 0.01$ per meter.

2.2.3 Anchorage Losses

Some slip or draw-in occurs during the transfer of the prestressing force from the jack to the anchorage, resulting in an additional loss of prestress. This loss is illustrated in Figure 2, where $P_{anchorage}$ represents the force in the anchorage after live end seating. The magnitude of the slip depends on the type of anchorage used, and the loss of prestress caused by the slip decreases with

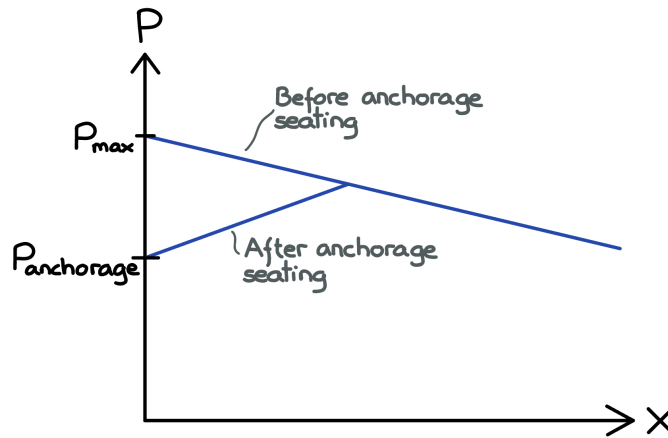


Figure 2: Friction reduces force as distance increases from the live end, as well as helping to offset seating losses.

the distance from the anchorage due to frictional resistance along the tendon. For longer tendons, this loss may be insignificant at the critical design section, but for shorter tendons, this loss can be significant and should not be ignored during the design phase. The prestressing loss due to wedge draw-in can be calculated if the magnitude of the draw-in is known, which is typically specified in the technical specifications for a particular system.

2.2.4 Time-Dependent Losses

Over time, the prestressing force in a member is expected to decline due to the effects of shrinkage and creep in the concrete, as well as the relaxation of the tendons. Creep and shrinkage cause gradual shortening of a concrete member, resulting in a reduction in the length of the prestressing steel that is physically connected to the concrete through either bond or anchorages at the tendon ends. The extent of this shortening can often be notable, leading to a decrease in stress levels in the steel, typically ranging from 150 to 300 MPa.

Furthermore, creep in the highly stressed prestressing steel causes an additional loss of stress through relaxation. Relaxation refers to the gradual loss of stress in a prestressing steel specimen that is stretched and held at a constant length, resulting from the development of creep strain in the steel, which manifests as a loss of elastic strain. Creep, and hence relaxation, is significantly influenced by the stress level and exhibits an increasing rate of increase as the stress level rises. Temperature increase also leads to a notable increase in relaxation.

Various methods exist for assessing the effects of concrete creep, shrinkage, and tendon relaxation on the long-term stresses of a prestressed cross-section. While Paragraph 5.10.6 in Eurocode 2 presents a simplified approach considering the dependencies of these phenomena, the book “Design of Prestressed Concrete to Eurocode 2” (Gilbert, Mickleborough, and Ranzi, 2017) claims that the approximate procedure specified in Eurocode may yield inaccurate and occasionally misleading results. This is because the method fails to adequately account for the significant loss of precompression in the concrete that occurs when non-prestressed reinforcement is present. Therefore, the book presents a realistic alternative estimation of the time-dependent losses of prestress in the tendon, including the redistribution of stresses between the bonded reinforcement and the concrete.”

2.3 Corrosion of Prestressed Reinforcing Steel

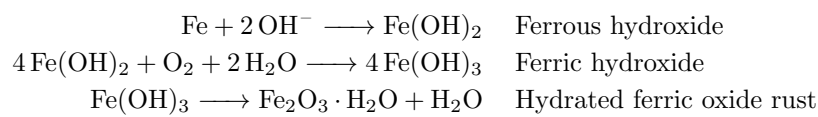
2.3.1 Corrosion of Steel in Concrete in General

Corrosion of steel reinforcement is a multistep process that is initiated at the interface between the steel bars and concrete mixture. It can be described by electrochemical reactions where the anodic reaction is the oxidation of iron, and the cathodic reaction is oxygen reduction (Ahlström, 2015).

The anodic reaction, meaning it is electron-producing: $2\text{Fe} \longrightarrow 2\text{Fe}^{2+} + 4\text{e}^{-}$

The cathodic reaction, i.e., electron-consuming: $\text{O}_2 + 2\text{H}_2\text{O} + 4\text{e}^{-} \longrightarrow 4\text{OH}^{-}$

As can be observed from the reaction equation above, the process is largely dependent on the availability of water and oxygen at the steel-concrete interface. Johnsen (2022) represents several subsequent reaction steps that can happen leading to the formation of corrosion product, or rather, rust:



Rust has a greater volume than iron, which can lead to cracking and spalling of the concrete. Figure 3 shows an electrochemical cell and illustrates the volume expansion, which is dependent on the type of corrosion product. The corrosion product in the figure requires oxygen to be present in the reaction.

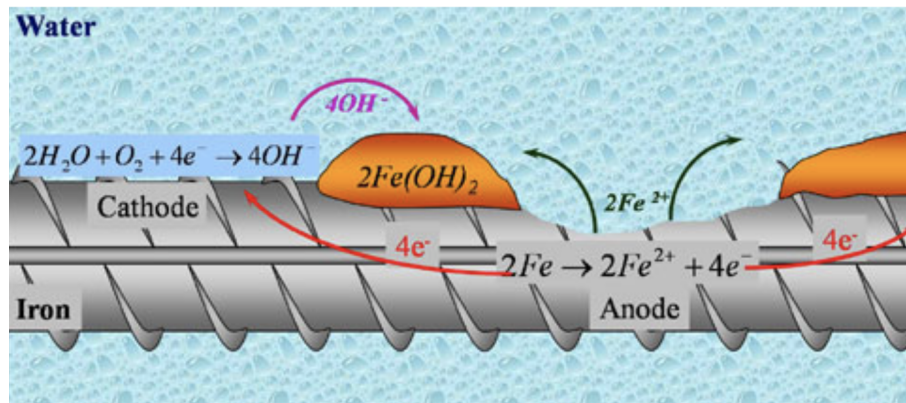


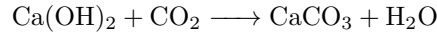
Figure 3: An electrochemical cell where the reactions occur simultaneously at different areas on the steel surface, called anodic and cathodic areas (PCA, 2023).

Reinforcement in concrete is normally protected by a dense passive film that forms due to the high pH level in the pore water solution, making the corrosion rate low. Concrete is naturally in a passive state when the pH is in the range of 13-14. The passive layer can have different chemical compositions but is primarily composed of iron oxides and hydroxides. Corrosion of steel reinforcement is induced either by carbonation or by chlorides.

2.3.2 Carbonation

Carbon dioxide (CO_2) accounts for approximately 0.04% of the composition of air. Carbonation occurs when CO_2 infiltrates the surface of concrete through the dry regions of interconnected pores

within the concrete microstructure and dissolves in the pore water. In the presence of calcium hydroxide in the pore water, a reaction takes place with carbon dioxide, resulting in the formation of calcium carbonate and water (Fuhaid and Niaz, 2022):



This process reduces the pH of the pore water to a level below 10, which is where carbon steel loses its passivity. Once the carbonation process reaches the steel within the concrete, the protective passive layer on the reinforcement surface breaks down due to the lowered pH, and active corrosion begins. The rate of carbonation is influenced by various factors, including the thickness and density of the concrete cover, the moisture content within the concrete, and the temperature.”

2.3.3 The Effect of Chloride Ions

Similar to the contribution of carbonation to corrosion, chloride corrosion diminishes passivity and disrupts the passive layer. This occurs because pore water containing dissolved chloride ions (Cl^-) in direct contact with the reinforcement can chemically react with the passive film. Chloride ions can either exist freely in the pore water or be bound to the concrete material. While chloride-containing constituent materials like seawater were used in the past, their usage is now prohibited. Therefore, a higher (or increasing) chloride content in concrete structures built in recent times is typically due to chlorides penetrating from the surrounding environment. Examples of chloride-containing environments include marine environments or areas where road salt is used.

Unlike corrosion induced by carbonation, which is characterized by uniform corrosion on the surface of the reinforcement, chloride-induced corrosion attacks localized areas and eventually leads to the formation of pits. This type of corrosion is known as pitting corrosion.

2.3.4 Voids

Portions of bonded post-tensioned tendons may inadvertently remain ungrouted during construction, resulting in the formation of substantial void spaces that can expose steel strands for extended periods. Additionally, water precipitation during casting, as well as subsequent re-absorption and/or evaporation from the injection mass, can lead to the formation of substantial voids. These voids typically have a larger volume than the pores, potentially creating an area where steel is highly susceptible to severe corrosion. Corrosion becomes probable as the voids become exposed to atmospheric conditions, with moisture, oxygen, and contaminants such as chloride ions and sulfate ions permeating the voids. A moisture film of adequate thickness acts as an electrolyte for electrochemical reactions, thus playing a crucial role in initiating the corrosion process. Significant corrosion is observed when the relative humidity level exceeds 75% ($\text{RH} > 75\%$) (Lau and Lasa, 2016).

2.3.5 Stress Corrosion Cracking and Hydrogen Embrittlement

Stress Corrosion Cracking (SCC) refers to the formation and propagation of cracks in typically ductile metal alloys when they are subjected to tensile stresses in a corrosive environment. SCC commonly exhibits rapid progression and results in sudden, brittle failure of high-strength steel wires.

Hydrogen Embrittlement (HE) is another brittle failure mechanism that, similar to SCC, necessitates the presence of three conditions: i) a material susceptible to hydrogen embrittlement, ii)

the presence of tensile stresses, and iii) the existence of hydrogen within the material. HE refers to the reduction in ductility of the steel wire caused by the absorption of hydrogen. The presence of hydrogen atoms weakens the metallic lattice bonds. Hydrogen can result from corrosion or be introduced into high-strength steel during the manufacturing process, for example.

2.4 Modelling in DIANA

DIANA is a finite element software specifically designed for advanced structural analysis and simulation. It is widely used in the field of civil and structural engineering to analyze and predict the behaviour of structures under various loading conditions. When dealing with post-tensioned concrete structures, it is particularly effective.

2.4.1 Finite Element Method

The Finite Element Method (FEM) is a numerical approach used for solving field problems, also known as Finite Element Analysis (FEA). This method divides an object into finite elements and connects them at nodes. By employing this technique, structural engineers can model and compute complex physical structures that are difficult or impossible to solve analytically or by traditional methods. Before utilizing FEM tools, it is crucial to have a solid understanding of the method. As mentioned by Cook et al. (2001), using the program without sufficient knowledge can lead to undesirable consequences, ranging from embarrassing mistakes to disastrous outcomes.

The process of dividing an object into finite elements is called meshing. When performing meshing, it is important to consider the type and size of elements to use. Generally, a more refined mesh with smaller elements tends to improve the solution. However, during the course of this project thesis, it was discovered that not every problem can be solved solely by refining the mesh.

2.4.2 Modelling of Reinforcement

As described by Pinto and Cantero (2022), DIANA offers two different modelling options for reinforcement. Both methods can be used to replicate bonded and unbonded post-tension systems. However, modelling a damaged or partially grouted system is more complex using either approach.

The first and simplest method is known as embedded reinforcement. This method is commonly used for modelling global systems and is recommended due to its simplicity. The user models simple lines representing the reinforcement, and the program identifies the intersections of these lines with the surrounding elements, as illustrated in Figure 4. These intersecting elements, referred to as “mother elements,” are updated with improved stiffness and modal loading when prestress is applied. In this method, the reinforcement is fully embedded within the elements and does not have separate degrees of freedom (DOFs). The reinforcement strain is computed based on its associated mother element. It is important to note that this method assumes bonding between the reinforcement and the surrounding material in the actual structure.

In DIANA, the user has the flexibility to choose whether the embedded reinforcement is bonded to the mother element or not (DIANA FEA_{BV}, 2022, 10.6, 39.1). For modelling a grouted post-tension system, the load must be applied before the tendons are bonded to the surrounding concrete. If the tendons are bonded to the concrete prior to applying the load, the force acts on a restricted tendon that cannot move freely. This limitation in the modelling approach is further discussed by Musach (2020) in their Bachelor’s thesis. To simplify the modelling of a bonded system, one can disregard the bond between the steel and concrete and model the tendons as unbonded. Although

this approach does not precisely represent reality, H. Vestad and M. Vestad (2021) concluded that there is little difference in the structural behaviour between an unbonded and a bonded system, with identical behaviour observed until the point of cracking.

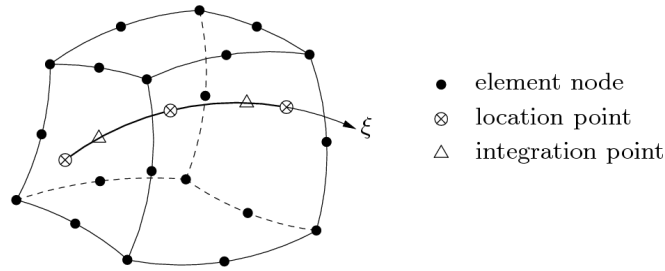


Figure 4: Embedded bar reinforcement in solid mother element (DIANA FEA_{BV}, 2022, 10.6, 39.1, Figure 39.10).

The second method of modelling reinforcement is bond-slip reinforcement. This approach simplifies the modelling of discrete reinforcement. The user can model simple lines representing the reinforcement, similar to the embedded method, and the program converts them into discrete reinforcement elements. These elements are connected to the surrounding elements using interface elements, as visualized in Figure 5. The benefit of this method is the ability to model the detailed behaviour of the reinforcement, making it suitable for detailed bond-slip analysis.

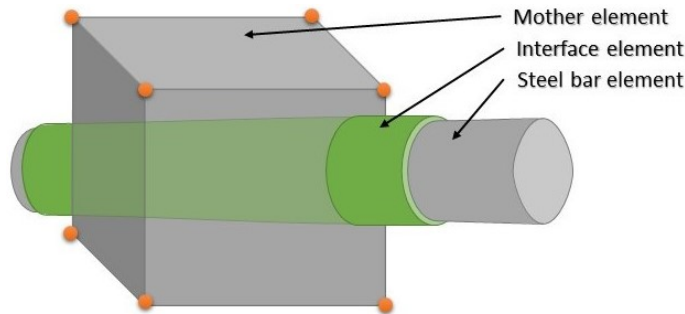


Figure 5: Bond-slip reinforcement in a solid element.

2.4.3 Mesh Order

When creating a finite element model in DIANA, the choice of mesh order is important. It can be either linear or quadratic, describing whether the elements are to be created without or with mid-side nodes, respectively. Including mid-side nodes will increase the number of degrees of freedom in the model. While linear meshing suffices for shapes with no curvature, concave and convex shapes require quadratic meshing to accurately represent the curvature. In quadratic meshing, additional side nodes are inserted between existing nodes, enabling the elements to have curved sides. It is still a serendipity element, as the nodes are placed on the boundary of the element, and there are no internal nodes (Cook et al., 2001). In DIANA, the mid-side location within quadratic elements can be determined either through linear interpolation or on shape (DIANA FEA_{BV}, 2022, 10.6, 10.1).

3 Herøysund Bridge

Herøysund Bridge, built in 1966, stands as one of the earliest examples of post-tensioned bridges constructed in Norway. The bridge is located in Nordland County Municipality and connects the islands “Sør-Herøy” and “Nord-Herøy”, which causes it to be subjected to a harsh coastal climate, as stated in Brutus. Figure 6 shows the location of Herøy, highlighting the exposed coastal location of the bridge.

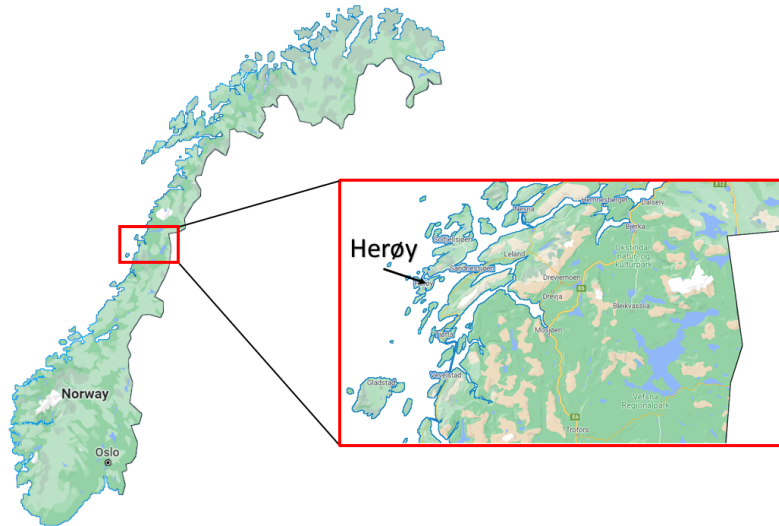


Figure 6: Map of Norway captured from Google Maps highlighting the location of Herøy.

The bridge is a cast-in-place concrete structure composed of five piers and two abutments with wing walls, spanning a total length of 154.5 m. The bridge’s axis numbering is defined to go from east (Nord-Herøy) to west (Sør-Herøy). As shown in Figure 7, the bridge comprises six spans, with a span division of 10.5 m, 30 m, 60 m, 30 m, 12 m, and 12 m. It has a one-lane carriageway and narrow pavements on both sides. The total width is 5.3 m, whereas the carriageway constitutes 4 m.

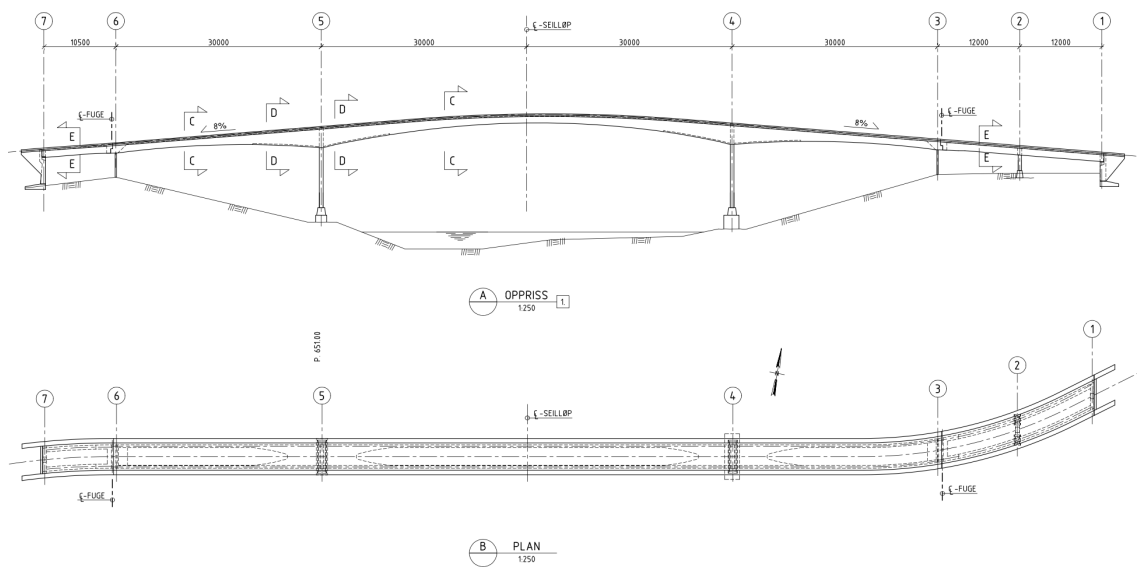


Figure 7: Side elevation and plan drawing of Herøysund Bridge.

The bridge superstructure is primarily designed as a girder bridge with two underlying beams. Towards the main piers in axis 4 and 5, the superstructure is designed as a box cross-section. The three longest spans, from axis 3 to 6, are prestressed with post-tensioning tendons, while the approach spans use conventional, passive reinforcement. The cross-section height, i.e. the distance between the bottom of the beam and the top slab surface, varies from 1.2 m for the approach spans and the middle of the main span, or rather, the midsection, to 3.0 m in the main pier areas. It is worth noting that the column bents and end abutments are founded on rock.

This master’s thesis focuses on the main part of the bridge, namely the main span of 60 m and the two adjacent side spans of 30 m. The reason for this is that the main part is subjected to the greatest loads and is post-tensioned. In addition, there are concrete corbels and joints at the transition between the side spans and the approach spans on both sides, which transfer horizontal forces in the longitudinal direction. In other words, there is no continuous concrete in this transition and in theory, no bending moments are transferred.

3.1 Geometry

The geometry of Herøysund Bridge is obtained from Brutus, which is the bridge database maintained by the Norwegian Public Roads Administration (NPRA). However, due to the bridge’s age, there is limited information available regarding many specific details. Therefore, this chapter presents the overall geometry of the bridge, derived from a combination of drawings, literature references, and expert discussions. Since this thesis primarily focuses on the main span and two side spans, which constitute the main part of the bridge, only the geometry of these sections is presented in this chapter and modelled. Relevant drawings can be found in Appendix A.

3.1.1 The Concrete Structure

Figure 8 displays the relevant bridge, including its associated piers. The cross-section of the bridge, as depicted in Figure 9, exhibits variations in both height and type. It primarily comprises a double T-girder cross-section but gradually transitions into a box girder configuration as it approaches axis 4 and 5.

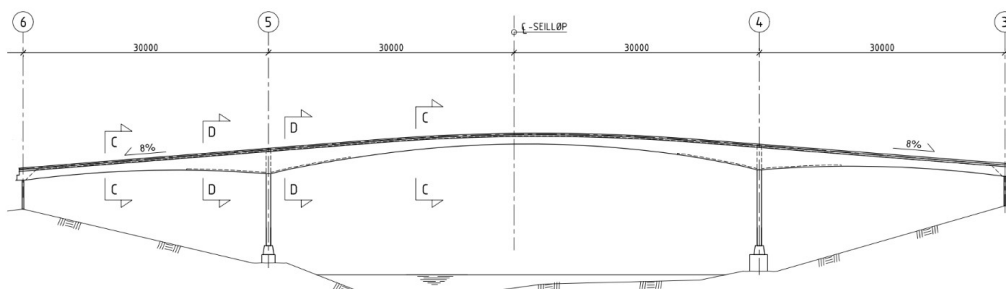


Figure 8: Drawing showing the relevant parts of Herøysund Bridge for this project.

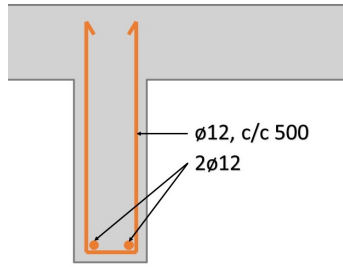


Figure 11: Beam reinforcement layout. Note that there are changes in c/c spacing near pier 4 and 5 to 150 mm

Although placement details of the main reinforcement in the transverse direction are lacking, Figure 12 illustrates what is assumed using schematic representations of the rebar shapes. It can be observed that this reinforcement includes stirrups encircling the longitudinal edge beam reinforcement and multiple rebars spanning the entire width.

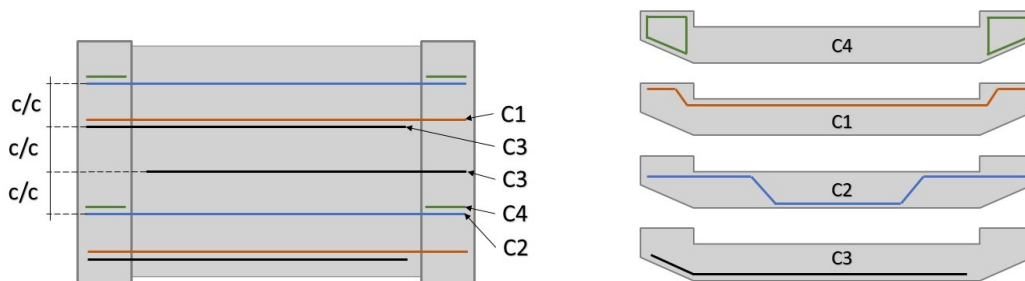


Figure 12: Layout of the bridge deck reinforcement in the transverse direction. c/c is either 100 or 120 mm, depending on the location in the bridge.

Additional reinforcement is incorporated in and around the piers. The piers are reinforced with longitudinal rebars, accompanied by shear reinforcement that surrounds the longitudinal rebars. Detailed illustrations of this reinforcement can be found in Drawing 4, 5, and 6 in Appendix A, providing a clear visual representation.

3.1.3 Active Reinforcement

The post-tensioning system of the bridge comprises four tendons in each beam, specifically, the north (N) and south (S) beam, and ten tendons in the bridge deck located above the supports. In addition to the prestressing reinforcement in the superstructure, two smaller tendons are placed in each of the piers at axis 4 and 5.

The post-tensioning cables utilized in Herøysund Bridge were supplied by AB Strängbetong and are of the BBRV type, which was one of the earliest and most reliable post-tensioning systems developed in Switzerland in 1944 (BBR, 2004). However, the BBRV technology is now outdated and has been replaced with a more modern and cost-effective concept called the barrel-wedge, which utilizes strands of 0.5" and 0.6" in diameter. A brochure for the prestressing reinforcement is provided in Brutus, and cable type 644 shown in the table in section S.2.4 is used in the bridge superstructure (Strängbetong, n.d.). Cable type 644 means that the tendon consists of 44 Ø6 wires, which implies a cross-sectional area of 1244 mm² per tendon. Furthermore, the pier tendons

consist of 22 $\text{Ø}6$ wires (622 mm^2 per tendon) and are placed 1.8 m apart, centred in the pier walls.

The anchorages in the post-tensioning system are responsible for fastening the ends of the tendons. For this system, they consist of a support plate and a wire anchor, which method allows for individual clenching of each wire, as depicted in Figure 13. By employing this anchorage technique, the occurrence of anchorage losses is prevented.

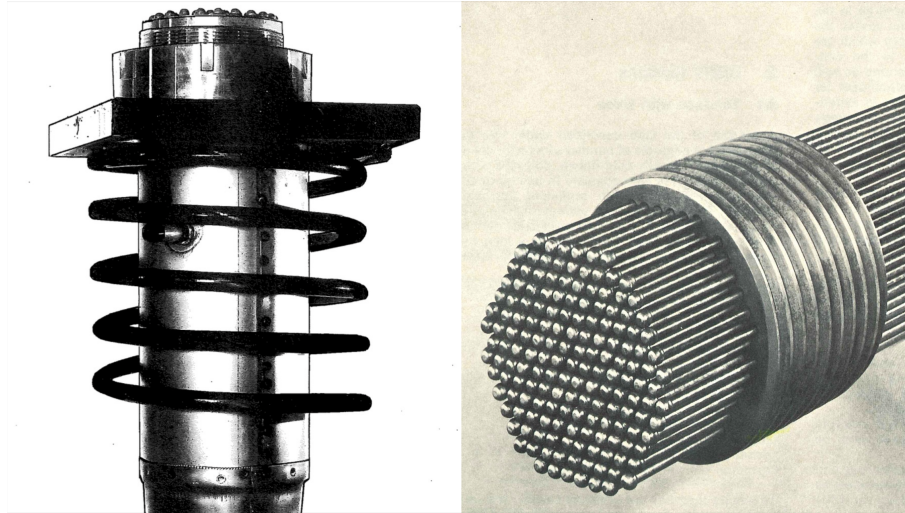


Figure 13: The live-end anchorage to the left (Strängbetong, n.d.), and a closer look of the wires' end to the right. The right figure is courtesy of BBR VT International, extracted from BBRV Report No. 6901 (Bureau BBR, 1969).

The comprehension of the construction process of the post-tensioning system in the beams posed a challenge due to the limited information available. However, through consultation with experts in the field, a hypothesis was formulated and subsequently validated by engineer Asmund Sveen. The hypothesis focused on the sectioning and connections of the tendons, as well as the prestressing sequence, and is illustrated in Figure 14. In one beam, three tendons are divided into segments denoted A, B, and C, while the remaining tendon is connected by movable couplers, indicating that it can be considered a continuous tendon. For further details regarding the post-tension system and anchorages, please refer to Appendix H and Section 3.2.

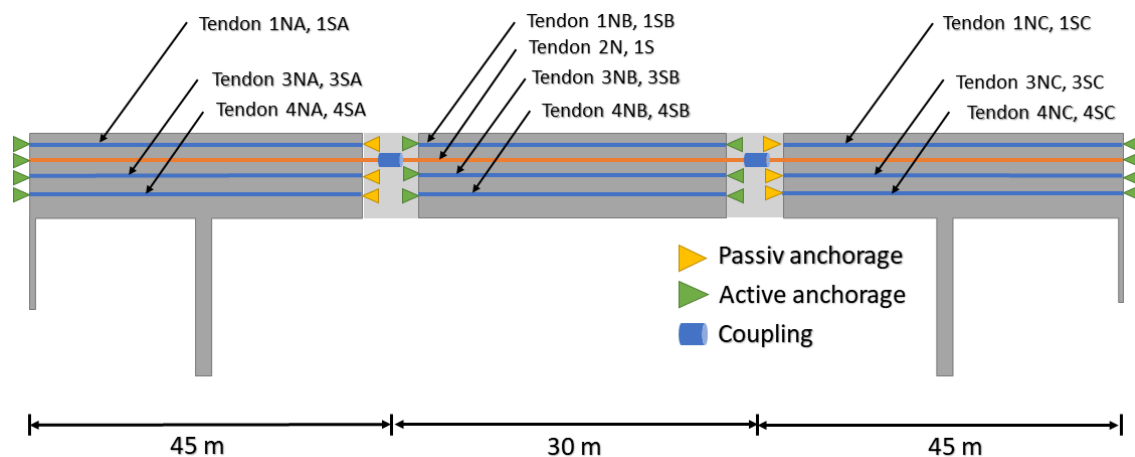


Figure 14: A schematic illustration displaying the names and anchorages of the beam tendons.

3.2 The Construction Process

Being one of the earlier post-tension bridges built in Norway, there is limited information about the way the bridge was built. However, conversations with pertinent experts, extant literature, visual aids, and drawings have provided usable insights into the construction of the bridge.

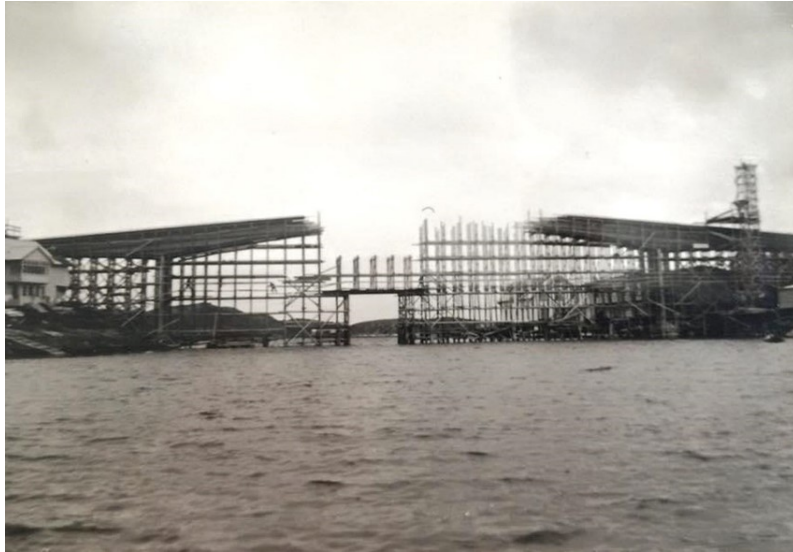


Figure 15: Construction of the bridge framework (Kristian, 2021).

The construction of the bridge involved casting it in place, with all framework built simultaneously. This construction method is supported by photographic evidence of the process, as depicted in Figure 15, and confirmed by engineer Asmund Sveen. Further information provided by Sveen, along with consultations with supervisor Daniel Cantero and professor Terje Kanstad from NTNU, has allowed for a description of the construction phases and the corresponding post-tensioning process as outlined below:

1. The entire framework is constructed.
2. The central 30 m of the midspan, with beam tendons installed, is cast. Subsequently, three out of four tendons in each beam are tensioned and anchored at both ends. In Figure 14, it applies to tendon 1NB, 1SB, 3NB, 3SB, 4NB and 4SB. These active anchorages are designed to facilitate a passive anchorage for the corresponding A and C tendons (e.g., 1NA and 1NC) on the reversed side.
3. The rest of the bridge is cast.
4. The ten tendons located in the bridge deck above both supports are prestressed from a single active end.
5. All remaining tendons are post-tensioned from axis 3 and 6.

3.3 Materials

Material specifications are specified in the original drawings from 1965 provided in Brutus. Consequently, out-of-date terms for concrete, passive reinforcement, and prestressing reinforcement are given. The NPRA manual V413 is used to extract values and understand what the older designations imply.

3.3.1 Concrete

Table 1 provides an overview of the concrete quality in different structural elements comprising Herøysund Bridge. To transform the concrete classes from NS 427A to today's standard, Table 2.1.2 in V413 is used. Furthermore, Eurocode 2 is utilized to calculate the design compressive strength, f_{cd} , and to find the elastic modulus, E_{cm} , which are essential characteristics when assessing capacity. The design compressive strength is

$$f_{cd} = \alpha_{cc} \frac{f_{ck}}{\gamma_c},$$

where f_{ck} is the characteristic cylinder compressive strength after 28 days and γ_c is the partial safety factor for concrete.

Table 1: The concrete class and associated strength for which the various structural parts are designed (Vegdirektoratet, 2021b).

Structural Element	NS 427A (of 1962)	NS-EN 1992-1-1 (NA 3.1.2)			
	Concrete Quality	Concrete Class	f_{ck} [MPa]	f_{cd} [MPa]	E_{cm} [GPa]
Main span, side spans, and piers at axis 3, 4, 5, and 6.	B400	B28	28	16	32.3
Approach spans, piers at axis 1, 2 and 7, and foundations.	B300	B20	20	11	30

As can be seen in the report elaborated by Saksberg (1998), Aas-Jakobsen is using the material specifications from the original drawings in the static analysis and capacity control of Herøysund Bridge. The same is done for their work in 2019 where it is assessed whether or not to pour concrete for cathodic protection (HOS, 2019). But in 2020, drilling into and pressure testing of the superstructure in the main part was carried out and a higher concrete strength than in the original design was revealed (Sveen, 2020). Aas-Jakobsen, therefore, uses concrete class B35 where the original design indicates B28 (see Table 1) in the bearing capacity calculations in Report A.J. 2020.

When it comes to the concrete ingredient cement, there is no specification about the type utilized. After consulting with Håvard Johansen from NPRÅ, it was determined that assuming cement strength class N, defined in Eurocode 2, is reasonable. This choice was made having in mind that older concrete recipes often used pure cement with fewer additives such as fly ash or silica, making them relatively fast.

3.3.2 Passive Reinforcement

The original drawings indicate longitudinal reinforcement of type Ks 40 and shear reinforcement of type St. 00. "Ks" is the antiquated designation of a ribbed bar, while "St" indicates a plain steel bar. The characteristic yield strengths of the passive reinforcement are provided in Table 2, and as it can be seen, St. 00 has a yield stress of 230 MPa. It should be noted that V413 only provides the yield strength of St. 37, which is 230 MPa, but since previous capacity assessments prepared by Aas-Jakobsen use stirrups of characteristic yield strength, 230 MPa, St. 00 and St. 37 are assumed to have the same strength. Moreover, the modulus of elasticity, E_s , is assumed to be 200 000 MPa.

Table 2: Characteristic yield strength of the passive reinforcement (Vegdirektoratet, 2021b).

Rebar	Reinforcement Quality	f_{yk} [MPa]
Plain	St. 00	230, for Ø8 - Ø32
Ribbed	Ks. 40	400, for Ø8 - Ø20 380, for Ø25 - Ø32

3.3.3 Active Reinforcement

All the wires constituting a tendon have a plain steel surface and are cold-drawn. Other material data are provided in the following table:

Table 3: Material characteristics for the BBRV-system (Strängbetong, n.d.).

Material Data		44Ø6
Young's modulus	E_p	205 000 N/mm ²
Cross-sectional area	A_p	1244 mm ²
Characteristic tensile strength	f_{pk}	1770 N/mm ²
Characteristic 0.2 % proof-stress	$f_{p0.2k}$	1570 N/mm ²
Characteristic 0.1 % proof-stress	$f_{p0.1k}$	1520 N/mm ²

The value of the prestressing steel strength utilized in the design, denoted as f_{pd} , can be determined as follows:

$$f_{pd} = \frac{f_{p0.1k}}{\gamma_s},$$

where γ_s is the partial safety factor for steel reinforcement, being 1.15 for persistent and transient design situations.

3.4 Damages

In a series of inspections, significant corrosion damage is discovered on the post-tensioning system. By examining pictures of the surface, exemplified by Figure 16, it is evident that parts of the bridge have corrosion issues. The origin of the damages is investigated and presented by Roy Johnsen (2022), professor at the Department of Mechanical and Industrial Engineering at NTNU, using findings from different inspections.



Figure 16: Pictures of peeling and rust colouring on Herøysund Bridge from Brutus.

During an inspection in January 2020 conducted by Dekra, it was discovered substantially large areas with deficient grouting in critical sections of Herøysund Bridge. In some areas the grouting was insufficient for lengths of up to 6 m, leaving large void spaces. Visual inspections revealed corrosion on the post-tensioning wires at these locations. However, when the grouting was adequate, there was no apparent corrosion inside the ducts. According to the report, there is a direct correlation between poor grouting and corrosion of the prestressing steel.

Another inspection was carried out in August of the same year, but this one was more comprehensive and performed by NPRA. Material samples were extruded and showed both general corrosion and pitting corrosion with greater corrosion damage near the bottom of the tendon than at the top. Pitting corrosion is a dangerous corrosion type due to the uncertainty surrounding the extent. In some ways it can be described as an iceberg floating in water; it can be difficult to know how big it is just by looking at the surface. Pitting corrosion is further explained in Section 2.3.3.

In addition to severe corrosion damage, a broken wire was found during the extensive inspection. The wire was heavily corroded, as shown in Figure 17. Examinations of the broken wire showed that the cross-section at the point of failure was significantly reduced due to pitting corrosion. The remaining cross-sectional area was estimated to be 30-35 % of the initial area. According to Johnsen (2022), the failure of the steel bar is not necessarily only caused by corrosion, but can also be due to stress corrosion cracking.



(a) Broken wire



(b) Wires with no bond to the concrete on the bottom side

Figure 17: Severe corrosion damages (Johnsen, 2022).

Significantly, the majority of corrosion is confined to the interior of the ducts. The tendency is that the exterior of the ducts exhibits favourable conditions, with corrosion observed only in certain locations. This suggests that the corrosive environment exists within the ducts and not in the concrete structure itself. SINTEF also concludes that it is not likely that the grouting has been affected by the external environment outside the ducts. This is due to the low concentration of chlorides in the grout, among other things. The grouting was also examined and found to vary in consistency and humidity. Regions that were the most corroded appeared to be more humid and had a different consistency than the non-corroded areas.

3.5 Measures

The extent of cement grout lack in the post-tensioning cables, as well as the quality of it, is uncertain. The following measures are implemented to monitor the load-bearing capacity until the new bridge is built:

- Carbon fibre straps are installed at the bottom and on the sides of the beams to ensure sufficient load-bearing capacity.
- At the bottom of the beams, it is installed strain gauges to measure the strain in the carbon fibres, while sensors are mounted on the beams' sides to measure crack widths.
- Heavy transport is regulated with road signs that inform about a minimum distance of 100 m.
- The bridge is levelled regularly on levelling bolts mounted along the entire bridge length.

(Sveen, 2021)

4 Loads

Loads that are to be used as calculation basis for design load effects are termed characteristic loads. When calculating existing structures, characteristic loads defined according to V412 must be used. In addition, the load definitions in previous bearing capacity calculation reports prepared by Aas-Jakobsen have been considered.

V412 classifies the characteristic loads into the following main groups:

- Permanent loads
- Variable loads
- Deformation loads
- Accidental loads

All these load groups are considered except for accidental loads, which are not necessary for the capacity assessment that this master's thesis deals with.

4.1 Permanent Loads

Permanent loads, also known as dead loads, are those that remain relatively constant over time and comprise, for example, the weight of the bridge's structural elements. In this work, the following characteristic self-weights are considered:

Reinforced concrete:	25 kN/m ³
Asphalt:	25 kN/m ³
Railing of steel:	0.5 kN/m

A 60 mm thick asphalt layer (1.5 kN/m²) is assumed based on measurements (Sveen, 2020).

4.2 Variable Loads

The variable loads comprise traffic loads and environmental impact due to variations in ambient temperature and wind loads. Nevertheless, only traffic load is included in the linear analysis in DIANA, since the other variable loads are not a part of the presumed design load combination, which is further explained in Section 4.4. Even so, the effect of thermal actions and wind load is briefly discussed in this section on variable loads.

Snow load is another important variable load, especially in Norway. On road bridges, snow load is not considered to co-occur with traffic load, according to paragraph 5.1 in V412, and is therefore neglected.

4.2.1 Traffic Load

According to V412, traffic load is defined as the vertical and horizontal forces arising due to pedestrians and vehicles on the carriageway, hard shoulder, bicycle path, and central reservation. This means that the traffic load on existing bridges includes all road traffic permitted on the public

road network, such as cars, lorries, motorized equipment, and special vehicles. Figure 18 provides an overview.

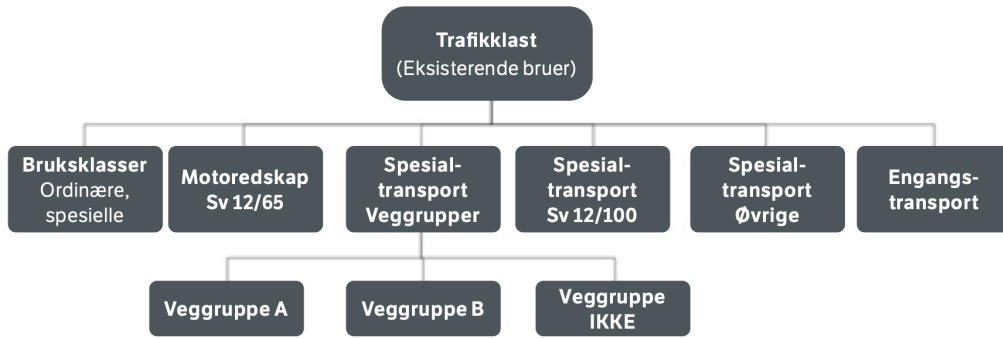


Figure 18: Overview of traffic loads when performing load bearing capacity classification of existing bridges (Vegdirektoratet, 2021a).

Every bridge in Norway is assigned a service class, which represents the traffic load allowed to be driven freely without exemption. The service class is denoted by the abbreviation Bk (short for “Bruksklasse”), followed by the maximum permissible axle load and total weight. For example, Bk 10/50 indicates a service class with an axle load of 10 tonnes (100 kN) and a maximum permissible total weight of 50 tonnes (500 kN).

Herøysund Bridge was originally designed according to load regulation 2/1958, which follows the stress control method rather than the current partial factor method that incorporates load and material factors. The stress control method involves checking occurring stresses against admissible stresses. For specific traffic load descriptions associated with load class 2/1958, reference is made to the outdated Håndbok 239. It is noted in this reference that load class 2/1958 imposes a lower design load than service class Bk 10 for bridges with a span length of approximately 4 m, which aligns with the findings of a handwritten calculation report from 1987. This report also concludes that the reduced requirements for snow and traffic loads allow the bridge to be considered under load class Bk 10. Although the available documentation does not provide information about the utilization rate during the design phase, there is no reason to believe that the safety margin was significantly greater than the regulatory requirements at that time (HOS, 2019).

In more recent load-bearing capacity assessments, such as the one conducted in Report A.J. 2020, Herøysund Bridge is evaluated for service class Bk 10/50. A note from 2021, addressing the instrumentation and load-bearing capacity follow-up, also prepared by Aas-Jakobsen, states that the bridge can maintain the Bk 10/50 classification as long as the measures mentioned in Section 3.5 are implemented and the measurement program is upheld (Sveen, 2021). According to Brutus, this classification remains valid and is set to expire on 31/10/2024. Furthermore, the bridge is not approved for any other traffic load types mentioned in Figure 18. Consequently, in this master’s thesis, Herøysund Bridge is only assessed for service class Bk 10/50.

4.2.1.1 Vertical Forces

The load models, also known as equivalent loads, for each service class include a bogie load, vehicle load, and lorry load, as can be seen in Figure 19. Considering the considerable main span of Herøysund Bridge, which spans 60 m, it can be assumed that the lorry load serves as the critical load model (LM). This is because the lorry load accommodates eight axle loads, resulting in the largest total load among the load models. Apart from the eight axle loads, referred to as $8xA$, the lorry load also includes a uniformly distributed load denoted as p .

The traffic load needs to be positioned in the most unfavourable location along the bridge in the longitudinal direction. Specifically, the axle loads of the lorry LM are applied only at a single location on the bridge, while the uniformly distributed load is distributed across all sections in the longitudinal direction where it contributes adversely. The objective of this thesis is to determine the maximum field stresses in the main span. To achieve this, the 8xA loads are placed in the middle of the main span, while the uniformly distributed load ($p = 6 \text{ kN/m}$) is applied across the entire span, excluding the side spans.

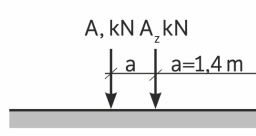
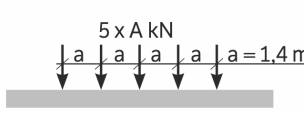
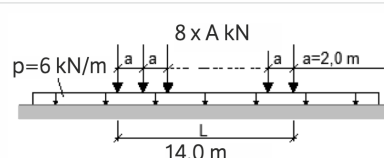
Lasttype	Lastfordeling	Ordinære bruksklasser					
		Bk 10/50	Bk T8/50	Bk T8/40	Bk 8/32	Bk 6/28	
Boggilast		A1	165	125	125	125	100
		A2	120	90	90	55	35
Kjøretøy- last		A	80	68	68	58	45
Vogntog- last		A	60	55	47	38	30

Figure 19: Equivalent loads for the ordinary service classes (Vegdirektoratet, 2021a).

The traffic load also needs to be positioned in the most unfavourable location in the transverse direction within the available carriageway width. The carriageway width, which is defined as the distance between the kerbs, is 4 m. According to Table 4.1 in Eurocode 1-2 (Standard Norge, 2003), this allows for one notional lane of 3 m, leaving a remaining width of 1 m. The area outside the loading lanes does not experience any traffic load. Therefore, in accordance with V412, the critical placement of the lorry load model in the transverse direction can be seen in Figure 20.

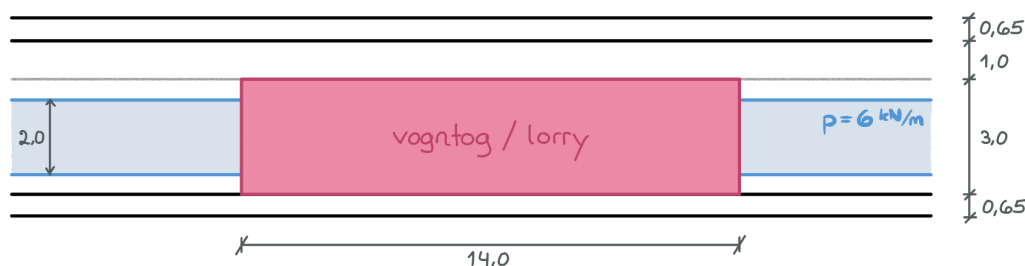


Figure 20: Plan view of the placement of the lorry load in the middle of the main span. The distances are given in meters.

Not only the carriageway but also the footpaths are subjected to vertical traffic load. The amount of traffic load from pedestrians on the footpaths depends on their separation from the carriageway and their width. In the case of Herøysund Bridge, the traffic load on the two footpaths is considered

negligible due to their narrow widths, as specified in V412. Therefore, the focus of the analysis regarding vertical traffic load will primarily be on the carriageway.

4.2.1.2 Horizontal Forces

The horizontal load includes braking loads, transverse forces, and centrifugal loads. They are only acting at the same time as the associated vertical loads in Figure 19. The braking and transverse load associated with lorry LM is placed where the lorry is standing. However, the centrifugal load is not considered pertinent for Herøysund Bridge since the structure only has notable horizontal curvature in the approach spans in the east.

Braking Load

Braking force shall be taken as a longitudinal force acting at the surfacing level of the carriageway. Figure 21 is showing the braking load for the different service classes, which can be assumed to be uniformly distributed over the entire carriageway width. As the figure is showing, Herøysund Bridge is going to be applied a braking load of 300 kN in the capacity analysis.

Brulengde	Bremselast (kN)			
	Bk 10/50 Bk T8/50	Bk T8/40	Bk 8/32	Bk 6/28
≤ 10 m (B1)	150	120	100	90
≥ 40 m (B2)	300	240	190	170

Figure 21: Braking loads for the ordinary service classes and different bridge lengths (Vegdirektoratet, 2021a).

Transverse Force

Lateral forces arise due to skew braking or skidding. A transverse braking force, equal to 25 % of the longitudinal braking or acceleration force, should be considered to act simultaneously with the braking force at the finished carriageway level.

4.2.2 Thermal Actions

Bridges can experience temperature effects that can be classified as either resulting from the seasonal and/or diurnal variation in the mean bridge temperatures or resulting from temperature differences between various bridge elements at any point in time. Variations in the mean bridge temperature will cause expansion or contraction of an unrestrained bridge superstructure. However, Herøysund Bridge is a hyperstatic structure restrained by its supporting piers, meaning that thermally induced stresses will result. Temperature variations between different parts of the bridge can cause both rotational and translational deformations of the superstructure (Imbsen et al., 1985).

In spite of the fact that temperature gradients induce static responses such as displacement and strain, it is considered reasonable to neglect the thermal actions. The intended focus of the study is to evaluate the capacity of the main span, which is less impacted by mean bridge temperature variations compared to the columns. The reason for this is that the superstructure is not fully restrained in the bridge's longitudinal direction, which is potentially introducing substantial moments on the columns. Furthermore, the bridge deck and beams are not of large dimensions, making Herøysund Bridge less prone to great local temperature differences.

Another key aspect is that bridges are more sensitive to temperature variations when considering the serviceability limit state. Temperature variations are constraints in an indeterminate structure.

When concrete cracks, the constraints may be released. Finally, it is worth noting that the load-bearing capacity assessment conducted in Report A.J. 2020 also did not include an evaluation of thermal actions.

4.2.3 Wind Load

Wind load can have a significant impact on the structural integrity and stability of a bridge. Herøysund Bridge exhibits greater sensitivity to wind load on its columns than on its superstructure, given the latter's small dimensions. The horizontal wind load applied to the bridge deck is transferred to the piers and is assumed to have minimal impact on the prestressed beams. Therefore, this study does not consider wind load as critical, as the focus is not on the pier capacity. However, if analyzing the capacity of the columns, a closer examination of wind load would be necessary, as bridge substructures are inherently less redundant when compared to buildings (Magar, 2021). It should be noted that the vertical component of wind load acting on the superstructure can have a significant impact, particularly as it adds to the permanent, traffic, and deformation loads.

4.3 Deformation Loads

Deformation loads are actions that are associated with either applied deformations or the properties of the construction material. Among these are the prestressing force, creep, shrinkage, and relaxation of steel. When it comes to the time-varying deformation of concrete due to creep and shrinkage, it is acceptable to assume that the phenomena are independent and may be calculated separately according to Eurocode 2.

4.3.1 Creep

As concrete ages, its Young's modulus can be reduced to account for the phenomenon of creep. Creep occurs in hardened concrete over time, where for constant load or stress, the deformations increase. In a concrete specimen subjected to a constant sustained compressive load applied at age t_0 , the capacity to creep at time t is usually measured in terms of the creep coefficient. The creep coefficient, $\varphi(t, t_0)$, for a constant sustained load first applied at age t_0 is determined according to the formulas in Annex B of Eurocode 2 and used to calculate the effective modulus of concrete, which is given by:

$$E_{c,eff}(t, t_0) = \frac{E_{cm}}{1 + \varphi(t, t_0)} \quad (3)$$

(Sørensen, 2013). The calculation of $\varphi(t, t_0)$ and subsequently $E_{c,eff}(t, t_0)$ for the self-weight (including the reinforced concrete, asphalt, and railing) and post-tensioning load, for the cross-section in the middle of the main span, is presented in Appendix C.2. The entire bridge was built on formwork, and it is assumed that it was removed 14 days after casting. Therefore, the start time for creep is set to 14 days, and the creep effect has been calculated for approximately 57 years (until 2023).

Calculating an average modulus of elasticity, E_{middel} , is the most practical approach for determining the response of concrete to loads applied at different times, whether they are short-term or long-term. The module is derived by taking into account the curvature contribution and accumulated curvature for the different loads, and is expressed as follows:

$$E_{middel} = \frac{\Sigma|M|}{\frac{|M_{L1}|}{E_{c,eff,1}} + \frac{|M_{L1}|}{E_{c,eff,2}} + \dots + \frac{|M_k|}{E_{cm}}}, \quad (4)$$

where M_{L_i} are the bending moments due to long-time actions (i.e., prestressing, self-weight, and other permanent loads), each applied at a certain time which defines the corresponding effective elastic modulus $E_{c,eff,i}$, and M_k is the moment due to the short-time load. $\Sigma|M|$ is the sum of all those moments in absolute value (Sørensen, 2013). A concise visualization of E_{middel} is provided in the figure below.

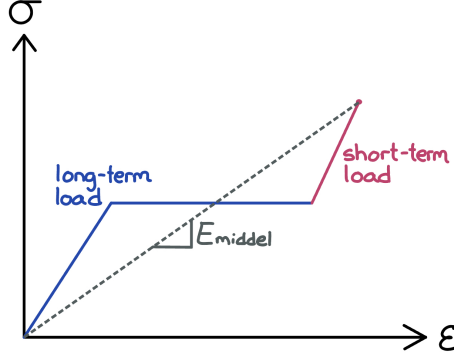


Figure 22: Average modulus of elasticity, E_{middel} .

This thesis work considers the phenomenon of creep by reducing the Young's modulus of concrete to E_{middel} . However, it should be noted that there are other ways to account for the time-dependent material property. Eurocode 2, for example, provides formulas to calculate creep deformation.

4.3.2 Shrinkage

The model for calculating the magnitude of shrinkage strain, as outlined in Eurocode 2, divides the total shrinkage strain ε_{cs} into two distinct components: autogenous shrinkage and drying shrinkage, as given by:

$$\varepsilon_{cs} = \varepsilon_{ca} + \varepsilon_{cd} \quad (5)$$

Autogenous shrinkage occurs in young concrete due to self-desiccation as water is consumed during the hydration reaction. It develops rapidly, with the final value $\varepsilon_{ca}(\infty)$ assumed to be a linear function of concrete strength. The autogenous shrinkage at time t (in days) after casting is given by:

$$\varepsilon_{ca}(t) = \varepsilon_{ca}(\infty) \cdot (1 - e^{-0.2t^{0.5}}) \quad (6)$$

where:

$$\varepsilon_{ca}(\infty) = 2.5 \cdot (f_{ck} - 10) \cdot 10^{-6} \quad (7)$$

As distinct from autogenous shrinkage, drying shrinkage develops more slowly and takes place months and years after setting of the concrete. It increases with time at a gradually decreasing rate. Drying shrinkage is primarily caused by the loss of water during the drying process, which

results in a reduction in volume. The mean value of the nominal unrestrained drying shrinkage strain $\epsilon_{cd,0}$ is given in Annex B in Eurocode 2. If drying commences at age t_s , the drying shrinkage strain at age t is given by:

$$\epsilon_{cd}(t) = \beta_{ds}(t, t_s) \cdot k_h \cdot \epsilon_{cd,0} \quad (8)$$

where k_h is a coefficient that depends on the notional size h_0 and is given in Table 3.3 of Eurocode 2 and $\beta_{ds}(t, t_s)$ is a function describing the drying shrinkage development with time and is given by Equation 9 (Gilbert, Mickleborough, and Ranzi, 2017).

$$\beta_{ds}(t, t_s) = \frac{(t - t_s)}{(t - t_s) + 0.04\sqrt{h_0^3}} \quad (9)$$

The calculations presented in Appendix C.1, using the formulas mentioned above, indicate a total shrinkage strain of 0.233 ‰ for Herøysund Bridge. It should be noted that this shrinkage strain specifically applies to the cross-section in the middle of the main span. Additionally, assuming normal environmental conditions outside, an ambient relative humidity of 80 % is considered in accordance with Eurocode 2.

4.3.3 Steel Relaxation

Eurocode 2 defines three classes of relaxation, namely:

- Class 1: wire or strand - ordinary relaxation
- Class 2: wire or strand - low relaxation
- Class 3: hot rolled and processed bars

The wires in Herøysund Bridge belong to Class 1. To perform design calculations related to steel relaxation, engineers rely on the value of ρ_{1000} , which is the relaxation loss in percentage at 1000 hours after tensioning with initial stress of $0.7f_p$ at a mean temperature of 20 °C. Here, $0.7f_p$ denotes the actual tensile strength of steel samples. ρ_{1000} is expressed as a percentage ratio of the initial stress and may be assumed to equal 8% for Class 1 if not specified in the manufacturer's certificate. Also applicable to Class 1, the loss of stress in the tendon due to relaxation for use in design, $\Delta\sigma_{pr}$, may be obtained from the following expression:

$$\frac{\Delta\sigma_{pr}}{\sigma_{pi}} = 5.39 \cdot \rho_{1000} \cdot e^{6.7\mu} \cdot \left(\frac{t}{1000}\right)^{0.75(1-\mu)} \cdot 10^{-5} \quad (10)$$

where σ_{pi} is the stress in a post-tensioned tendon immediately after anchoring it (i.e. after transfer); t is the time after tensioning (in hours) and $\mu = \sigma_{pi}/f_{pk}$.

The calculation of the stress loss in the tendons of Herøysund Bridge due to relaxation is shown in Appendix D.1, yielding a loss of 178 MPa. It is worth noting that the calculations employ a conservative assumption by setting σ_{pi} equal to the jacking stress. The simplification is carried out since the wedge draw-in is zero and the immediate losses are different in all sections along the length of the cables.

4.3.4 Prestressing Force

The original prestress cable drawings from the bridge superstructure indicate that the tendons are prestressed with an initial force of 1370 kN. However, it is crucial to consider the prestress losses, as elaborated in Section 2.2. To account for the immediate losses, it is necessary to define the coefficient of friction μ and the k factor that represents the unintentional angular deviation. Generally, the wedge draw-in also needs to be specified, but as previously mentioned, the stressing anchorage is designed to prevent anchorage losses. Besides, the anchorage slip would not have affected the critical cross-section in Herøysund Bridge, considering the long span lengths.

As mentioned in Section 2.2.2, μ and k shall be given in an ETA of the BBRV post-tensioning cables. However, as the ETA was launched in the early 2000s and Herøysund Bridge dates back to 1966, an ETA is not available for the post-tension cables in this bridge. To obtain the loss coefficients, the material and cross-sectional data from Osstrupen Bridge, which also utilizes the BBRV post-tensioning system, were used. The value of μ is set to 0.2, which is in reasonable agreement with Eurocode’s recommendation. For internal tendons consisting of cold-drawn wires, Table 5.1 of Eurocode 2 suggests a coefficient of friction of 0.17. Moreover, k is set to 0.002, which falls within the range recommended by Eurocode 2 (Hangaard and Aasheim, 2018). In addition, the unintentional angular deviation of 0.002 falls within the range that the Australian concrete standard, AS 3600-2009, suggests for sheathing containing wires $\phi \leq 50$ mm, being $k = 0.024 - 0.016$ rad/m. Even though it is an Australian standard, the ranges are considered relevant as they are stated and adapted in the book “Design of Prestressed Concrete to Eurocode 2” (Gilbert, Mickleborough, and Ranzi, 2017).

Having defined the wedge draw-in, friction coefficient, and unintentional angular deviation, the only immediate loss that remains to be considered is that caused by elastic shortening. To calculate the elastic deformation losses, the average stress loss is determined, as explained in Section 2.2.1 and demonstrated in Appendix D.2. The calculation yields an average prestress loss of 15.2 MPa for the central tendons post-tensioned in Phase 2 of the construction process described in Section 3.2, which is equivalent to a loss of 1.4 %. For the remaining tendons, a conservative approach is taken by assuming the number of tendons in a section, n , to be 18, which represents the maximum number of tendons in a section. This assumption results in an average prestress loss of 36.8 MPa.

When it comes to the time-dependent losses of the prestressing force, creep, shrinkage, and relaxation exhibit interdependence and influence each other. In Section 2.2.4, reference is made to methods accounting for the dependencies of the phenomena. However, considering the long-term effects separately is a valid approach, and is what is done in this master’s thesis. Creep, shrinkage, and steel relaxation are taken care of as elaborated in Section 4.3.1, Section 4.3.2, and Section 4.3.3 respectively. Even though the three phenomena are computed separately, the prestress loss due to relaxation is reduced by a factor of 0.8, in accordance with clause 5.10.6 (1) of Eurocode 2, to account for the relaxation of steel being dependent on the concrete deformation due to creep and shrinkage. As a consequence, $\Delta\sigma_{pr}$ decreases from 178 MPa to 142 MPa.

Moving on to the tendons situated in pier 3 and 6, the available information for these four BBRV cables is unfortunately limited. Without any specified post-tension load, an estimation had to be made based on the stated cross-sectional area. It is assumed that these tendons are stressed with the maximum allowed force, similar to the approach taken for the tendons in the superstructure. By referring to Report A.J. 2020, the allowed prestress force was determined using Equation 11. As a result, the 22 ϕ 6 tendons in the piers were found to have a post-tension force of 680 kN. It is worth noting that the same prestress losses, as mentioned earlier, apply to the tendons in the piers as well.

$$P_{max} = 0.7 \cdot f_{p0,2k} \cdot A_p \quad (11)$$

Significantly, the factor of 0.7 employed in these calculations is notably lower than the standards in practice today. This use of the lower factor can be attributed to the uncertainties and limited practical experience associated with post-tensioned structures during that time. It is important to note that Herøysund Bridge, designed in 1965, represents an early version of a post-tensioned bridge, which further justifies the adoption of the lower factor.

4.4 Design Load Combinations in ULS

In accordance with V412, two sets of load combinations must be checked, with partial factors as shown in Figure 23. The load-bearing capacity assessment is based on the most unfavourable combination of a and b . However, it is reasonable to assume that the design load combination is a , given that the symbols in Figure 23 represent and have the following values:

- γ_D is the partial factor for the deformation load, or rather the prestressing force, which is equal to 0.9.
- γ_1 is the partial factor for the service class, being 1.4 in the case of Herøysund Bridge having one notional lane.
- γ_2 is also a partial factor for the service class, equal to 1.2.
- Q_1 represents the characteristic value of the variable load that produces the most critical load effect.
- Q_n represents the characteristic value for any other variable load that may cause an unfavourable load effect.

In the case of Herøysund Bridge, the three central actions are the self-weight of the structure, the post-tension load and the traffic load it carries. Traffic load is thus the critical variable load and constitutes Q_1 . Such a significant combination of temperature and wind loads must occur that load combination b surpasses a in magnitude. It is possible that load combination b may be more critical for certain specific conditions, such as when a column moment or displacement of a support is assessed. However, in the context of the thesis, the focus is on determining which load combination results in the most severe vertical response of the superstructure.

Lastgruppe Kombinasjon	Permanente laster, P		Deformasjons- laster, D	Variable laster Q
	Jordtrykk, J	Egenlast/Andre		
a	1,0	1,15 ⁽¹⁾⁽²⁾	γ_D	$\gamma_1 \cdot Q_1$
b	1,0	1,0	1,0	$\gamma_2 \cdot Q_1 + 0,8 \cdot \Sigma Q_n$

Figure 23: Partial factors for the combination of actions in ULS (Vegdirektoratet, 2021a).

5 Exploring Relevant Methods in DIANA Modelling

This chapter addresses and documents the findings when relevant methods and tools in DIANA were explored. Specifically, it focuses on the use of Composed Line Elements and DIANA’s handling of prestress losses due to friction. Additionally, the feasibility and significance of performing Phased Construction Analysis have been investigated. The reason for including this chapter in the master’s thesis is that a significant amount of time has been devoted to exploring DIANA, and the observations can likely benefit others, or rather, next year’s master’s students.

5.1 Composed Line Elements

In DIANA, the direct output of cross-sectional forces from the analysis is not available. However, the software provides a method of reproducing them through the use of *composed line elements*. This method is further explained in one of DIANA’s tutorials, named “Design Analysis of a 3D Box Girder Beam using Composed Line Elements”. DIANA integrates stresses in the surrounding finite elements giving cross-sectional forces. However, as discovered by fellow student, Brage Sikveland, this method needs a configuration for post-tension loads. As stated by DIANA support, the composed line method considers both the stresses in the concrete as well as the reinforcement. When the post-tension load is applied, there are compressive stresses in the concrete and tensile stresses in the reinforcement that by integration cancel each other. The output for a statically determined system will therefore give the impression that there are no cross-sectional forces. A static indeterminate system will only present the secondary moments, also known as restraint forces. To include the forces due to the prestress load and its eccentricity, i.e. the primary moments, one must exclude the reinforcement. This is done by creating a separate output in the analysis and selecting “NONE” reinforcement as shown in Figure 24.

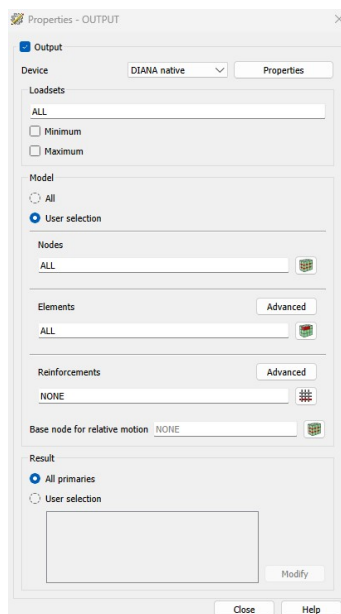


Figure 24: Composed line elements - output properties.

Although the DIANA support team assisted in understanding the composed line method, it is essential to verify whether the method accurately reproduces the desired diagrams. Validation of the method was conducted by modelling a simply supported beam, which allowed for control over the parameters and facilitated result verification. The configuration of the simple beam is

depicted in Figure 25. A structural linear static analysis was performed using a mesh element size of 50 mm, and all prestress losses were neglected. The obtained results were compared with hand calculations, and the comparison is presented in Table 4. For detailed hand-calculated results, refer to Appendix F.

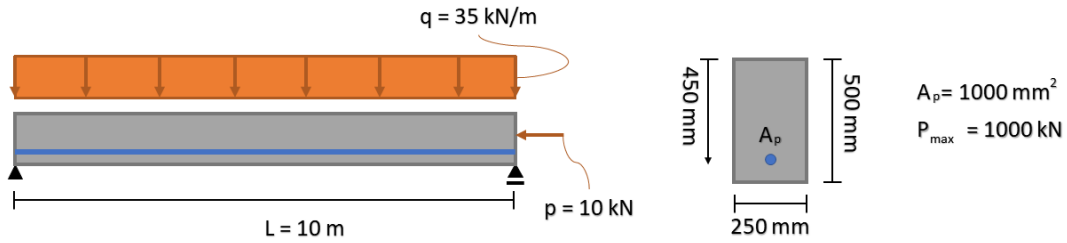


Figure 25: Simple beam subjected to a jacking force P_{max} , an axial force p , and a uniformly distributed load q .

Table 4: Comparison of results obtained from linear analyses in DIANA and hand calculations for the simple beam.

Uniformly Distributed load, 35 kN/m			
	Hand Calculations	DIANA	Deviation
$M_{y,max}$ [kNm]	437.5	437.5	0
$V_{z,max}$ [kN]	175	174.1	0.9
$N_{x,max}$ [kN]	0	≈ 0	0
Axial Force, 10 kN			
	Hand Calculations	DIANA	Deviation
$M_{y,max}$ [kNm]	0	2.5	2.5
$V_{z,max}$ [kN]	0	0.3	0.3
$N_{x,max}$ [kN]	10	10	0
Post-Tensioning Load, 1000 kN			
	Hand Calculations	DIANA	Deviation
$M_{y,max}$ [kNm]	200	200	0
$V_{z,max}$ [kN]	0	≈ 0	0
$N_{x,max}$ [kN]	1000	1000	0

The comparison table above demonstrates a strong agreement between the results obtained from DIANA and the hand calculations. Specifically, in the uniformly distributed load case, the shear force exhibits the maximum deviation, with an approximate difference of 0.5%. Among the various load cases, the largest deviation occurs in the case involving axial loading, resulting in a difference

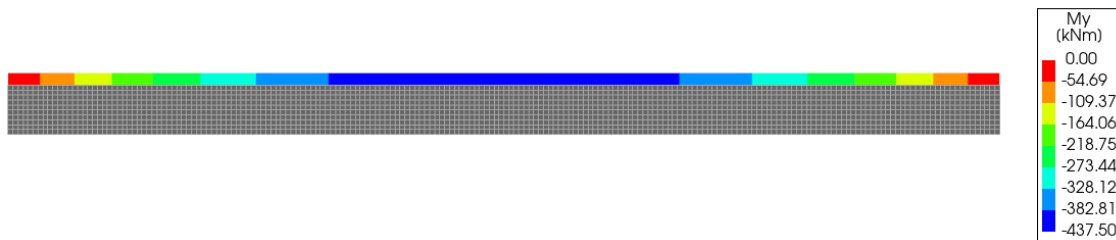


Figure 26: The bending moment distribution, M_y , due to the uniformly distributed load of 35 kN/m acting on the simply supported beam.

of 2.5 kNm in the bending moment. Notably, no deviations are observed for the post-tensioning load case. In summary, the deviations observed are minimal, confirming the validity of using composed line elements for obtaining forces. Furthermore, it is worth highlighting that the distribution along the beam aligns well with beam theory, as illustrated in Figure 26.

5.2 Losses due to Friction

Given the emphasis of this study on creating an accurate model of Herøysund Bridge, where the post-tensioned tendons play a vital role in the load-bearing system, it is imperative to have a comprehensive understanding of how DIANA handles prestress losses. This understanding is crucial for interpreting the output results effectively.

To validate DIANA's treatment of prestress losses resulting from friction and ensure its alignment with theoretical principles, hand calculations were performed specifically for tendon 2N using Python. The prestress force at any given distance along tendon 2N was determined using the following equation, derived from Equation 2:

$$P(x) = P_{max} \cdot e^{-\mu \cdot (\theta + k \cdot x)} \quad (12)$$

These calculated prestress values were then compared to the corresponding output obtained from DIANA. It is important to note that, during this stage of the modelling process, the tendons were represented as piece-wise linear elements, and the meshing order was linear. Through this validation process, a notable issue related to prestress losses was identified: DIANA did not account for the sum of the absolute values of angular deviations over the tendon length, denoted as θ . This finding was unexpected, prompting contact with the DIANA support team. Further confirmation of this issue was obtained from Dr. Denise Ferreira, a product specialist at DIANA.

It is worth noting that this issue is not directly attributed to a software bug but rather an unfortunate constraint. DIANA's support engineer, Hee-Jeong Kang, elaborated on the problem, explaining that it arises when DIANA attempts to capture the tendon's curvature. To accomplish this, the tendon must be defined as a curve, consisting of three or more points. At the time of this thesis work, the program could not capture the curvature of a piece-wise linear representation comprising straight lines. Moreover, for DIANA to accurately reproduce the losses, the mesh order must be set to *quadratic*. For a linear meshing order, improvements in the meshing procedure or the kernel algorithm are necessary to account for the θ parameter. Both possibilities are being considered by the DIANA team as long-term projects.

Armed with this information from the DIANA support team, a decision was made to update the model accordingly. Specifically, the tendon geometry was defined using curves, and a quadratic meshing order was implemented. The results of this update were compared to the hand calculations, and Figure 27 illustrates the resulting prestress development in tendon 2N from axis 6 to the middle of the main span. A noticeable deviation between the losses produced by DIANA and the hand-calculated values, especially in the initial stages, was observed. The underlying reason for this discrepancy remains unclear. However, it is evident that the software accounts for angular deviations, unlike when a linear meshing order was employed in conjunction with tendons represented by straight segments. This can be observed in the figure, where the declining blue graph representing the results obtained in DIANA is uneven, indicating varying angle changes along the tendon length. Disregarding the θ parameter would result in a steadily decreasing blue graph, as the unintentional angular deviation, k , remains constant.

To summarize the findings thus far, the development of prestress force obtained through hand

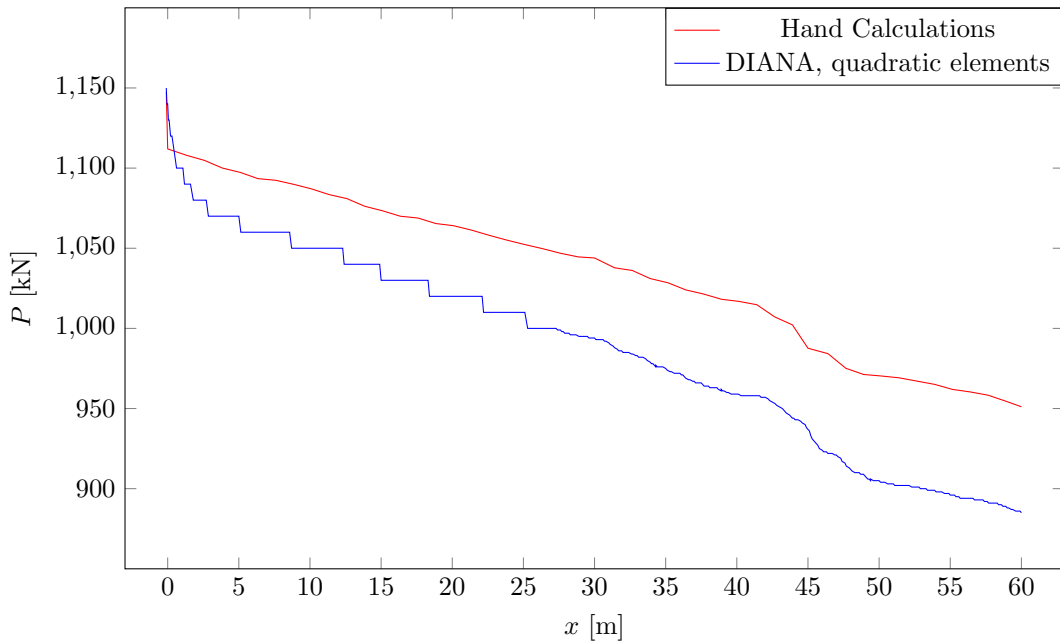


Figure 27: Prestress force, P , along tendon 2N with losses included, extending from one anchorage located at axis 6 ($x = 0$ m) to the midpoint of the main span ($x = 60$ m).

calculations differs from that obtained in DIANA, and the underlying reason for this disparity is not evident. This discrepancy may suggest a potential issue with how DIANA accounts for prestress losses, assuming the hand-calculated prestress losses are accurate. Further details will be provided in the upcoming subsection.

Furthermore, it is crucial to mention that due to limited computational resources in this thesis work, it is appropriate to avoid the use of a quadratic meshing order as it leads to an extensive increase in meshing and analysis time. Having said that, a detailed examination of this topic will be presented in the upcoming chapter on modelling. Consequently, linear meshing order is utilized while representing the tendons with curves. It is worth mentioning that the representation of tendons as curves has little to no effect since quadratic meshing order is not adopted. The angular deviation over the tendon length is then included through the unintentional angular deviation, or wobble factor, set to 0.002.

5.2.1 Including Angular Deviations Through the Wobble Factor

To account for the angular deviations (θ) in DIANA's post-tension load definition, the adjusted wobble factor must be determined. To include θ through the wobble parameter, an averaged curvature of the tendon is incorporated. This averaged curvature and the wobble parameter have the same dimension, namely "1/length". Essentially, an average angle change per unit length is calculated by summing the absolute values of the angular deviations and dividing the sum by the length of the tendon.

The averaged change in angle can be computed from a list of coordinates describing the tendon layout. To do this, vectors are defined between a point and its previous and next point, as shown in Figure 28. The angle between the two vectors can then be calculated using Equation 13. By summing the resulting angles for each point in the coordinate list and dividing the sum by the length of the tendon, the average change in angle along the tendon is obtained.

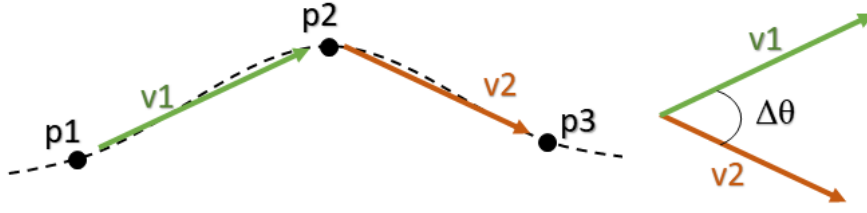


Figure 28: The derivation of vectors and calculation of angles between consecutive points in the tendon layout.

$$\cos(\Delta\theta) = \frac{v1 \cdot v2}{|v1| \cdot |v2|} \quad (13)$$

To validate the approach of including the averaged curvature of the tendon in the wobble factor, tests were conducted on tendon 2N. The results were compared to hand calculations and DIANA's output when a quadratic meshing order was applied. The comparison is illustrated in the plot presented in Figure 29. The plot confirms that the calculated averaged curvature, or the method of calculating θ and incorporating it into the wobble factor of 0.002 (green graph), is accurate, as it exhibits good agreement with the hand-calculated prestress values (red graph). It is important to note that, in proximity to the anchorage located at axis 6 ($x = 0$ m), the results obtained with DIANA using a linear meshing order show similar deviations from the hand calculations as the results obtained with DIANA using a quadratic meshing order. However, the focal point of interest in this thesis work lies at the midpoint of the main span ($x = 60$ m), where the prestress value is the same for both the red and green graphs. This validates the approach of including the angular deviations over the tendon length through the wobble parameter as an accurate method.

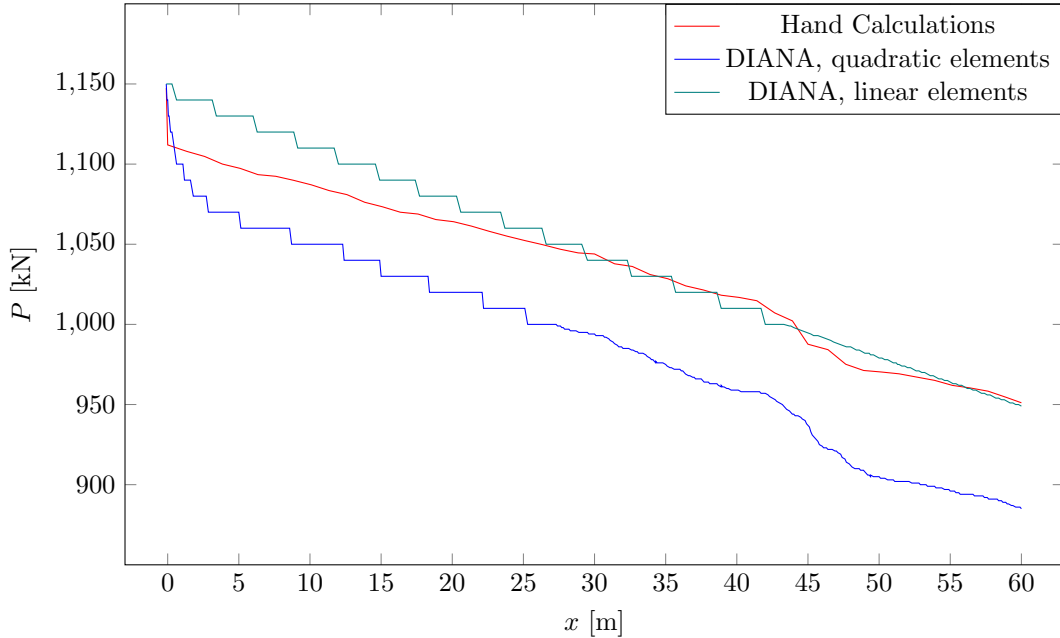


Figure 29: Prestress force, P , along tendon 2N with losses included, extending from one anchorage located at axis 6 ($x = 0$ m) to the midpoint of the main span ($x = 60$ m), highlighting the comparison between hand calculations and the two ways of modelling friction loss in DIANA.

5.3 Phased Construction Analysis

In modelling, it is crucial to include the correct load and deformation history from the start. A completely accurate model and analysis of the bridge is therefore simulating the different construction phases with corresponding prestressing of the reinforcement, as enumerated in Section 3.2. For example, prestressing of the central tendons does not have any loading effect on other parts of the bridge than the central 30 m of the main span, but since the DIANA model of Herøysund Bridge is only a single static model, this is not taken into account in this thesis. Similarly, prestressing of the deck tendons in step 4 does not affect the central 30 m of the midspan as it is not yet connected.

Report A.J. 2020 considers the phased construction in the NovaFrame analysis program by performing prestressing of the reinforcement on different static systems before all the models are assembled into a complete bridge at the connection points. It is also possible to perform phased construction analysis in DIANA, even for linear analysis (DIANA FEA_{BV}, 2022, 10.6, 66.3). Phased analysis determines the effects of construction history and shows the critical construction stages, but, naturally, it comprises several calculation phases, and is considered too time-consuming to undertake in this thesis work. In addition, the phased construction is assumed reasonable to neglect in an analysis of the current capacity, due to the following arguments:

- The entire bridge is built on scaffolding, and in theory, the entire scaffold is removed simultaneously at the end. Thus, the entire bridge is loaded with its self-weight and all other loads, except for prestressing force, at the same time. For instance, the traffic load that occurs later, after the bridge is opened, occurs on the continuous system. Therefore, the continuous system must be considered in the analysis.
- The importance of construction history effects diminishes over time as force redistribution occurs due to creep. This can be further elaborated through the example of prestressing the middle 30 m of Herøysund Bridge. If the bridge had been constructed solely of steel and modelled using separate static systems to simulate the phased construction, the prestress forces would have been permanent and limited to the midspan. However, since the entire bridge is made of concrete and undergoes creep, the effect of prestressing applied to the local system gradually affects the entire bridge. The middle section of the bridge “pulls” at all parts around it, causing the bridge to approach a state as if there was no phased prestressing. While the first system experiences only elastic deformation, creep deformation is two to three times larger and affects the entire system. After 30-40 years, the bridge approaches today’s final system.

Although neglecting phased construction is considered reasonable, the impact of prestressing only the six central beam tendons (i.e. tendon 1NB, 1SB, 3NB, 3SB, 4NB, and 4SB) was examined during the early stages of model development. The validity of this assumption is confirmed in Section 7.1.

6 Modelling Herøysund Bridge in DIANA

This chapter presents the structural three-dimensional modelling process of Herøysund Bridge in DIANA. It is important to provide a detailed description of this process to assist others conducting similar work. The bridge modelling is accomplished through a combination of Python scripting and DIANA's interface. Python scripting proved to be essential during the project work associated with this master's thesis, especially for modelling complex geometry. Notably, some of the complex geometry features can be observed in the meshed bridge shown in Figure 30.

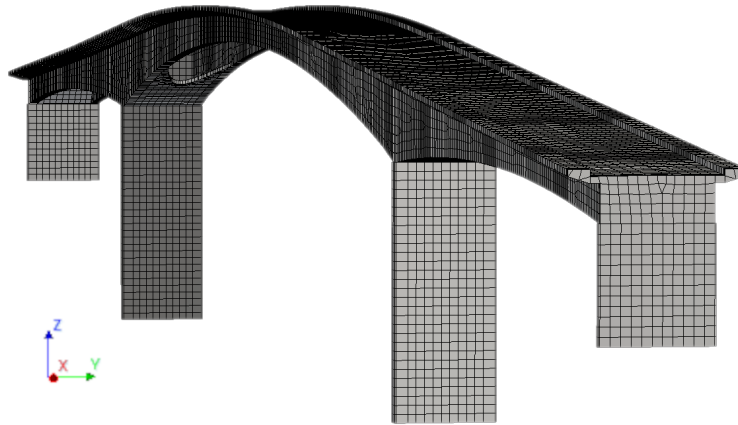


Figure 30: Meshed bridge.

6.1 Reference System and Reference Line

In DIANA, the global reference system is established using x , y , and z coordinates. For this bridge model, the x -axis is defined horizontally along the longitudinal direction of the bridge, following the standard practice in bridge engineering. The z -axis is defined in an upward vertical direction, while the y -axis is defined perpendicular to the longitudinal direction. Refer to Figure 30 and Figure 33 for visual illustrations of the reference system.

The main modelling approach involves using coordinates located in the top-middle of the cross-section that follows the bridge roadway (see Appendix A, Drawing 1 for coordinates). To establish a point of origin at the beginning of the bridge, the coordinates are shifted 60 m forward. This facilitates the intuitive simulation of removing post-tensioned tendon parts when considering corrosion damage. The coordinates are organized in an Excel sheet before being saved as a CSV file and imported into Python. This set of coordinates serves as a reference line for modelling and is referred to as such throughout this section. A similar procedure is followed for obtaining the cross-section heights, which is a separate list of coordinates. Both the reference line and cross-section heights are combined in a CSV file for utilization in Python (see Figure 31).

	A	B	C	D
1	x	y	z	Beam Height
2	-100	0	9902	1392
3	0	0	9910	1400
4	100	0	9918	1408
5	300	0	9934	1390
6	1600	0	10038	1325
7	2000	0	10070	1311

Figure 31: CSV file containing coordinates for the reference line and values of cross-section heights.

6.2 Geometry

The geometry of the bridge is accurately modelled using Python scripting, which is the preferred method due to the bridge's varying curvature and cross-section height. While striving for precision in emulating geometry, certain simplifications have been introduced. The horizontal curvature of the bridge part of interest is negligible and thus not modelled. Moreover, the bridge is modelled with the same transversal slope from the middle and out to the edge beams. Detailed specifications regarding the geometry can be found in Section 3.1, supplemented by drawings in Appendix A.

The approach to modelling the geometry involves a step-by-step process, focusing on one feature at a time. This is accomplished by saving the project after each new feature is added and subsequently reopening it at the start of a new script that models a different feature. This approach offers better control and enables the identification of errors during development. Additionally, this methodology facilitates the modelling of the post-tension system as the final step, providing the flexibility to apply configurations for simulating damage scenarios.

6.2.1 The Concrete Structure

The bridge is modelled by creating multiple cross-sections and lofting between them. This is achieved by generating a series of points using the reference line coordinates and corresponding cross-section heights. These points are then used to create polygon sheets, which accurately represent the cross-sections of the bridge. The creation of these polygon sheets is facilitated through a proprietary function in DIANA. An example of a cross-section with arbitrary height is depicted in Figure 32.

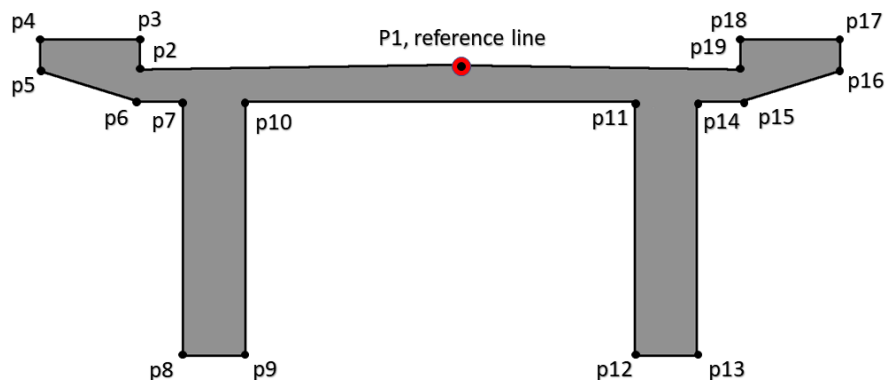


Figure 32: Cross-section with arbitrary height.

To achieve a more accurate representation of the bridge geometry around the piers, additional

points are interpolated along the reference line and corresponding cross-section heights. This interpolation process allows for a finer level of detail in the bridge model. The resulting geometry, including the piers, is illustrated in Figure 33. The piers themselves are created by generating simple cross-sections and extruding them to match the precise height of each pier.

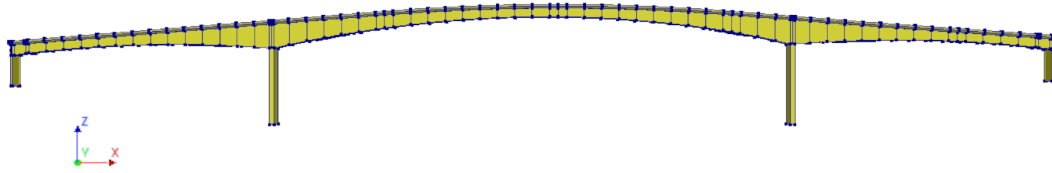
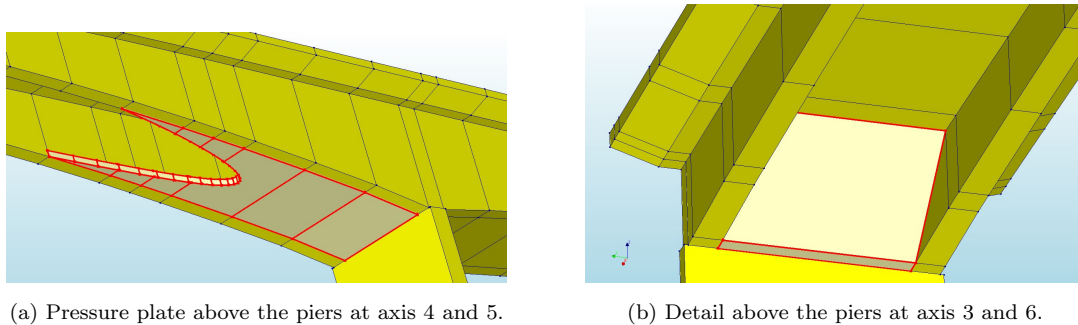


Figure 33: Front view of the bridge geometry.

The final step in modelling the solid concrete geometry involved the incorporation of pressure plates connected to the main span supports, namely the piers at axis 4 and 5, as well as the end sections associated with the side span supports at axis 3 and 6. Initially, the pressure plates were modelled as simple rectangular plates. Subsequently, a void was created by defining a sheet using coordinates generated from a quadratic function. The sheet was then extruded and subtracted from the plate to form the void. The end sections above the columns at axis 3 and 6 are designed based on the provided drawings. The resulting geometry is depicted in Figure 34.



(a) Pressure plate above the piers at axis 4 and 5.

(b) Detail above the piers at axis 3 and 6.

Figure 34: Details above the supports.

6.2.2 Passive Reinforcement

Passive reinforcement is modelled according to drawings. The longitudinal reinforcement is modelled with DIANA's modelling function *Curve*, which is created by coordinates calculated in Python from available data. *Polyline* is used for reinforcement with a more detailed shape, such as shear reinforcement and main reinforcement in the transverse direction. Drawings also suggest a simple rebar in the edge beam for each railing post, this is however disregarded in the model. Only simple longitudinal compression reinforcement, 11 $\phi 10$, is modelled in the pressure plates above the piers.

Passive reinforcement in the piers is also included, with the longitudinal reinforcement modelled as simple lines defined by two points. Shear reinforcement is modelled as simple stirrups encircling the longitudinal bars as a simplification of the drawings. Figure 35 is showing detailed reinforcement in connection to the column at axis 4. With no significant effect on the results, some lengths of the reinforcement bars must be assumed due to a lack of information.

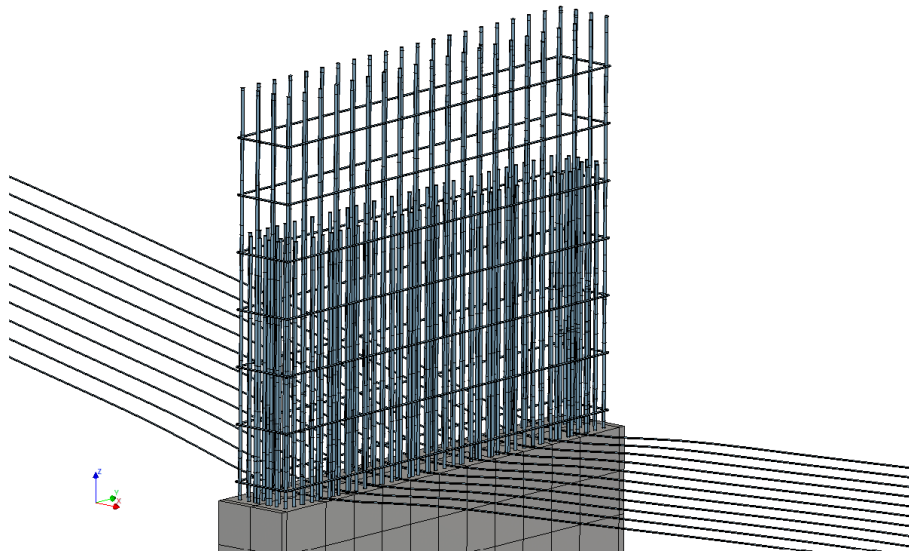


Figure 35: Passive reinforcement in the pressure plate located above the pier at axis 4, along with the reinforcement incorporated within the pier.

6.2.3 Active Reinforcement

The complete post-tension system is simulated in DIANA, incorporating four tendons in each beam, ten tendons in the deck positioned above axis 4 and 5, and two tendons in the piers at axis 3 and 6. Tendon drawings indicate where the tendons should be placed relative to the beam section boundaries, as shown in Figure 36. To model the tendons it is necessary to derive new lists containing points along the reference line and cross-section height values corresponding to the sections defined in the tendon drawing. This involves interpolating between the available points and values in the lists introduced in Section 6.1. Subsequently, by considering the cross-section dimensions, coordinate lists describing each tendon layout can be generated.

To model the tendons, a *Curve* is created using the above-mentioned coordinates. The same procedure is followed for the tendons in the bridge deck. However, for the piers, the tendons are modelled as *Lines* defined by two points.

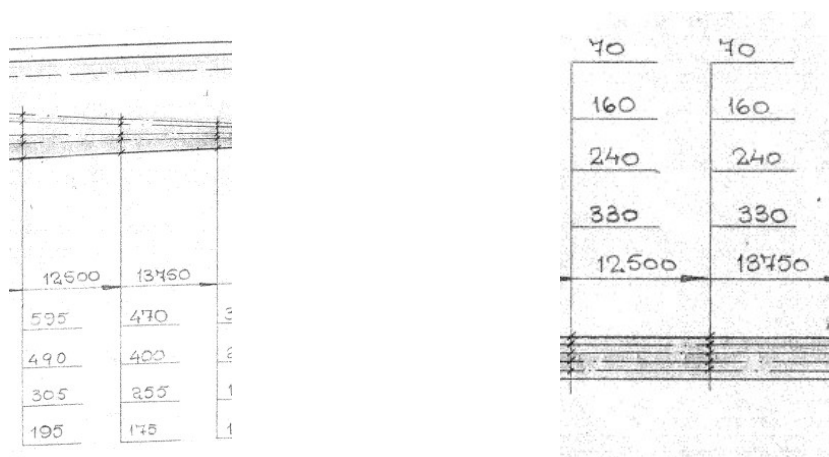


Figure 36: Tendon layout described relative to the cross-section boundaries.

6.3 Properties

After defining the geometry, the next step involves assigning properties to the geometric shapes. The properties of the concrete and reinforcement are established based on the specifications provided in Section 3.3.

6.3.1 The Concrete Structure

The bridge superstructure and piers are assigned with element class *Structural Solids* and a concrete material according to the specifications given in Table 1. The concrete material is assigned the *Concrete and Masonry* material constitutive model with linear elastic isotropic properties. For the linear elastic isotropic model, parameter performance indicators in all directions are the same. Parameters that need to be specified are shown in Figure 37 and include the elastic modulus, Poisson's ratio, and density. Poisson's ratio for uncracked concrete generally lies within the range of 0.15-0.22 and for most practical purposes may be taken as 0.2. In addition to the latter mandatory parameters, thermal effects are included and the reason for that is explained in Section 6.4.2. A coefficient of thermal expansion for concrete of $10 \cdot 10^{-6} / ^\circ\text{C}$ is typically sufficient in design when more detailed information is unavailable, and thus it is assigned to the model (Gilbert, Mickleborough, and Ranzi, 2017).

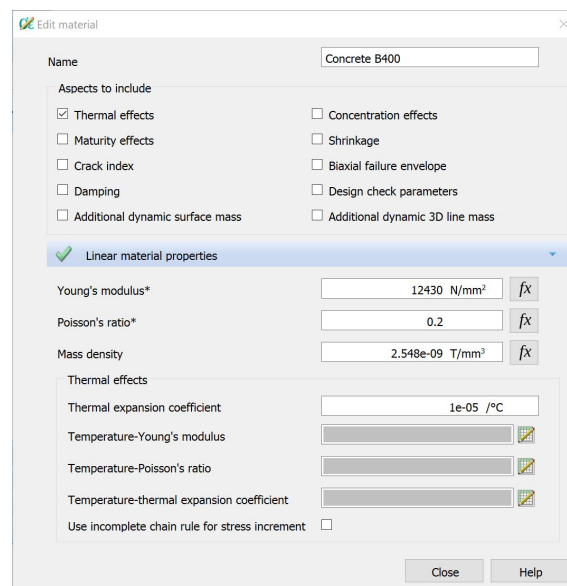


Figure 37: Linear material properties - concrete.

The *Concrete and Masonry* material constitutive model has some suitability for simulating certain aspects of concrete behaviour. However, its limitation lies in the lack of consideration for long-term parameters such as creep and concrete element age. As a result, it is unable to accurately simulate time-dependent issues addressed in international codes. Consequently, other methods have had to be employed to account for the long-term parameters. The material constitutive model in accordance with Eurocode 2, which can simulate all kinds of conditions in concrete, is not chosen because it is preferable to have control over all input parameters, particularly when a nonlinear analysis is not intended.

6.3.2 Reinforcement

A Young's modulus according to specifications given in Section 3.3.2 and Section 3.3.3 is assigned to the passive and active reinforcement, respectively. The materials are assigned the class *Reinforcements* and material model *Linear elasticity*. As for the concrete, thermal effects are included to later simulate shrinkage. The thermal expansion coefficients for both the prestressed and non-prestressed steel reinforcement are set to $10 \cdot 10^{-6} / ^\circ\text{C}$. Both reinforcements are modelled as embedded bars, where the meaning of this was explained in Section 2.4.2. Figure 38 shows how the different specifications are applied in DIANA.

When assigning material properties to the prestressed and non-prestressed steel, the bonding aspect is the crucial differentiator. In the material definition of prestressing steel, the bonding aspect is included, and the option “Reinforcement is not bonded to mother element” is selected, as shown in Figure 39. However, this is not the case with Herøysund Bridge's tendons, which are bonded to the concrete by grouted ducts. Despite this, the tendons are left unbonded in DIANA to simplify the modelling. When the option “Reinforcement is not bonded to mother element” is deselected, the bonding occurs before the prestressing force is applied, resulting in inaccurate results. To apply bonding after tensioning, a phased nonlinear analysis must be conducted. Although the tendons are left unbonded in the model, it will be shown later that this has little to no impact on the results of the linear static analysis of the bridge.

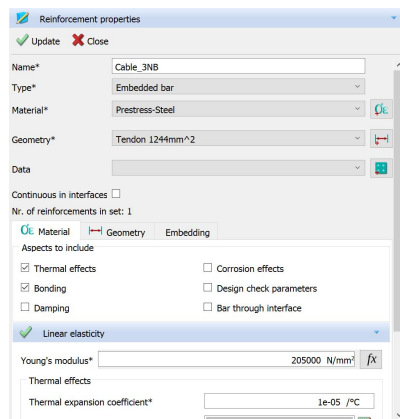


Figure 38: Reinforcement property assignment for prestressing steel.

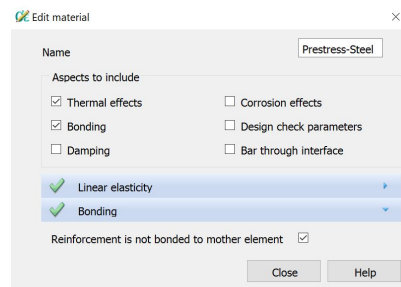


Figure 39: Tendons are not bonded.

6.4 Loads

In DIANA, loads are mainly applied using the software's interface. However, for post-tension loads, a different approach is employed by utilizing Python scripting. This allows for better flexibility when simulating the damaged post-tension system. Additional lines are added to the model to facilitate the placement of loads as required. Detailed load specifications can be found in Section 4.

6.4.1 Self-Weight

To represent the self-weight of the reinforced concrete structure in DIANA, it is modelled as a global load categorized as *Deadweight*. Self-weight of reinforced concrete is given as $2.548 \cdot 10^{-9}$ Tons/mm³, derived from its characteristic self-weight. The self-weight of the railing is represented as line loads applied on the edge beams, positioned 2.5 m away from the centre line of the bridge. Furthermore, the self-weight of the asphalt is simulated as a uniformly distributed load that is

applied across the carriageway. This load is distributed over the entire top surface, except for the edge beam, ensuring an accurate representation of the asphalt's weight distribution.

6.4.2 Creep and Shrinkage

Both creep and shrinkage are nonlinear material behaviours that can be simulated in DIANA through time steps in a nonlinear analysis. However, while shrinkage can be viewed as a linear behaviour from a material perspective, it is still a nonlinear aspect that requires careful consideration. It is important to note that creep and shrinkage are not inherent attributes of the *Concrete and Masonry* material defined by linear elastic isotropic properties, and as such, they are simulated using different methods.

Creep

In DIANA, creep is modelled as a reduction of the Young's modulus, where the concrete material is assigned E_{middel} , instead of E_{cm} , as calculated by Equation 4. The calculation using this formula is as follows:

$$\begin{aligned}
 E_{middel} &= \frac{|M_{SW}| + |M_P| + |M_T|}{\frac{|M_{SW}|}{E_{c,eff,SW}} + \frac{|M_P|}{E_{c,eff,P}} + \frac{|M_T|}{E_{cm}}} \\
 &= \frac{|-4905.91kNm| + |6401.45kNm| + |-2483.95kNm|}{\frac{|-4905.91kNm|}{10950MPa} + \frac{|6401.45kNm|}{10950MPa} + \frac{|-2483.95kNm|}{32300MPa}} \\
 &= 12430MPa
 \end{aligned}$$

where M_{SW} , M_P , and M_T are the bending moments due to the self-weight, post-tensioning load, and traffic load, respectively. These loads were applied as separate load cases, and the resulting moments were obtained for each case. Figure 40 shows, as an example, the bending moment diagram for the central 24 m when the bridge is subjected only to post-tensioning load. The cross-section in the middle of the bridge is where the moments used in the calculation of the average modulus of elasticity are taken from. It is a simplification to apply an E_{middel} calculated for the critical cross-section to the entire bridge, but it is acceptable given the conservatism. It is worth noting that the moments used in the calculation of E_{middel} are based on the assumption that the concrete material has a Young's modulus of E_{cm} , which means that only one iteration has been performed to obtain E_{middel} . Multiple iterations would yield a more precise result, naturally.

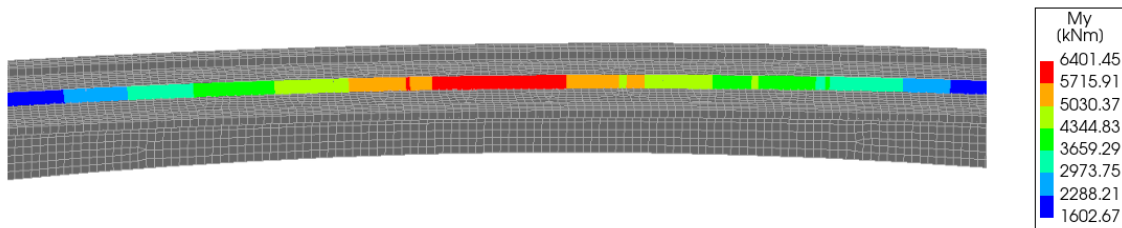


Figure 40: Moment diagram of the central 24 m, with mesh size $h = 200$ mm, when the bridge is subjected to only to post-tensioning.

As mentioned in Section 4.3.1, there are several methods for accounting for the phenomenon of creep. In this study, since a linear elastic analysis is carried out in DIANA, it was considered to ad-

opt the Principle of Superposition to account for creep. This involves conducting separate analyses for each load applied on the structure, assigned with the corresponding Young’s modulus (i.e., the effective modulus of concrete, $E_{c,eff}$, for long-term actions and E_{cm} for short-term actions), and summing the results in the end. Using the Principle of Superposition to account for creep ensures that the correct elastic modulus is used throughout the structure, yielding more accurate results. However, due to the time-consuming nature of meshing and performing linear analysis multiple times, this approach was not selected.

Shrinkage

A temperature load is defined and applied to the structural solids, i.e. the concrete elements, generating a strain that is equivalent to the effects of shrinkage. The definition of the temperature load is depicted in Figure 41, where the equivalent temperature gradient is calculated as follows:

$$\Delta T = \frac{\varepsilon_{cs}}{\alpha} = \frac{-0.233\text{‰}}{10 \cdot 10^{-6}/^{\circ}\text{C}} = -23.3^{\circ}\text{C}$$

Although the calculated equivalent temperature is -23.3°C , it was revealed during the course of the thesis work that the analysis was conducted with an equivalent temperature of -26°C . This is not a deliberate choice, but rather a result of a typing error in the modelling process. It is not clear how this affects the design moment at midspan, but testing the model indicated that the error introduced by the higher equivalent temperature of -26°C was conservative compared to the intended temperature of -23.3°C .

To enable the applied equivalent temperature load to function in the analysis, thermal expansion coefficients must be defined in the properties of all materials. The approach used to simulate shrinkage effects draws inspiration from DIANA’s official tutorial titled “Shrinkage Effects on a Concrete Slab on Ground”.

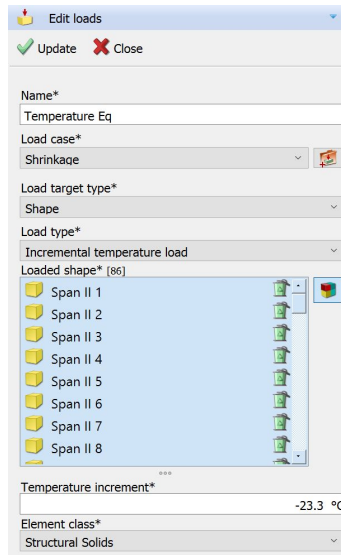


Figure 41: Definition of an incremental temperature load equivalent to the shrinkage strains.

As can be observed in the previous figure, a constant shrinkage strain is assumed over the entire structure because all the structural solids in the model are subjected to the same temperature load. The total shrinkage strain of 0.233 ‰ applies to a section in the middle of the main span and was chosen to represent the temperature gradient as a conservative estimate in a simplification.

6.4.3 Traffic Load

The traffic load is applied in DIANA using its interface, following the guidelines outlined in Section 4.2.1. The placement of vertical traffic loads on the concrete structure can be seen in Figure 42, visually illustrating the distribution. Line loads are used for the horizontal load, encompassing the breaking load and transverse force. The breaking load is positioned along the width of the carriageway, while the transverse force is modelled as a line load extending 14 m along the carriageway edge. To simulate the most unfavourable scenario, the transverse force is aligned in the same direction as the lateral displacement of the vertical traffic load from the carriageway centre line.

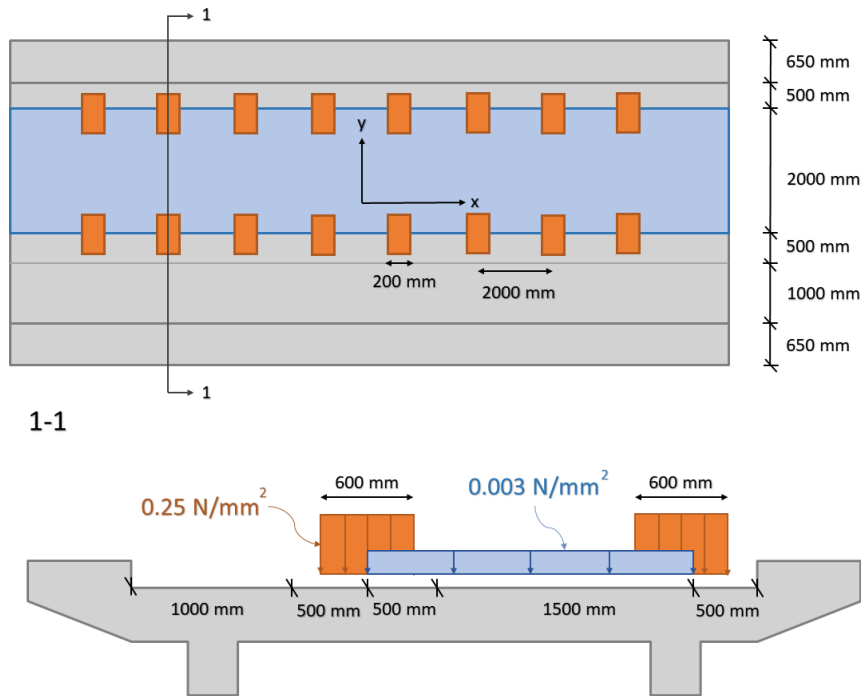


Figure 42: The vertical traffic load, where the blue colour indicates the uniformly distributed load, and the orange colour indicates the axle loads.

6.4.4 Post-Tension Load

The post-tensioning load, including the associated losses, is applied to the embedded reinforcement using the *Post-tensioning* load type, as illustrated in Figure 43. The load application is implemented through Python scripting, adhering to the specifications outlined in Section 4.3.4, which incorporates all prestress losses.

It is important to note that the wobble factor accounts for the cumulative sum of angular deviations along the length of the tendon. For instance, in the case of tendon 3NB, a manual calculation yielded an angular deviation (θ) of 0.0167045/m. By adding this value of θ to the original wobble factor of 0.002/m, an adjusted wobble factor of 0.0187045/m is obtained.

Furthermore, the active and passive anchorages are determined based on the interpretation of available drawings, as discussed in Section 3.1.3. The post-tensioning scheme follows the guidelines outlined in the *CEB-FIP Model Code 1990*.

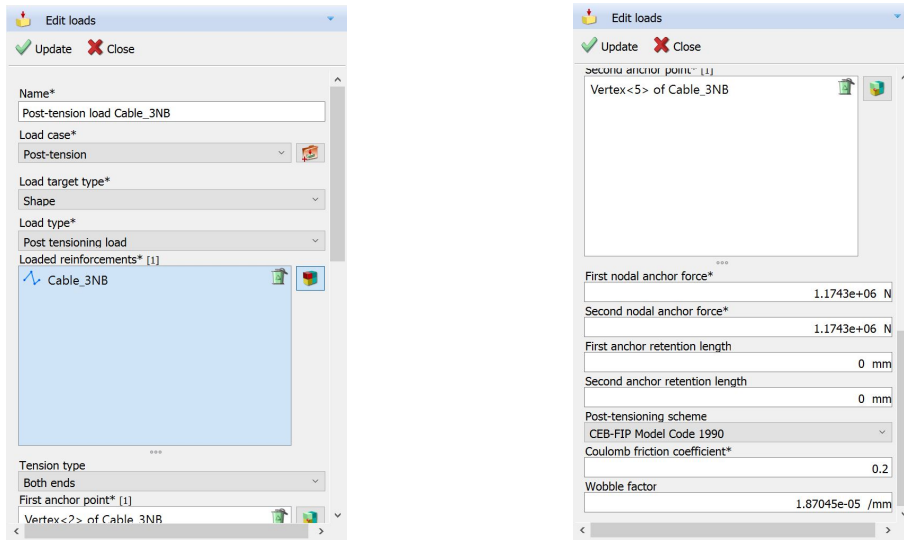


Figure 43: Prestress load reinforcement for tendon 3NB.

6.4.5 The Design Load Combination

The design load combination a , as defined in V412, corresponds to load case ULS a in the DIANA model. The representation of this load combination is shown in Figure 44.

	Selfweight Concrete	Selfweight Asphalt	Selfweight Railing	Post-tension	Shrinkage	Lorry-load Uniformly distributed load Midspan	Lorry-load Uniformly distributed load Stilespan 1	Lorry-load Uniformly distributed load Stilespan 2	Lorry-load Axial load	Horizontal Traffic Load	50 Tons Midspan
ULS a	1.15	1.15	1.15	0.9	1	1.4			1.4	1.4	
50 Tonns Test	1	1	1	1	1						1
50 Tonns Only											1

Figure 44: ULS a load case.

6.5 The Python Script for the Post-Tensioning System

The post-tension system is modelled with Python scripting. This applies to all aspects, including geometry, properties, and loads. The Python script is particularly important when later simulating damage to the system. Therefore a more detailed explanation of this is deemed relevant. This will provide an appreciation of the script but also insight into the general modelling through Python scripting. See Appendix G for the Python script.

Firstly, a coordinate list of each tendon layout is created and saved as individual CSV files. This is

done in a separate Python script that utilizes both the *reference line* and the *cross-section heights* as well as a detailed CSV file containing a description of the tendon layouts provided in Drawings 7-10 of Appendix A. The coordinate lists are subsequently stored and utilized in another Python script, which handles the modelling process.

The Python script responsible for handling the modelling process in DIANA primarily carries out three key actions. Firstly, it creates the geometry of the tendons. Subsequently, it applies parameters such as cross-sectional areas and material specifications to the tendons. Lastly, the script applies a post-tension load to the tendons. These actions are performed using functions within the *Tendon* class, which is defined within the Python script and is not a built-in function in DIANA.

By structuring the code with inspiration from object-orientated programming, i.e. dealing with classes, the script becomes easier to interpret and, if deemed necessary, change. For each tendon, an instance of the class *Tendon* is created and the three actions are executed in the initial class function, see function definition below.

```
def __init__(self, name, coordinateList, anchoredLeft, anchoredRight, area,  
    ↪ load)
```

Additionally in the initial class function, other parameters are assigned to each tendon, such as friction coefficient and wobble factor. On the note of wobble factor it is important to mention that when an instance of *Tendon* is created, the average curvature of the tendon is calculated and integrated into the wobble factor. This is done as earlier mentioned to account for friction losses due to the tendons' curvature. Further, the input parameters used to create an instance of *Tendon* are as follows:

- **name** - Name of tendon.
- **coordinateList** - List containing coordinates for the tendon.
- **anchoredLeft** - The boolean variable for the left anchorage indicating whether it is a passive anchorage (False) or an active anchorage (True).
- **anchoredRight** - Boolean for right anchorage.
- **area** - Cross-section area.
- **load** - Post-tension load, where elastic shortening and relaxation are accounted for.

In order to investigate a damaged post-tension system more effectively, it was essential to enhance the script to enable the removal of specific segments of a tendon. This is achieved by introducing a 2D list that contains intervals of x-values representing the desired removal sections, as detailed in Appendix H. By doing this, the tendon can be divided into multiple pieces, giving several tendon segments. In the Python script, each of these segments is created as separate instances of the class *Tendon*, where the ends originating from removing a part of the tendon are assigned passive anchorage, as depicted in Figure 45.

Doing this is sufficient for the case of removing central tendons where both anchors are active. However, for tendons that only have one active anchor, a further investigation into how to simulate this correctly is necessary. In DIANA a tendon with two passive anchors is considered a passive tendon without post-tension load.

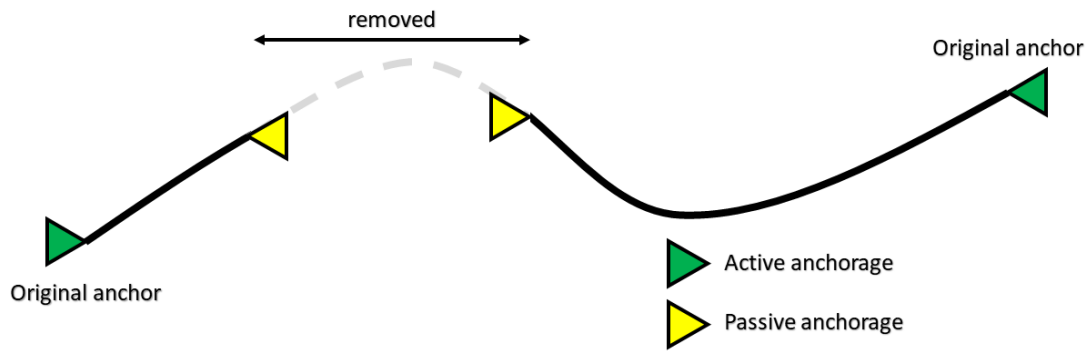


Figure 45: Anchorages originating from a tendon breakage.

6.6 Boundary Conditions

Each pier is fixed at the bottom, which simulates the connection between the column bents and the underlying rock. This ensures that any translation and rotation at the bottom surfaces of the piers is prevented, accurately representing the foundation-soil interaction.

Regarding other boundary conditions, no additional constraints are applied. The vertical supports and bridge deck were cast together, eliminating the need for specific boundary conditions at their connection.

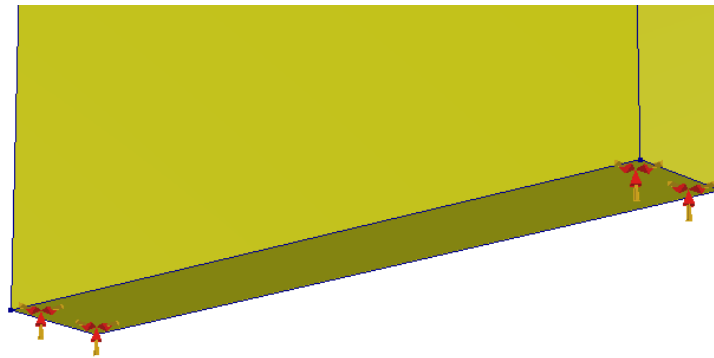


Figure 46: The boundary condition for the column at axis 4.

6.7 Meshing

The act of meshing, dividing a structure into finite elements, is mainly an automatic process done by the finite element program. However, some specifications need to be provided by the user before the meshing techniques and algorithms can generate the finished mesh. This section will therefore present the meshing-specific specifications used in the bridge model. This includes element type, element size, and meshing order. The choosing of element size is done based on a convergence study where the meshing time, analysis time, and results are considered. Meshing order, i.e. linear or quadratic mesh order, is chosen based on findings in Section 5.2 and a time study conducted on the two different meshing orders. Due to time being a relevant factor in these two studies, it is worth mentioning the specs of the computer used to carry out the studies:

- Processor: 2.38 GHz
- RAM: 8.00 GB (7.42 GB usable)

Firstly the element type was chosen as it is a critical decision that will impact the accuracy and reliability of the subsequent results. In this meshing process, the primary element type selected is the quadratic element, specifically the DIANA element HX24L. It is important to clarify that in this context, the term “quadratic element” refers to its shape, rather than the meshing order.

The HX24L element, as illustrated in Figure 47, is an eight-node isoparametric solid brick element. This element type is the preferred choice due to its superior convergence rate compared to the tetrahedral element. With the element being isoparametric, it provides great versatility by allowing arbitrary quadratic shapes of the elements (DIANA FEA_{BV}, 2022, 10.0, 11.5.4). Additionally, the mesh is supplemented by tetrahedral elements to mesh detailed geometry features.

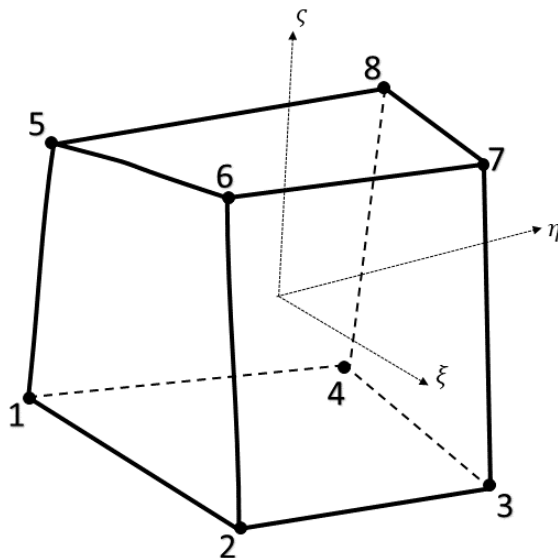


Figure 47: The HX24L element.

A time study comparing the use of quadratic and linear mesh order was conducted to assess their feasibility. The results, presented in Table 5, revealed that while quadratic meshing performed adequately for larger elements, it significantly increased analysis time when refining the mesh. Ultimately, the choice of linear meshing order was determined due to limitations in computer memory (RAM), particularly evident for element size 300 mm. It is worth noting that the test was conducted under varying circumstances, or rather, affected by available memory, which may explain the decrease in meshing time when refining from 500 mm to 400 mm.

Furthermore, considering the inclusion of the unintentional angular deviation of the tendons through the wobble parameter (as explained in Section 5.2), there were no significant advantages in opting for quadratic meshing order in the model of Herøysund Bridge. This is due to the piece-wise linear representation of most of the geometry where linear elements are sufficient, as stated in Section 2.4.3.

Table 5: Time-study comparing quadratic and linear meshing.

Element Size [mm]	Meshing		Analysis	
	Linear	Quadratic	Linear	Quadratic
500	390 s	390 s	805 s	994 s
400	312 s	510 s	878 s	1455 s
300	611 s	544 s	746 s	1350 s *

* Aborted due to insufficient virtual. memory

After selecting the element type and meshing order, a convergence study was conducted to determine the optimal element size. The study focused on evaluating stresses at the midsection when the bridge is subjected to the design load combination, considering both minimum and maximum values. The results of the study are presented in Table 6 and visualized in Figure 48. Additionally, as part of the convergence study, the maximum deflection at the midspan was evaluated when a 50-ton load was applied. This evaluation was conducted to replicate the test described in Section 7.2.1.

Based on these results, an element size of 300 mm was selected, with 200 mm elements concentrated in the central 24 m, resulting in a total of 31 800 elements. This configuration ensures a reasonable meshing time, an adequate number of elements in the cross-section height direction, and satisfactory results. It is worth noting that nodal averaging was not utilized at this stage in the project course, but its application in future analyses can enhance the convergence of stresses.

Table 6: Convergence study for the element size determination, where h denotes the element size and n the number of elements.

h [mm]	n	Time		50 Ton	ULS a	
		Meshing	Analysis	w_{max} [mm]	$\sigma_{x,max}$ [MPa]	$\sigma_{x,min}$ [MPa]
1000	6190	266 s	401 s	-29.47	8.59	-11.84
500	13120	343 s	833 s	-32.99	9.11	-12.83
300	26187	414 s	693 s	-33.70	9.21	-12.64
300 *	31800	501 s	755 s	-33.69	9.22	-12.81
200	56020	648 s	923 s	-33.86	9.25	-12.83

* The central 24 m is meshed with an element size of 200 mm.

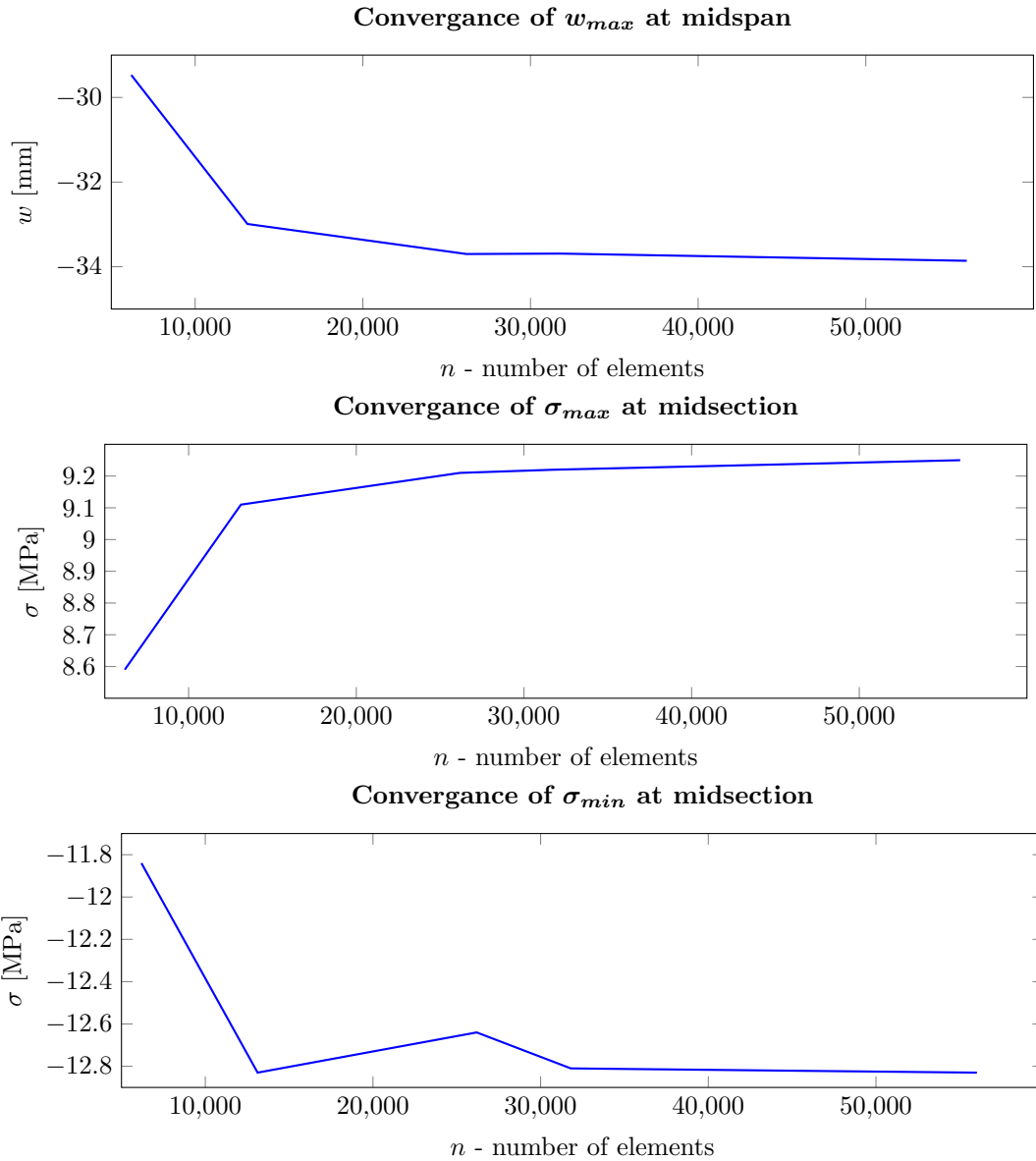


Figure 48: Plotted results from convergence study.

6.8 Post-Processing

Cook et al. (2001) describe user error when conducting a finite element analysis, and herein includes the user's inability to interpret computed results. The act of post-processing is consequently an important step in any finite element analysis. Some aspects surrounding this subject are therefore presented in this chapter.

One of the challenges of accurately presenting results is regarding the discontinuity of stresses across element boundaries. Therefore, most finite element programs provide some kind of element smoothing to produce more accurate results. In DIANA, this is done by nodal averaging (DIANA FEABV, 2022, 10.2, 21.2.1). Nodal averaging is described by Kolbein Bell (2013) as a straightforward fairly robust technique and is a common method used in many finite element programs. It involves calculating average nodal stresses by averaging the stress contributions from all the elements connected to a node.

Nodal averaging is employed in the extraction of results but was not adopted at the early stages of this thesis. It is therefore throughout the thesis specified where nodal averaging is not applied. Most importantly, this applies to the convergence study to determine mesh size.

As discussed in Section 5.1, the composed line method is employed to obtain cross-sectional forces in DIANA. This method focuses on a predefined line, known as the composed line, which the forces are evaluated along. The results obtained along this line can be visualized through contour plots or line diagrams, see Figure 49 and Figure 50 respectively.

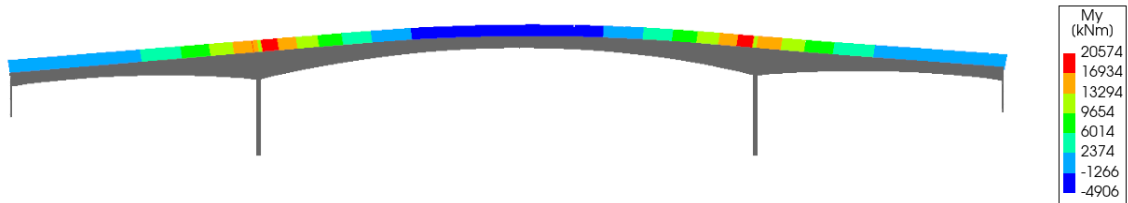


Figure 49: Contour plot of the bending moment, M_y , distribution with nodal averaging applied, depicting the effects of self-weight on the bridge.

Line diagrams prove to be particularly useful when assessing and controlling the results, as they provide a clear visualization of how the forces vary along the composed line. This provides an easy way to monitor the force distribution and understand the structural response more intuitively. Therefore, line diagrams are used continuously throughout the work as a visualization tool to control the structural response.

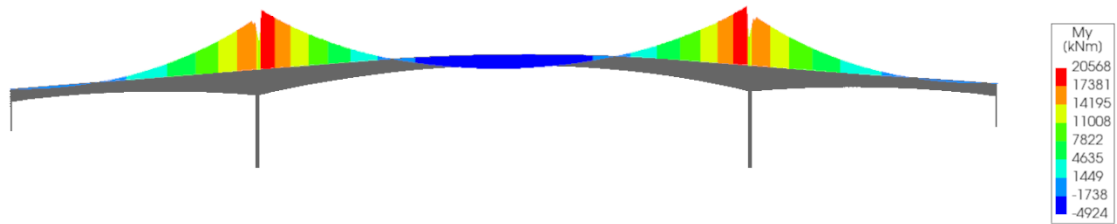


Figure 50: Line diagram of the bending moment, M_y , distribution without nodal averaging applied, depicting the effects of self-weight on the bridge.

However, it is important to note that nodal averaging could not be applied in combination with a line diagram. This limitation is considered unfortunate in DIANA's capabilities. Consequently, the extraction of results is performed using nodal averaging with contour plots.

7 Model Validation

As part of the post-processing phase when conducting a finite element analysis, it is crucial to ensure that the analysis produces anticipated results. This chapter focuses on validating the analysis by comparing the results with field tests and previous studies on the bridge’s capacity. Furthermore, the impact of not incorporating various post-tensioning phases in the bridge model is evaluated. By examining these aspects, the reliability and adequacy of the model can be established.

7.1 Stage Construction Impact

To evaluate the impact of not incorporating the various post-tensioning phases in the bridge model, an assessment was conducted on the displacement above the main piers by solely applying prestress to the central six beam tendons. The relevant tendons include 1NB+1SB, 3NB+3SB, and 4NB+4SB. This evaluation was conducted at an early stage of the model development when creep and angular deviation θ in friction loss were not accounted for, to gain insight into the potential effect. Although the mesh size was not yet optimized, a suitable element size was selected to ensure satisfactory results. The results are presented in Table 7, which indicate relatively small displacements. Therefore, it confirms the reasonable choice of not including the phased construction aspects.

Table 7: The displacement in the x-direction (DtX) at the top of the main piers when only the six central beam tendons are tensioned.

Axis	DtX
5	4.35 mm
4	-4.96 mm

7.2 Control of Model Results

7.2.1 Comparison with Measurements from Full-Scale Structural Testing

After the installation of measuring instruments, a full-scale test was conducted on the bridge on September 2, 2020, using a 50-ton semi-trailer. During the test, the semi-trailer was brought to a stop in the middle of the main span, and deformations were measured. The bridge was crossed by the trailer a total of three times, with continuous monitoring of strains. A note with the subject “18-1069 Herøysund bru. Oppfølging av instrumentering og bæreevne” prepared by Aas-Jacobsen on November 8, 2021, can be found in Brutus. This note presents the results obtained from the full-scale testing, including the measured deformations and maximum strains, which are summarised below:

- Deflection at midspan: -33 and -31 mm for north and south beam, respectively.
- Horizontal displacement at axis 1: 3-5 mm
- Horizontal displacement at axis 7: 0 mm
- Maximum strain: 0.5 ‰

A replication of the full-scale test was performed using the bridge model in DIANA. The test simulation specifically concentrated on applying a static load of 50 tons to a surface measuring 16x4

m in the middle of the main span. The vertical displacements, strains, and horizontal displacements obtained are presented in Figure 51, Figure 52 and Figure 53, respectively. As the load placement is symmetrical relative to the bridge's central axis, the displacements and strains are identical for both the south and north beams.

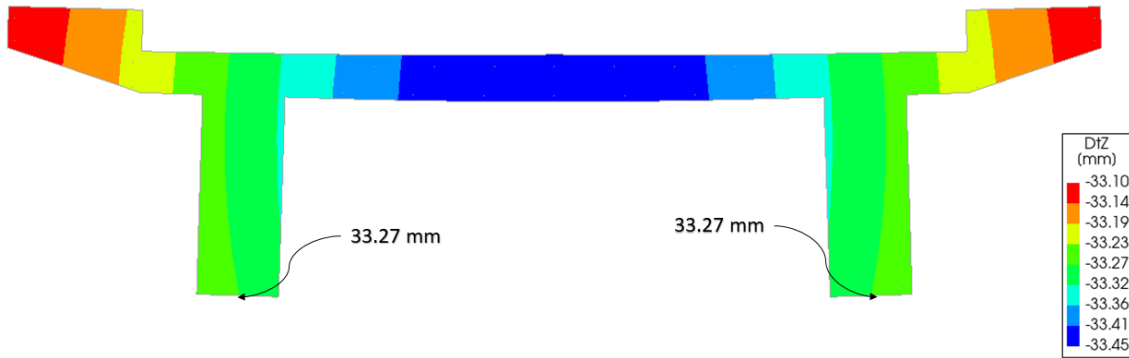


Figure 51: Vertical displacements DtZ in the middle of the main span, when the structure is only subjected to a static 50 tons load in DIANA.

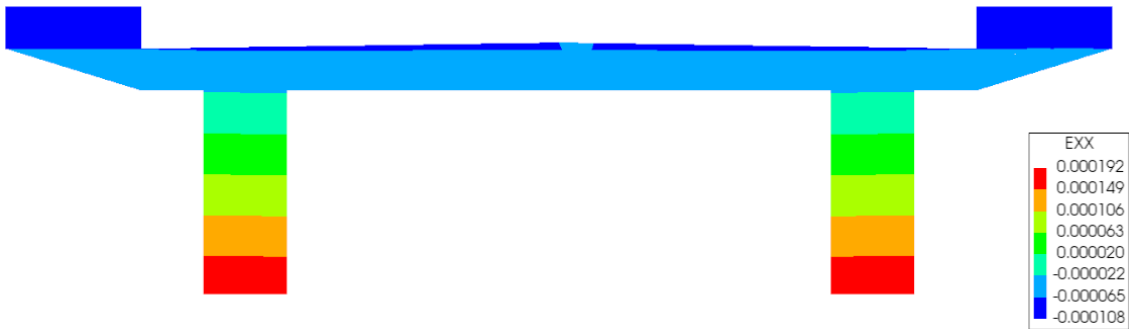


Figure 52: Strains in the x-direction, ε_x , at midsection when the structure is only subjected to a static 50 tons load in DIANA.

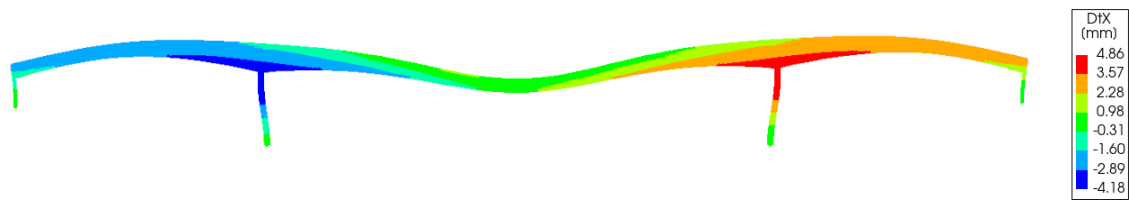


Figure 53: Horizontal displacements DtX in the bridge when it is subjected to only a static 50 tons load in DIANA.

Table 8 provides a comparison between the measurements obtained from the full-scale test and the results obtained from the test simulation. The vertical displacements show a high degree of similarity, indicating agreement between the two. However, noticeable differences are observed in the horizontal displacements, particularly at axis 7. While the measurements indicate 0 mm, the finite element analysis yields -2.3 mm. The absence of a measured horizontal displacement at axis 7 can be attributed to the accumulation of dirt in the slit.

To achieve similar horizontal displacements in the model as observed in the measurements, there was consideration given to constraining the horizontal displacements at axis 6. Therefore, in

Table 8: Comparison between the full-scale test and results obtained from Finite Element Analysis (FEA) in DIANA.

	Measurments	FEA	FEA (DtX=0 at axis 6/7)
Vertical displacement [mm]			
North beam	-33	-33.27	-30.52
South beam	-31	-33.27	-30.52
Horizontal displacement [mm]			
Axis 1	3-5	3.1	4.49
Axis 7	0	-2.3	0
Strain	0.5 ‰	0.19 ‰	0.18 ‰

Table 8, in the column indicating the displacement in the x-direction (DtX) set to 0 mm at axis 6, the results from the linear analysis are presented. However, as can be observed from the table, these results did not show significant improvement compared to the previous analysis. Therefore, it was decided to maintain the original design. Additionally, constraining horizontal movement at one of the extremities was deemed inappropriate given that the superstructure is designed to have longitudinal freedom of movement under normal maintenance conditions.

It is important to highlight that Table 8 includes horizontal displacement values for axis 1 and axis 7, even though the bridge model spans only from axis 3 to axis 6. Despite this variation, the values can still be considered comparable, assuming that some displacement is transferred from axis 3 and 6 to axis 1 and 7. As mentioned earlier in this section, the presence of dirt in the slits is highly probable. Nevertheless, it is reasonable to anticipate a certain level of displacement transfer.

Continuing with the comparison of strains, this is where the most significant deviations between the measurements and finite element analysis become apparent. The measured maximum strain is 0.5 ‰, whereas the model indicates 0.19 ‰. However, these differences are expected due to the placement of strain gauges on top of the carbon fibre plates, which are installed on the beams to enhance load-bearing capacity. Consequently, the strains are not directly measured in the concrete but rather in the carbon fibres, which are bonded to the concrete using glue. The effectiveness of this interaction, specifically how well the glue transmits the strain from the concrete to the carbon fibre straps, raises some doubts.

Given these factors, it is not surprising that the resulting strains in DIANA differ from the measured values. This disparity can also be attributed to other factors such as cracks in the concrete, for instance. It is worth noting that the carbon fibre plates are not modelled, so a larger deviation in strains is acceptable and understood. Additionally, it is possible that neither the measurements nor our model accurately captures the section strains, as both may have their limitations and imperfections.

In conclusion, the model results for the 50-ton test are considered satisfactory due to the close agreement between the measured and DIANA-calculated vertical displacements. Although the horizontal displacements exhibit some differences, they are not significantly divergent. However, it is important to note that a direct comparison of the strains is not feasible. One possible explanation for the minor disparities in displacement could be the omission of carbon fibre straps in the model. These straps enhance the stiffness of the structure, resulting in reduced deflection. Overall, considering these factors, the model performance is regarded as satisfactory for the 50-ton test.

7.2.2 Comparison of Design Moments with Report A.J. 2020

This section focuses on validating the model concerning design load effects. The design load effects obtained from analyses in DIANA are compared to those obtained by Aas-Jakobsen in Report A.J. 2020. The comparisons are presented in Table 9 and Table 10. Before discussing these comparisons, firstly, the methodology employed in obtaining the different results in DIANA and Report A.J. 2020 will be presented.

Starting with the structural linear static analysis conducted in DIANA, Figure 54 and Figure 55 depict the resulting moment distributions when the bridge is subjected to self-weight and load case ULS a, respectively. As mentioned in Section 6.8 about post-processing of FEA results, the moment distributions are obtained using the composed line method.

In Figure 55, the moments above the column at axis 4 are depicted with a contour plot and a line diagram. Note that the values presented from the line diagram are without nodal averaging. Visualizing the moments through a line diagram is only done to clearly show the moment “jumps” that occur over the supports. Importantly, the maximum moment, located above the edge of the column, is assumed as the support moment, denoted as the Support Moment in Table 10.

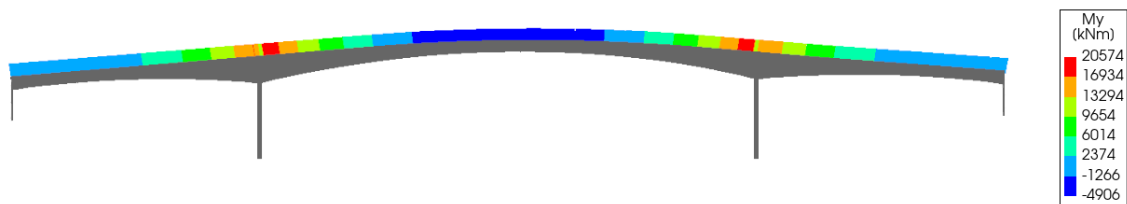


Figure 54: The moment distribution when Herøysund bridge is subjected to self-weight as the only load case.

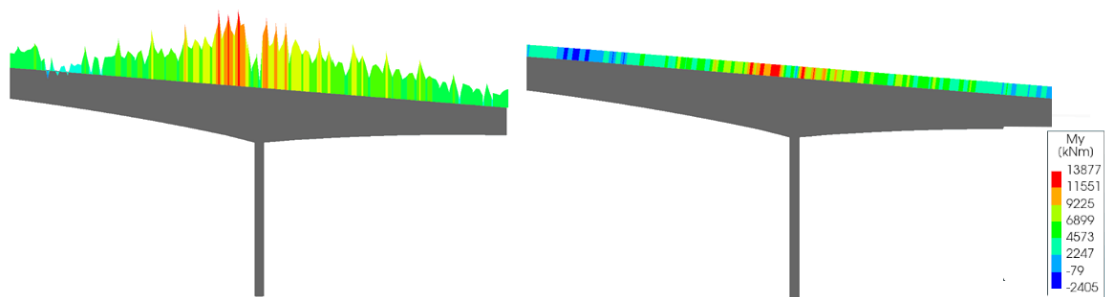


Figure 55: The moment distribution above the column at axis 3 when load combination ULS a is applied.

In Report A.J. 2020, the design load effects are obtained using NovaFrame, a space frame analysis program based on beam element theory. It is important to note that the analyses conducted by Aas-Jakobsen utilize beam finite elements, which differ from the 3D solid elements used in the DIANA model. This difference needs to be considered when comparing the results.

When modelling with beam elements, the maximum hogging moment, or support moment, can be easily extracted from the bending moment diagram. Above the main piers, the moment diagram exhibits a sharp-pointed shape, indicating the maximum value, as shown in Figure 55. Figure 55 represents the moment distribution, including the direct effect of the post-tensioning system, when the structure is subjected to load case ULS a.

The direct effect of post-tension refers to the moment generated by the eccentricity of the prestress

force, $P \cdot e$. If the direct effect of prestress is not considered, only the secondary moments resulting from the prestress force are taken into account. These secondary moments are restraint forces that arise due to the system being statically indeterminate.

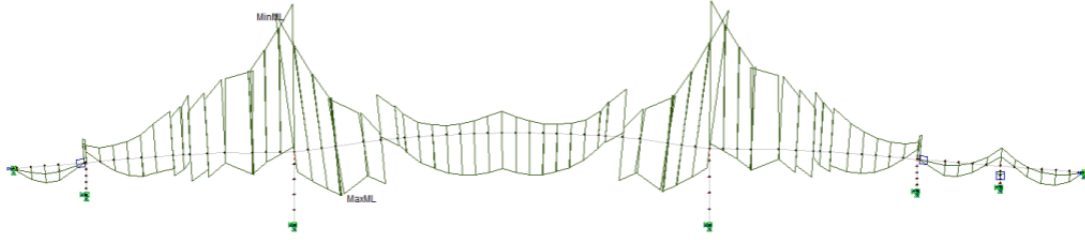


Figure 56: The moment distribution from Report A.J. 2020 for load case ULS a including direct effects of the post-tensioning. $M_{y,max}/M_{y,min} = 5\,765/-17\,369$ kNm.

Table 10 reveals relatively large deviations for the support moment when the bridge is subjected to the ULS a load case, with deviations of 20.1% and 13.1%, where the latter being without accounting for the direct effect of prestressing. The deviations can be due to the disparity in modelling approaches between DIANA and NovaFrame. NovaFrame, being a frame analysis program, represents piers as simple bars, resulting in distinct moment peaks at the middle of the piers. However, this representation of the moment distribution does not account for the thickness of the support, as is done in the 3D model within DIANA. To ensure a more accurate comparison of results, it may be appropriate to extract the support moments in NovaFrame at a distance equivalent to half the width of the support, measured from the middle of the support. This adjustment would align the modeling considerations more closely between the two programs.

Table 9: Comparison of maximum span bending moments obtained with NovaFrame in Report A.J. 2020 and the ones obtained in DIANA.

Maximum Span Moment [kNm]			
Load Case	NovaFrame	DIANA	Deviation
Self-weight	- 4 781	- 4 906	2.6 %
ULS a	- 5 765	- 3 892	-32.5 %
ULS a (without secondary effects of post-tensioning)	- 10 668	- 10 340	-3.1 %

Table 10: Comparison of support bending moments obtained with NovaFrame in Report A.J. 2020 and the ones obtained in DIANA.

Support Moment [kNm]			
Load Case	NovaFrame	DIANA	Deviation
Self-weight	20 762	20 574	-0.9 %
ULS a	17 369	13 877	-20.1 %
ULS a (without direct effect of post-tensioning)	38 706	33 650	-13.1 %

Also for maximum span moment, the results show deviations from Aas-Jakobsen's analysis, by up to 32.5% in the ULS a load combination. In this study, the largest span moment occurs in the middle of the span, unlike Aas-Jakobsen's findings, where the highest moment is reported closer to the support, as depicted in Figure 56. This discrepancy is likely due to the evaluation

of different traffic load positions to obtain the greatest span moment. Other deviations may be attributed to the application and definition of loads, as well as the calculation of post-tension losses. Furthermore, Table 11 supplements the current result comparisons by focusing solely on the moments from the ULS a load combination in the middle of the main span. The trend still indicates that this study using DIANA produces less conservative results.

Table 11: Comparing moments in the middle of the main span.

Midsection Moment [kNm]			
Load Case	NovaFrame	DIANA	Deviation
ULS a	- 4 136	- 3 892	-5.9 %

Considering the modelling differences between this study and Report A.J. 2020, the observed deviations are reasonable. It is important to mention that in Report A.J. 2020, some model input parameters were adjusted to achieve results similar to the measurements obtained during the full-scale testing. In other words, Aas-Jakobsen's study and this study have different areas of focus. This study primarily aims to model the Herøysund Bridge as built/as designed. Although the results obtained in DIANA and Report A.J. 2020 are not directly comparable, it can be confidently concluded that the bridge model in this study is accurate, as the results are in the same area as those in Report A.J. 2020.

8 ULS Capacity Assessment

This chapter presents the results from a linear static analysis conducted in DIANA of Herøysund Bridge in its intact state, as intended at the time of design. The ultimate moment of resistance, M_{Rd} , is then calculated for the section of interest and compared to the design moments, M_{Ed} , obtained from the analysis in DIANA. This allows for an evaluation of the bridge's capacity at midspan, which is a key objective of this work. It is important to note that while ULS design involves several verifications, this thesis will only assess the bridge's bending capacity.

8.1 Analysis Results

The design bending moment resulting from a linear static analysis conducted in DIANA, for the central span of Herøysund bridge when subjected to only the design load combination ULS a, is shown in Figure 57. ULS a load combination is considered as the design load case for the midsection, and the bending moment about the y-axis induced by this is therefore denoted by $M_{y,Ed}$. It can be observed from the figure that the design moment in the midsection is -3 892 kNm. It should be noted that the results are based on only one load case of ULS a, wherein the traffic load is positioned to be the most unfavourable for the moment at the midsection.



Figure 57: Distribution of bending moments, $M_{y,Ed}$, along the central part when the bridge is subjected to load case ULS a.

8.2 Ultimate Moment of Resistance

When Herøysund Bridge is subjected to sagging bending moments, the bridge deck functions as a compression flange. Therefore, to calculate the moment capacity of the midsection, the cross-section is idealized as a double tee or double-T beam, which resembles two T-beams connected side-by-side. Figure 58 shows the transformation from the original cross-section, which is provided in Appendix B, to a double tee, along with relevant geometric data, including effective flange width parameters. The flange thickness, t , is set to 215 mm, which is an average value. The effective flange width, b_{eff} , is determined in accordance with clause 5.3.2.1 of Eurocode 2 as:

$$b_{eff} = \sum b_{eff,i} + b_w \leq b,$$

where

$$b_{eff,i} = 0.2b_i + 0.1l_0 \leq 0,2l_0$$

and

$$b_{eff,i} \leq b_i.$$

The effective width of the flange is based on l_0 , which is the distance between points of zero moments. This distance is read from the moment diagram depicted in Figure 57, and in this case, is 30 m when rounded off. With l_0 set to 30 m, and b_1 , b_2 and b_w being 0.95, 1.30, and 0.40 m, respectively, the effective flange width, b_{eff} , is calculated to be 2.65 m, which means that the entire flange width is effective.

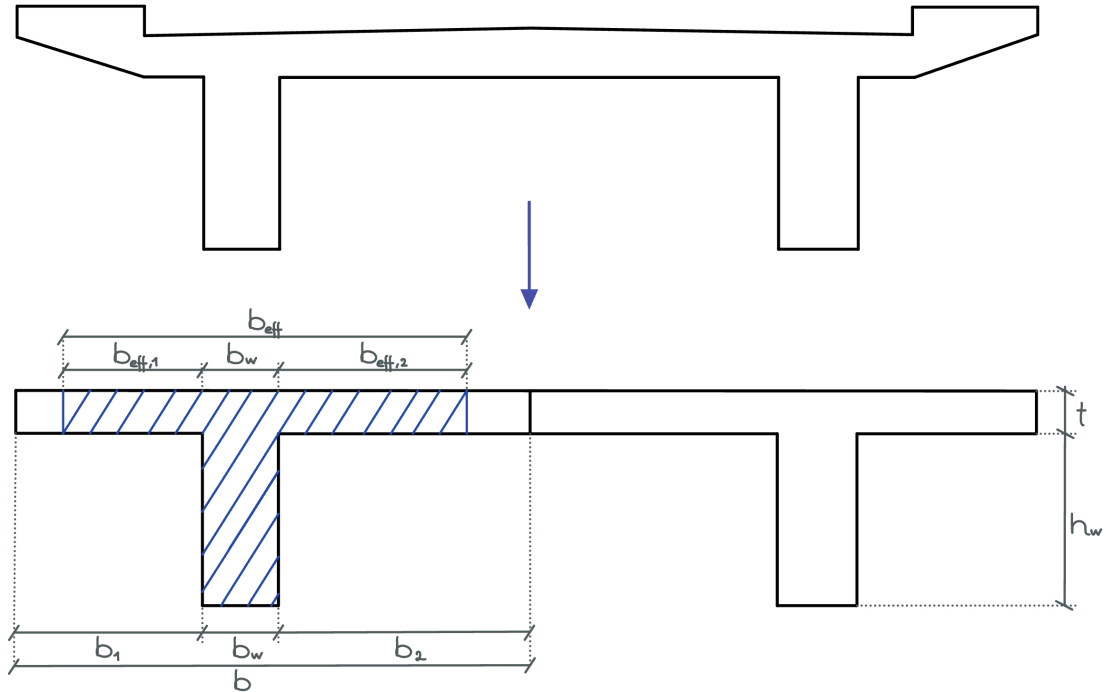


Figure 58: The original cross-section is idealized as a double-T beam to simplify the capacity calculations.

The procedure for moment capacity calculations of a T-section is detailed in Chapter 4.2.4 of Sørensen's book, "Betongkonstruksjoner" (Sørensen, 2013). According to the chapter, the flange's dimensions are typically large enough that the height of the compression zone becomes small, resulting in significant reinforcement strains before the concrete reaches its ultimate compressive strain. In this scenario, it is reasonable to assume constant compressive stress in the flange only, with the resultant compressive force acting in the middle of the flange thickness. This assumption is undertaken in the calculation of the ultimate moment of resistance of the section of interest. It is important to note that the nonlinear behaviour of concrete is taken into account, where the compressive stress in concrete in the ULS is represented as a rectangular stress distribution.

Additionally, it is assumed that the contribution from the longitudinal passive reinforcement to the moment capacity is negligible. This assumption is justified because only corner bars are placed in the tension side of the beam, and it is concrete that mainly takes up the compressive stresses. To visualize the resulting stress and strain distribution in a T-section, or rather half of an idealized double-T beam, refer to Figure 59.

Equation 14 can be used to express the ultimate moment of resistance, assuming prestress as internal resistance in an intact bonded section, and considering equilibrium about the midpoint of the flange thickness.

$$M_{Rd} = f_{pd} \cdot A_p \cdot \left(d - \frac{t}{2} \right) \quad (14)$$

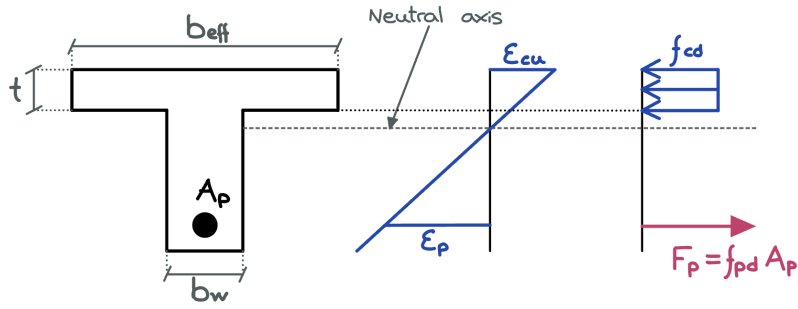


Figure 59: Strains and stresses in a T-section with only prestressing reinforcement.

To calculate the moment capacity of Herøysund Bridge, it is necessary to multiply M_{Rd} by two since the section of interest consists of two T-sections, each containing four tendons at the same height. Based on this approach, the designed ultimate moment of resistance for the midsection of the bridge is 13 254 kNm, as shown in the calculation below:

$$M_{Rd} = 2 \cdot \left(\frac{1520 \text{ MPa}}{1.15} \cdot 4 \cdot 1244 \text{ mm}^2 \cdot \left(1115 \text{ mm} - \frac{215 \text{ mm}}{2} \right) \right) = 13254 \text{ kNm}$$

One must also verify that the moment capacity is within safe limits. This is accomplished by ensuring that $\sigma_{cd} \leq f_{cd}$, which is the case here, as demonstrated below:

$$\sigma_{cd} = \frac{M_{Rd}}{t \cdot b_{eff} \cdot \left(d - \frac{t}{2} \right)} = \frac{0.5 \cdot 13254 \cdot 10^6 \text{ Nmm}}{215 \text{ mm} \cdot 2650 \text{ mm} \cdot \left(1115 \text{ mm} - \frac{215 \text{ mm}}{2} \right)} = 11.5 \text{ MPa} < f_{cd}$$

8.3 Moment Capacity Assessment

The ultimate moment of resistance calculated for the midsection is determined to be 13 254 kNm, while the design moment obtained from the linear static analysis in DIANA yields a magnitude of 3 892 kNm. Consequently, the utilization ratio at the midsection is calculated to be 29.4%. However, it is important to note that the moment capacity of the cross-section may be slightly lower due to the presence of voids in the ducts, which leave the tendons partially unbonded. In an unbonded system, the prestressing strands are free to move locally relative to the concrete, not achieving strain compatibility between materials. This is resulting in less contribution to the structure's ultimate strength and a force in the prestressing reinforcement that is less than the steel strength f_{pd} . As a result, the moment capacity is affected if there is a long zone in the midspan without grout. Therefore, the utilization ratio at the midsection may be slightly higher than calculated.

Furthermore, it is valuable to examine relevant research pertaining to the influence of grouted and ungrouted tendons on moment capacity. Terje Kanstad's doctoral thesis from 1990, titled "Nonlinear Analysis Considering Time-dependent Deformations and Capacity of Reinforced and Prestressed Concrete", demonstrates that an unbonded system exhibits a comparable capacity to that of a bonded system. This finding is further corroborated by the R&D study named "Ekstern Forspenning i Betong", conducted by Berdal Strømme A.S. for the NPRA in May 1993. These studies lend support to the approach adopted in this thesis for assessing the bridge's capacity.

It is worth noting that the utilization ratio of only 29.4% at the midsection appears relatively low. However, it is important to acknowledge that the original design calculations for the bridge are unavailable. Considering the absence of longitudinal reinforcement in the beams, except for the corner bars, it is reasonable to assume that the bridge was designed to prevent tensile stresses in

the cross-section. This assumption aligns with the historical context of the bridge's construction in 1966, predating the implementation of Limit State Design (LSD) in Norway in 1973. Before LSD, prestressed concrete was dimensioned based on simplified stress states, with the criterion that tensile stresses should be eliminated. This design approach resulted in an excess capacity, as the tensile capacity of the reinforcement remained underutilized, and the concrete exhibited no cracking. These factors likely contribute to the observed low utilization ratio at the midsection of the bridge.

9 Study of the Post-Tensioning System with Damage

This chapter aims to investigate the behaviour of the bridge when subjected to damage in the post-tensioning system. The presence of severe corrosion in the post-tensioning system, particularly in the large void spaces of the ducts, increases the likelihood of wire breakages. Therefore, studying the effects of such damage is highly relevant. It is important to note that this study focuses specifically on the consequences of severe corrosion damage that lead to tendon breakage. Partial section loss of the steel is not the primary focus; instead, the emphasis is on situations where corrosion is severe enough to cause tendon rupture.

Various damage models, ranging from simple to complex, can be developed and analyzed. In this thesis, two separate studies will be conducted using DIANA. The first study evaluates the bridge's capacity at the midsection under successive tendon breakages, while the second study examines the effect of induced damages at different positions along a specific tendon on the design moment. These studies represent two among several possible approaches to studying the post-tensioning system with damage.

To simulate a damage scenario in the DIANA model of Herøysund Bridge, either a portion or the entire tendon can be removed from the model. Complete removal of a tendon can be easily achieved by deleting the associated geometry and loading through DIANA's interface. Additionally, partial removal of a tendon is feasible using the Python script employed for creating the post-tensioning system.

Figure 60 illustrates the placement of the different central tendons in the beams at the midsection. These cables have the same eccentricity at the midsection, resulting in the same primary moments when prestress losses are disregarded. However, each tendon has a different layout throughout the bridge, leading to distinct contributions to the constraint forces in the structure. Understanding how the secondary moments influence the design moment is crucial, particularly for comprehending and discussing the upcoming results.

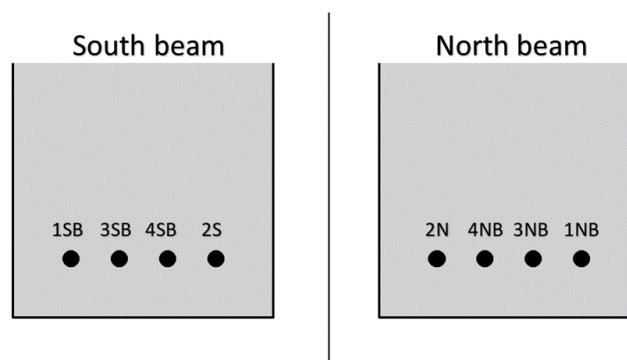


Figure 60: Tendon placement in the midsection.

As mentioned, various approaches can be employed to study the post-tensioning system with damage. However, a more precise and well-grounded study of the post-tensioning system in Herøysund Bridge with damage is deemed necessary, surpassing the analysis conducted by Aas-Jakobsen. Of particular concern is the significant omission in the existing capacity assessment, where the influence of prestressing reinforcement on the cross-sectional moment capacity is entirely neglected. This omission raises doubts about the accuracy of the obtained results and the overall comprehension of the bridge's behaviour when subjected to damage. It is worth noting that Report A.J. 2020 includes a capacity control scenario in which sufficient capacity is demonstrated to be achieved

in all sections by assuming 50% of the tendons are grouted and thus bonded. However, in this capacity control scenario, the damage scenario is simplified by reducing the area of all prestressing reinforcement by 50%, resulting in a calculation of M_{Ed} and M_{Rd} that incorporates 50% less prestressing reinforcement area.

9.1 Successive Tendon Breakages

In this study, the concept of a damaged tendon involves the complete removal of the tendon and its associated load within the DIANA model. This removal has an impact on both the design moment and the moment capacity of the structure. By calculating these values, it becomes possible to identify a critical point where the design moment matches the moment capacity. This critical point indicates the maximum number of cables that can be removed before the capacity at the midsection is no longer sufficient.

9.1.1 Method

To simulate successive tendon breakages, each tendon is successively removed from the model, and the analysis is performed for each case. This approach allows for the determination of the design bending moment at the midsection, denoted as $M_{y,Ed}$, under different damage scenarios. It is important to highlight that only the central tendons, which span through the midsection, are removed, while the rest of the post-tensioning system remains unaffected.

The study begins by examining the impact of removing each central tendon individually. This analysis is particularly significant as it enables the ranking of tendons based on their effect on the design bending moment, $M_{y,Ed}$. Table 12 presents the influence of each individual tendon removal on the design moment, along with $\Delta M_{y,Ed}$, indicating the extent of change compared to the undamaged state. This information is utilized to determine the order of tendon removal, aiming to create the most unfavourable scenario of successive tendon breakages. Accordingly, the order of removal is as follows: 4NB, 4SB, 3NB, 3SB, 2N, 2S, 1NB, and 1SB. Notably, the contribution from a tendon in the north beam is equivalent to the corresponding tendon in the south beam.

Table 12: ULS a bending moments, i.e., $M_{y,Ed}$, when tendons are removed successively.

Damaged Tendon	$M_{y,ED}$ [kNm]	$\Delta M_{y,ED}$ [kNm]
1NB/1SB	-4 152	-260
2N/2S	-4 231	-339
3NB/3SB	-4 234	-342
4NB/4SB	-4 293	-401

This being a linear analysis, the principle of superposition applies when considering the prestressing force on the action side. This means that the effect of removing tendons successively could be determined by adding each tendon's individual impact on the design moment presented in Table 12. However, with the tendons also contributing to the stiffness of the structure, the damage study must be conducted with the combined removal of the tendons.

Although the tendons in Herøysund Bridge do contribute to its stiffness, it remains uncertain whether DIANA considers this stiffness contribution when the tendons are modelled as unbounded. To investigate this aspect, a study is conducted comparing two different approaches, with a focus on tendons 1NB, 2S, and 4NB. Firstly, the total increase in the design moment is calculated by summing up the moment increases obtained from removing each tendon separately, as shown in

Table 12. Additionally, a collective removal analysis of all tendons is performed, and the resulting increase in design moment is recorded. The discrepancy between these two tests is found to be 5 kNm, indicating that DIANA does consider the stiffness of the post-tension system. This finding underscores the need to proceed with the study using the combined removal of tendons.

Once a clear understanding of obtaining the design moment for each damage scenario is obtained, the bending moment capacity is calculated for each case. It is important to note that each tendon contributes equally to the capacity since they all have the same eccentricity and cross-sectional area. An updated assessment of the midsection’s capacity is conducted for the removal of varying numbers of tendons, following the guidelines outlined in Section 8.2.

9.1.2 Results and Discussion

Table 13 and Figure 61 present the outcomes of the study investigating the sequential removal of tendons. As mentioned earlier, the removal order is as follows: 4NB, 4SB, 3NB, 3SB, 2N, 2S, 1NB, and 1SB. The parameter n represents the total number of removed tendons. Therefore, when n equals 0, it signifies the healthy state of Herøysund Bridge. As n increases, it denotes the removal of additional tendons, such as tendon 4NB ($n = 1$), tendons 4NB and 4SB ($n = 2$), tendons 4NB, 4SB and 3NB ($n = 3$), and so on, until reaching $n = 8$.

The analysis results in DIANA demonstrate that four tendons can be removed while the bridge still maintains sufficient capacity at the midsection. This finding aligns with Report A.J. 2020, where it is stated that all sections have sufficient capacity when 50% of the prestressing reinforcement area is incorporated in the capacity assessment.

It is important to note that the ultimate moment of resistance becomes zero when all central tendons are removed. Although this assumption is not entirely accurate, it is necessary for the capacity assessment of the post-tensioning system with damage to be comparable to the assessment conducted on the healthy state bridge in Section 8. Both assessments must follow the same calculation procedures and assumptions. Another crucial point is that the plot in Figure 61 is conservative. In reality, the blue graph would be lifted higher and the red line lowered further due to the inclusion of safety factors in the calculations of M_{Ed} and M_{Rd} .

Although this study makes a broad assumption by assuming the complete loss of a tendon when damaged, it can still provide useful insights for the research project on Herøysund Bridge. It can serve as a tool or indicator within the bridge’s condition monitoring system. As the bridge’s condition is continuously monitored, detecting each individual tendon breakage may be possible, and this study can be utilized as an indicator to determine when the bridge is in a safe operational state and when it is not. Strain jumps could potentially be used to identify tendon ruptures. Currently, the bridge remains close to $n = 0$, and this study demonstrates that the bridge can withstand a few tendon breakages, indicating its safety.

Table 13: Absolute value of design bending moment, M_{Ed} , and moment capacity, M_{Rd} , for the section in the middle of the main span containing n removed tendons.

n	0	1	2	3	4	5	6	7	8
$ M_{Ed} $ [kNm]	3892	4293	4721	5215	5709	6111	6513	6810	7106
$ M_{Rd} $ [kNm]	13 254	11 596	9 939	8 283	6 626	4 967	3313	1657	0

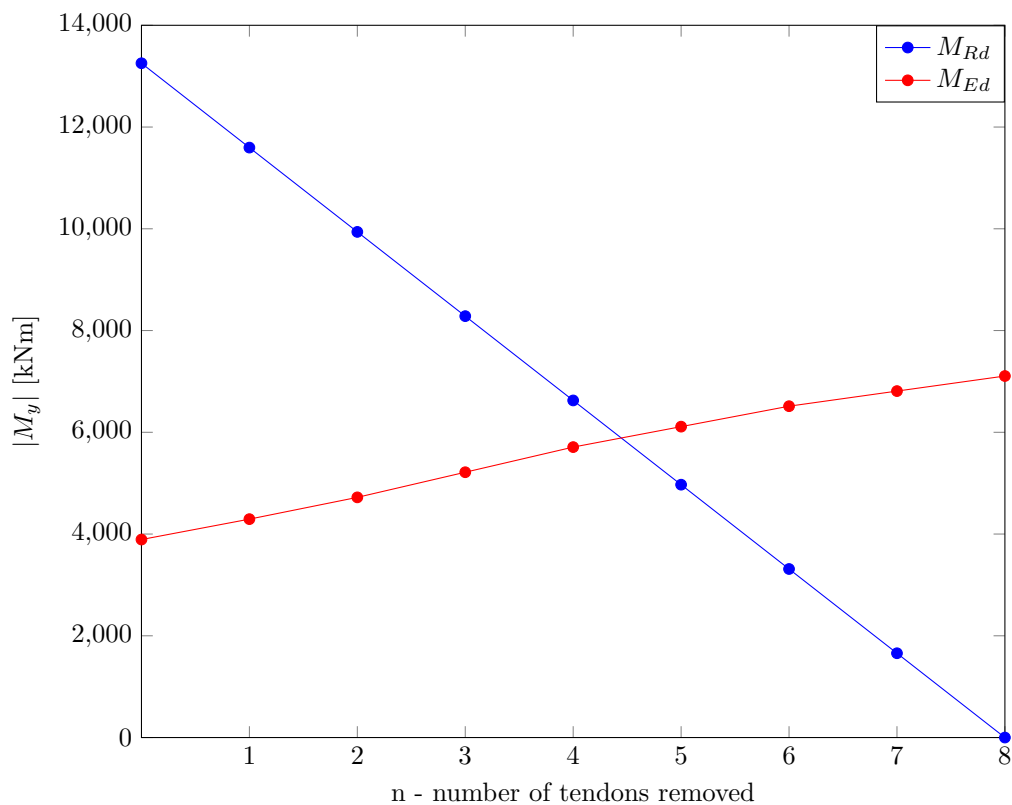


Figure 61: The design moment and ultimate moment of resistance at midsection with varying amount of tendons. Note: Design moments are negative from DIANA.

9.2 Refinement of the Damage Model

In this section, the study of the post-tensioning system with damage is refined by narrowing the focus to a single tendon. The refined study involves inducing varying degrees of damage at different positions along the tendon. In this context, inducing damage refers to the removal of the tendon.

The motivation behind this study arises from significant sections of the bridge's central region suffering from poor grouting, as presented in Section 3.4. Inadequately grouted areas are prone to corrosion, increasing the likelihood of wire breakage. Hence, it is valuable to investigate the impact of different degrees of damage at various positions along the tendon on the design load. Consequently, the focus will shift from capacity assessments to analyzing the actual effect of varying damage scenarios on the design moment at the midsection. It is worth noting that capacity assessments are not relevant in this context since the emphasis is solely on one tendon, and previous findings have already demonstrated sufficient capacity at the midsection when one tendon is removed.

9.2.1 Method

To gain a better understanding of the current state of damage in the bridge and determine the most relevant tendon to induce damage on, consultation was sought from Professor Roy Johnsen, an esteemed expert in corrosion monitoring and corrosion management at the Department of Mechanical and Industrial Engineering, NTNU. Prof. Johnsen is actively involved in the research project on Herøysund Bridge and has extensively worked on mapping areas with poor grouting. He provided an overview of ultrasound measurements that highlighted the central top tendons as

being particularly vulnerable to insufficient injection. Based on this information, tendon 4NB was selected as the target for the refined study.

Considering the study’s focus on inducing damage at different positions along tendon 4NB, two variables are defined:

- *Extent* (E): This variable specifies the extent of the damage, encompassing the void and transmission length.
- *Location* (L): This variable indicates the precise location of the damage.

A detailed explanation of these variables is necessary. Starting with E , its minimum value is 0 m, representing an undamaged, healthy state, while the maximum value is 30 m, indicating the complete removal of tendon 4NB from the DIANA model. Excluding the undamaged state, the minimum extent is defined as the transmission length, which refers to the distance along the prestressed tendon required for the transfer of prestress to the surrounding concrete upon tendon release. In other words, when a tendon rupture occurs, the prestress force will be re-established after a certain length known as the transmission length, due to the bond between the wires and the grout. This length is calculated in Appendix E and is determined to be 3 m.

Figure 62 provides a visual representation of E when it equals 12 m. The illustration depicts the removal of 6 m of the tendon on each side of the damaged location, totalling 12 m. This configuration applies when the combination of E and L ensures that the damage does not exceed the physical length of the tendon. However, if the variable combination indicates damage extending beyond the tendon’s boundaries, an E value of 12 m implies the removal of 12 m of the cable either to the right or left of the damage location. Consequently, for a minimum damage extent located at the beginning of the tendon, only the transmission length in one direction, i.e., 3 m, is considered. This configuration was done with the intent of creating a 3D plot. The 3D plot was later disregarded in this thesis, as it did not provide valuable insight, but the points of interest remain.

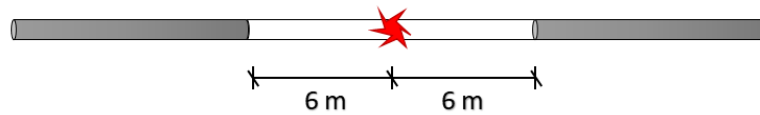


Figure 62: Damage extent of 12 m ($E = 12$ m).

Moving on to the explanation of variable L , its minimum value is 0 m, representing the starting point of the tendon, or rather, the anchorage, while the maximum value is 15 m, corresponding to the midsection. The selected values of L are based on the ultrasound measurements provided by Prof. Johnsen, which indicated that tendon breakages were most likely to occur at the following locations:

- 1-2 m from the centre of the bridge (to each side)
- 6-7 m from the centre (to each side)

Given this information, it was decided to perform a linear analysis on the bridge with damage located at the midsection, 2 m from the midsection, and 6 m from the midsection. The corresponding damage scenarios are presented in Figure 63.

Lastly, it is important to mention that while damaging tendon 4NB in the DIANA model, the original anchorages are preserved, and a passive anchorage is introduced at the “new ends” resulting from the damage.

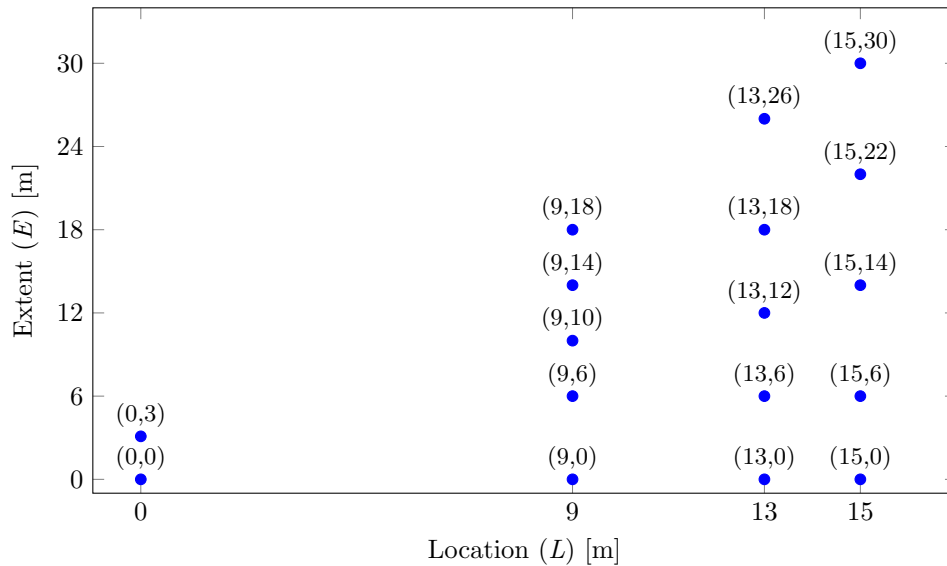


Figure 63: The studied damage scenarios.

9.2.2 Results

The results are presented in Table 14 and visualized through plots in Figure 64. Initially, it was anticipated that the results would follow a similar pattern to those of the previous study, with a roughly linear increase in the design moment as more of tendon 4NB was removed. However, the obtained results deviate slightly from the expected pattern. While there is an overall increase in the design moment when the tendon is damaged, the plots also reveal a slight decrease within certain ranges of E . Additionally, significant moment increases are observed at specific E values, such as $E = 12$ when $L = 13$, although this value appears to vary for each location.

Taking the damage at the midsection ($L = 15$) as an example, after an initial moment increase, there is a slight decrease before it resumes growth around an E value of 22 m.

Due to the relatively uncertain nature of the observed plot patterns, further studies were conducted on simpler cases, which are detailed in the subsequent section. This approach aims to provide clearer and more comprehensible explanations for the observed results before engaging in discussions and drawing conclusions.

Nevertheless, despite the uncertainties surrounding the observed plot patterns in Figure 64, one notable observation can be made. When the extent parameter is fixed at 6 m, the design moment at different damage locations increases as the location approaches the midsection at $L = 15$ m. This can be observed in Figure 65. However, it is important to note that the design moment remains the same for damages located at $E = 9$ m and $E = 13$ m. This implies that the same extent of damage becomes more critical as it occurs closer to the midsection of the bridge.

Table 14: Results from the refined damage model.

Location (L) [m]	Extent (E) [m]	$M_{y,Ed}$ [kNm]
0	0	-3 892
	3	-3 899
9	0	-3 892
	6	-4 126
	10	-4 145
	14	-4 102
	18	-4 283
13	0	-3 892
	6	-4 124
	12	-4 318
	18	-4 276
	26	-4 276
15	0	-3 892
	6	-4 328
	14	-4 283
	22	-4 264
	30	-4 291

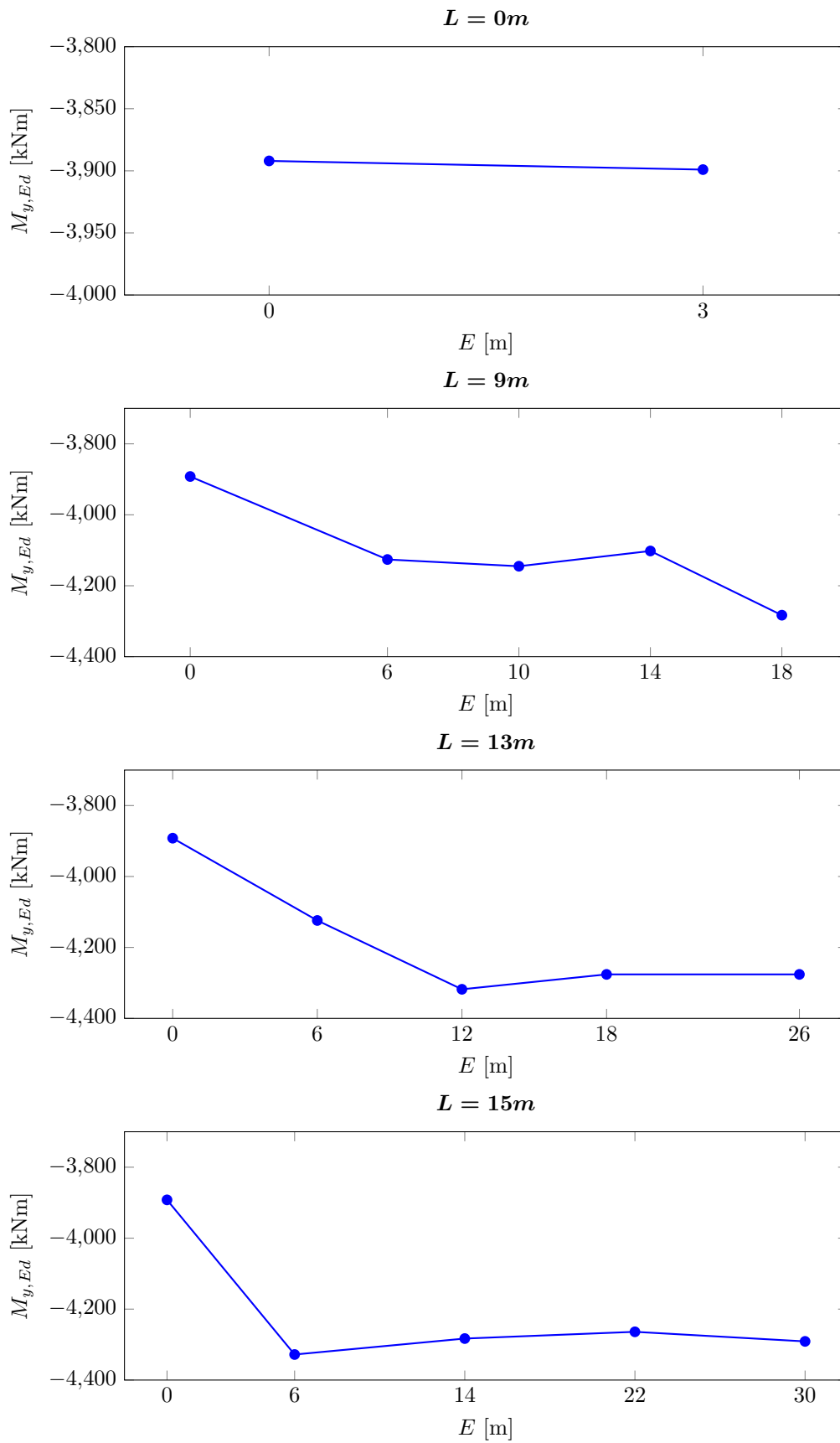


Figure 64: Design bending moments resulting from damages of different extent (E) induced at different positions along tendon 4NB.

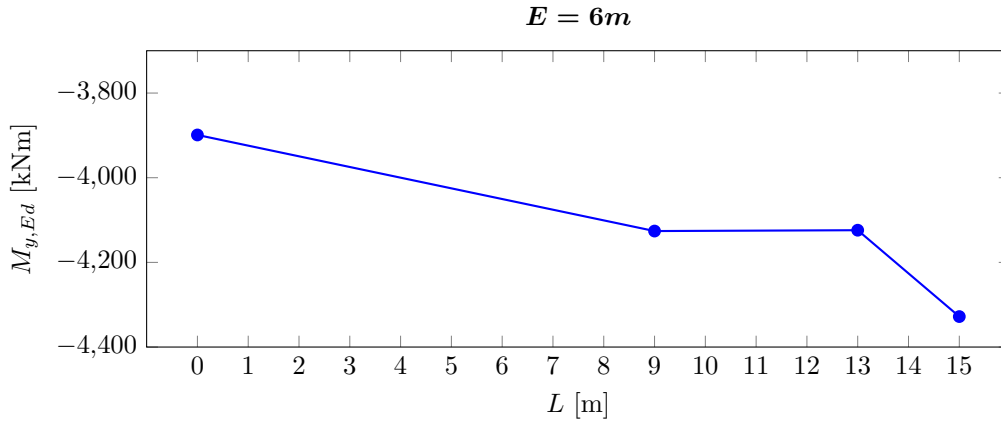


Figure 65: Design bending moment resulting from damages at different locations (L) with the minimum extent of 6 m except at $L = 0$ m where $E = 3$ m.

9.2.3 Exploratory Studies for Result Interpretation

To validate the results obtained from the refined study, a series of simplified cases are modelled in DIANA and subjected to static linear analysis. These cases aim to replicate certain aspects of the original bridge model. All cases consist of beams with a prestressing reinforcement cross-sectional area, A_p , of 1244 mm^2 , and are subject to a post-tension load of 1000 kN. The analysis focuses solely on the response to the post-tensioning load, as it is the primary area of interest.

In these simplified studies, damage is induced at the midsection of each beam. The extent of the damage is still determined by the variable E , with the minimum value remaining the same, but the maximum value is now constrained to 10 m, which corresponds to the length of a span in each beam case. The following simplified cases are considered:

1. Simply supported beam.
2. Three-span continuous beam, representing a statically indeterminate structure.
3. Three-span continuous beam supported by columns, providing some stiffness against rotation and lateral displacement.
4. Three-span continuous beam with a curved tendon layout and supported by columns.

In the following pages, depictions of each beam configuration are shown, and the linear analysis results in DIANA for each of these simplified cases are presented and plotted.

9.2.3.1 Case 1 - Simply Supported

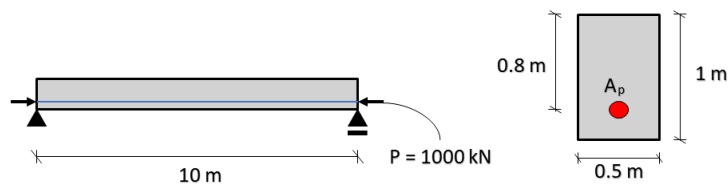


Figure 66: Case 1 - simply supported beam with a straight tendon.

The first case examines a simply supported 10 m beam, as illustrated in Figure 66. This configuration is modelled to assess how DIANA responds to the removal of tendon parts. By inducing the damage in the middle of the tendon, the primary moment is instantly removed from the midsection, aligning with expectations. Figure 67 illustrates that the bending moment resulting from the post-tensioning load does not change due to an increased extent. These findings indicate that some of the results observed in the refined study are influenced by the restraint forces induced by the system's static indeterminacy.

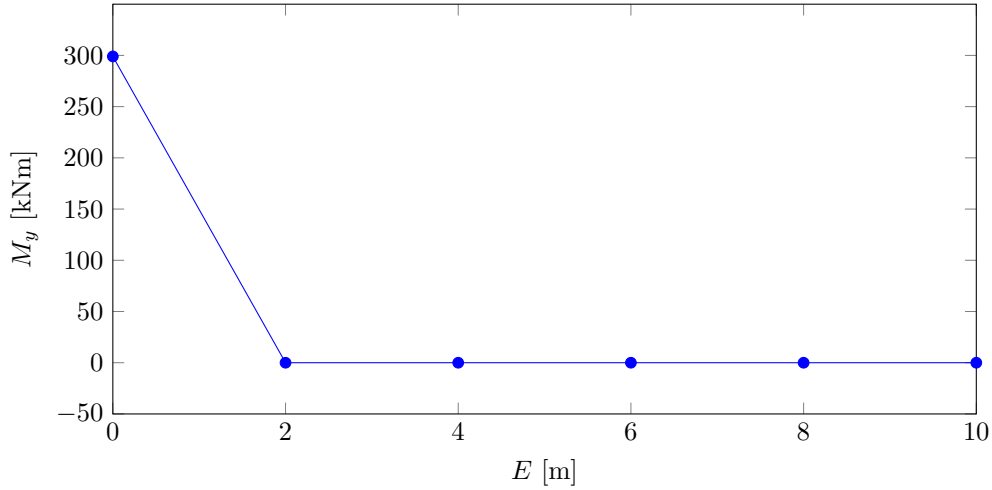


Figure 67: Moments at midsection with different damage extents for case 1.

9.2.3.2 Case 2 - Three-Span Continuous Beam

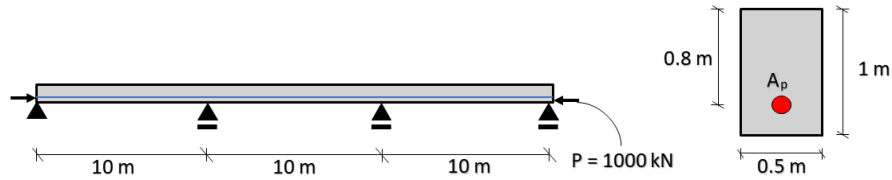


Figure 68: Case 2 - three-span continuous beam with a straight tendon.

A three-span continuous beam, as shown in the figure above, is investigated to explore the influence of a statically indeterminate system on the results. Similar to Case 1, the primary moment is eliminated from the midsection upon the first case of damage, resulting in a significant increase in the design moment, as observed in Figure 69. However, this case diverges from the first case as the extent increases beyond $E = 2$ m. With further extent increments, the moment exhibits a linear decrease. This behaviour aligns well with the response of the bridge model at extent values less than 60% of the tendon and is further explored by theory.

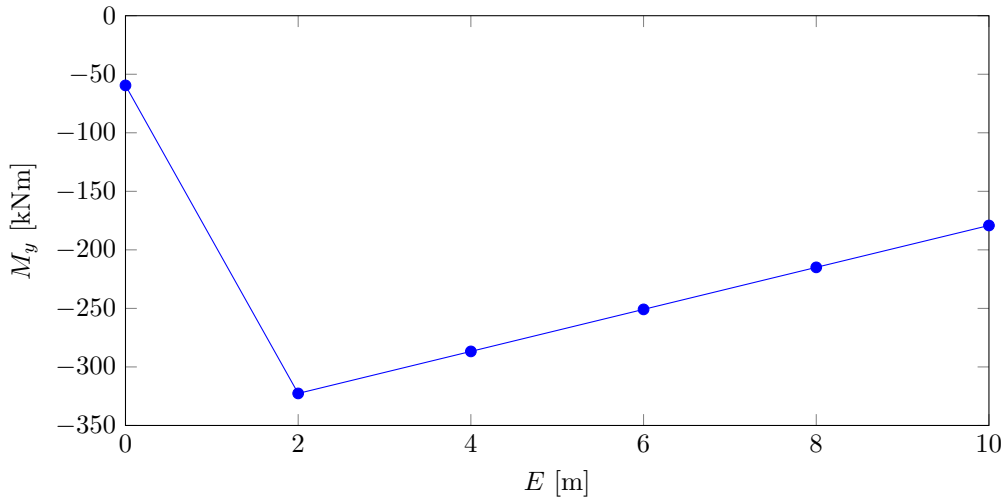


Figure 69: Moments at midsection with different damage extents for Case 2.

As explained by Sørensen (2013), the secondary moments resulting from prestress can be determined by considering the displacements the beam would experience if not restrained. Exploring this approach gives an understanding of why the secondary moments decrease for E -values greater than 2 m. Firstly, it is imperative to look at the behaviour of the primary moment, which is equal to the prestressing force times the tendon's eccentricity, when a segment of the tendons is selectively removed. In theory, this will only result in removing the primary moment from that part of the beam, as shown in Figure 70.

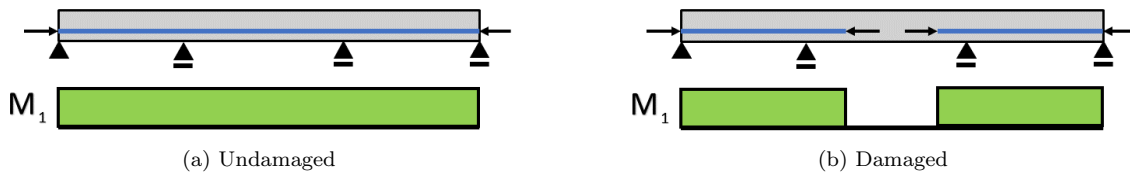


Figure 70: The primary moment M_1 distribution for case 2.

Furthermore, the behaviour of secondary moments resulting from constraints at the supports is investigated. According to Figure 71 and Sørensen's explanation, these moments directly correspond to the displacement experienced by the beam in the absence of the middle supports. When parts of the post-tensioning are removed, it becomes evident that the mentioned displacement decreases. This observation is also supported by studies conducted in DIANA. Consequently, a decrease in displacement leads to reduced constraint forces, ultimately resulting in decreased secondary moments at the midsection. Considering the absence of the primary moment at the midsection, this effect explains the decrease in moment exhibited by the midsection when E increases.

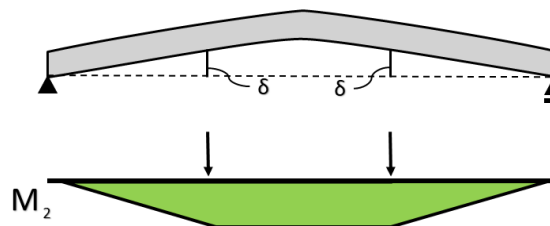


Figure 71: Secondary moment M_2 distribution in case 2.

9.2.3.3 Case 3 - Three-Span Continuous Beam Supported by Columns

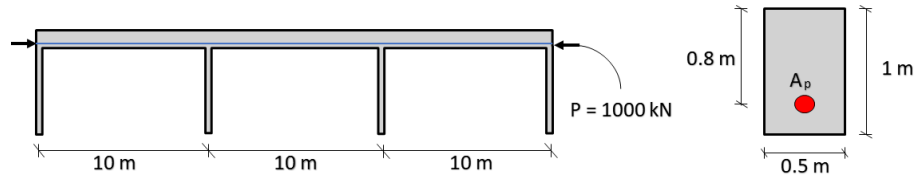


Figure 72: Case 3 - three-span beam with a straight tendon supported by columns.

This particular case is specifically designed to replicate one of the distinctive characteristics of the bridge, namely its partial restraint against bending and lateral displacement at the supports. To achieve this, concrete columns are introduced at each support, as depicted in Figure 72. The obtained result shows minimal variation compared to case 2 and exhibits a similar trend. While the increased restraint system affects the secondary moment, the overall behaviour remains consistent with the results obtained in case 2 when removing more sections of the tendon. The corresponding plot can be seen in Figure 73.

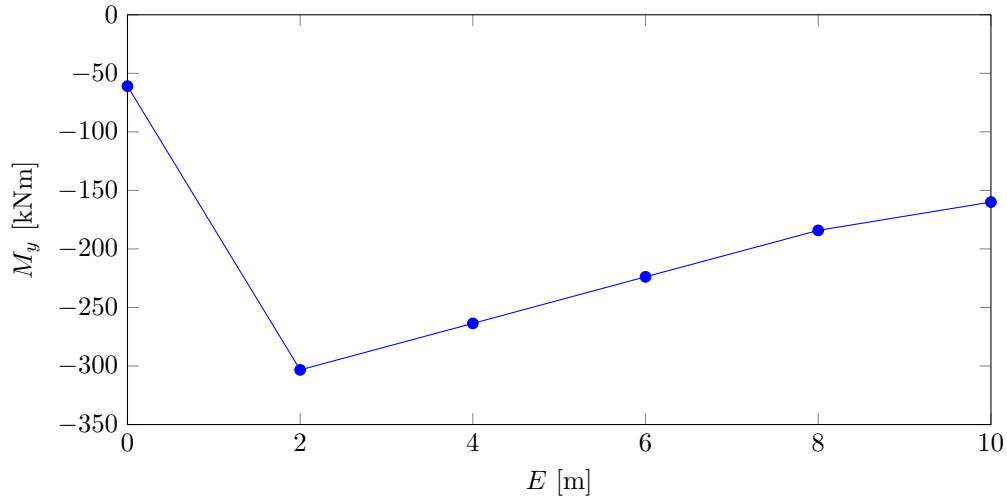


Figure 73: Moments at midsection with different damage extents for case 3.

9.2.3.4 Case 4 - Curved Tendon Layout

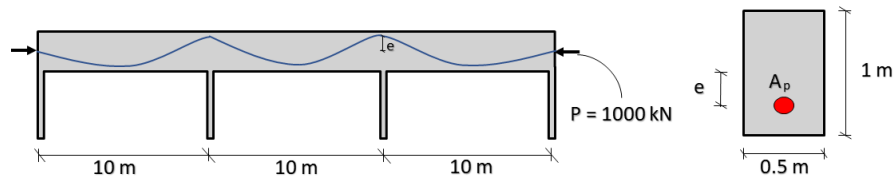


Figure 74: Case 4 - a three-span beam supported by columns with a curved tendon having the extreme eccentricities $e_{max} = 0.4 \text{ m}$ and $e_{min} = -0.4 \text{ m}$.

To simulate another notable feature of Herøysund Bridge, a simplified model with a curved tendon layout is analyzed, as illustrated in Figure 74. The obtained results from this study align closely with the results observed in the bridge model. It demonstrates a similar trend of a decreasing

bending moment, as seen in Case 2 and Case 3, during the initial stages of damage. Additionally, it exhibits a slight increase in the bending moment for larger extents. This appears to happen when the extent exceeds the area where the tendon's eccentricity moves above the centre of the area of the concrete cross-section.

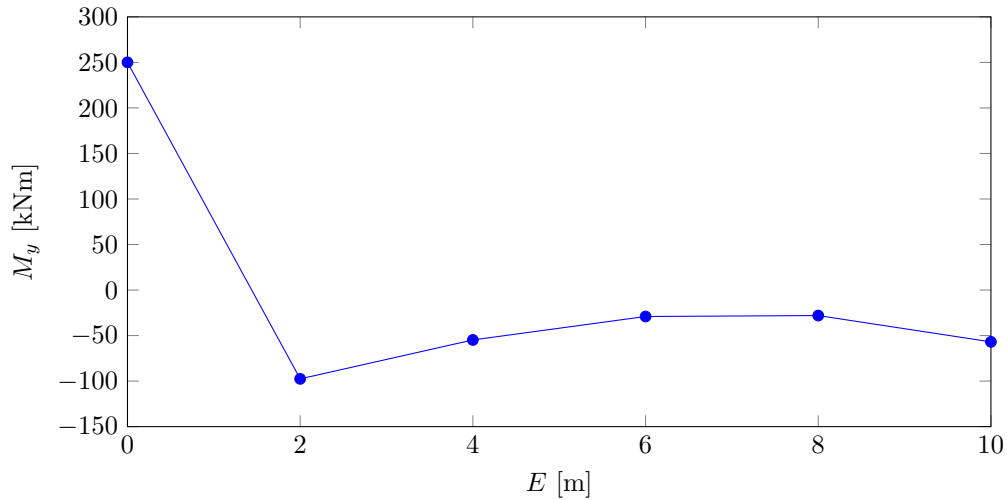


Figure 75: Moments at midsection with different damage extents for case 4.

9.2.4 Discussion

The results obtained from conducting linear analysis on the simplified cases confirm the accuracy of the findings obtained in the refined study, which involved inducing varying degrees of damage at different locations along tendon 4NB.

In post-tensioned structures, the design moment encompasses both primary and secondary moments, commonly known as isostatic and hyperstatic moments, respectively. The most significant change in the design moment at the midsection of the Herøysund bridge occurs when the contribution of the primary moment is eliminated, as observed when there is no tendon 4NB present in the midsection. Hence, the primary moment has a significantly greater impact on the design moment.

In the absence of isostatic moments contributing to the design moment, the design moment becomes dependent on the distribution of hyperstatic moments. However, as the extent of damage increases and there is no tendon 4NB in the midsection, the variation in secondary moments is generally small. It is important to note that the secondary moments are influenced by nodal moments that arise due to the introduction of additional anchorage forces P' , as schematically illustrated in Figure 76. The magnitude of the nodal moment depends on the placement of P' relative to the neutral axis of the cross-section.

Another crucial aspect to consider when analyzing the results is that the removal of tendon 4NB from a section reduces the stiffness in the indeterminate structure, leading to lower stress and consequently less moment in that section. Stresses tend to follow the path of higher stiffness. This may partially explain why, for example, the design moment for $L = 15$ m (see Figure 64) slightly decreases between $E = 6$ m and $E = 22$ m.

If all damages in the bridge were known and a comprehensive overview of these damages was available, along with an exact capacity assessment to be conducted, the significance of accurately modelling the location and extent of each damage becomes evident. This study emphasizes the importance of precisely representing the location and extent of every damage. For instance, when

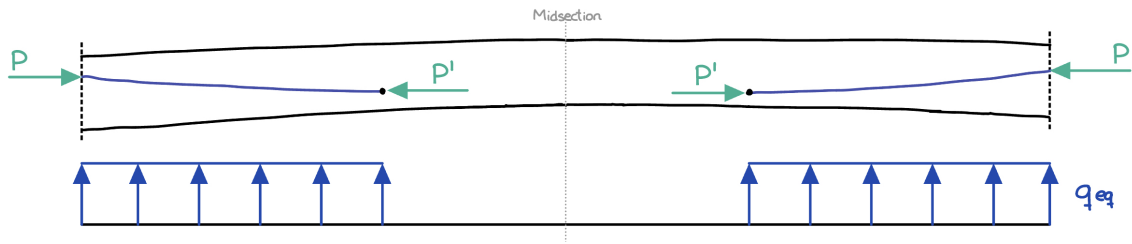


Figure 76: Schematic representation of Herøysund bridge at the midsection, demonstrating the removal of a section of tendon 4NB. This removal leads to the introduction of additional anchorage forces and the elimination of the equivalent load, q_{eq} , dependent on the prestressing force and the tendon layout over this distance.

damage occurs at the beginning of the tendon, it has the potential to regain its prestress force before reaching the midsection, resulting in minimal impact on the design moment at that specific section. This observation is reflected in the results for $L = 0$ m. However, the removal of the post-tensioning force at other sections may render those sections more critical than the midsection.

10 Conclusion

In this thesis, a detailed model of Herøysund Bridge is successfully modelled. The model is deemed accurate and the numerical results are reasonable after conducting a model validation.

First and foremost, the model's response, i.e. displacement at midspan, to a 50 tons load complies well with field testing. Additionally, design load effects are corresponding well with the results from Report A.J 2020. This confirms that the geometry and material parameters are modelled effectively, and indicates that the loads, especially load combination ULS a, are modelled correctly and according to regulations. Herein, assumptions done in this thesis regarding loads and geometry are deemed reasonable. This includes the way of considering the prestress losses, creep and shrinkage, and the post-tension system, including how the anchorages are defined. It should be noted that load effects such as creep and shrinkage have minimal impact compared to self-weight, prestress load, and traffic load. As a result, the obtained results offer more accurate insights into the proper modelling of these loads compared to creep and shrinkage loads.

The result from the capacity assessment on the healthy state bridge, i.e. the bridge as designed and intended at this time, shows a utilization ratio of 29.4% at the midsection. Given the assumption that the midsection is the most critical area, this suggests that the bridge is highly over-dimensioned with regard to service class Bk 10/50. This is confirmed by the low passive reinforcement amount in the beams, suggesting that the bridge was designed to eliminate tensile stresses in the concrete, resulting in a high moment capacity.

The study of the post-tensioning system with damage, conducted by successively removing the central tendons from the bridge model in DIANA, reveals that it is possible to remove up to four tendons without exceeding the moment capacity at midspan. Although this assumption of complete tendon loss in case of damage is a simplified one, the results still hold value as an indicator for an enhanced condition monitoring system. By detecting individual tendon breakages, this damage study can be utilized as an indicator to assess the safety of the bridge's operational state.

Further investigation of the damaged bridge by focusing on a single tendon and inducing varying degrees of damage at different positions along the tendon reveals important insights. It can be concluded that not all damages are necessarily critical, but the impact on the design moment in a specific section heavily depends on the extent and location of the damage. The location of the damage becomes crucial, particularly when conducting a capacity assessment, as the primary moment is disregarded in that specific section. Additionally, the conducted parametric study provides valuable information by examining the effect of the damage extent. Currently, if a tendon breakage were to occur in Herøysund Bridge, NPRA would likely assume the extent to encompass the entire tendon. However, this study demonstrates that such an assumption is not reasonable in a capacity assessment. Therefore, this research offers important considerations for accurately assessing the effects of tendon damage to make informed decisions about the bridge's structural capacity.

Moreover, the study of the post-tensioning system with damage serves as a prime example that creating a detailed model, including inspected damages, does not necessarily require significantly more time and skills compared to modelling without considering the damage. By employing systematic digitization of the modelling and assessment process, as demonstrated through Python scripting in this project, it becomes feasible to streamline and automate assessment procedures. Conducting thorough condition analysis of damaged bridges, integrating defects into structural models, facilitates accurate models and analyses, and thus improved decision-making capabilities. This approach contributes to increasing the service life of existing structures, resulting in cost-effective and environmentally friendly solutions. Furthermore, the continuous development of

BIM technology will further enhance the efficiency and effectiveness of these analyses. Embracing these approaches will advance bridge engineering practices and ensure sustainable management of infrastructure assets.

11 Further Work

As this thesis is written as one of the first concerning Herøysund Bridge within the broader research project *Green Management of Infrastructure Structures*, it is deemed important to present some topics of interest for further work. Through our work on this bridge, we have identified specific topics that warrant further investigation and exploration.

In this thesis, the evaluation of capacity focused solely on the midsection, which was assumed to be the most critical. However, when dealing with a damaged post-tension system, this section may not necessarily be the critical one. Other sections of the bridge exhibit different tendon eccentricities, meaning that the removal of specific tendons could have a greater impact on the design moment at these locations. Conducting a more detailed analysis that considers multiple sections would provide valuable insights.

The tendons in Herøysund Bridge were modelled as unbonded, although in reality, they are bonded to the surrounding concrete through grouted ducts. However, there are concerns regarding the quality of the grouting. While the difference between modelling the tendons as unbonded versus bonded is assumed to be small, it is important to accurately represent the bridge's intended design. Therefore, it would be beneficial for future research to explore the implications of modelling a bonded post-tensioning system for linear analysis in DIANA. By examining the effects and potential differences between bonded and unbonded tendon modelling, a more comprehensive understanding of the bridge's behaviour can be obtained.

Another recommendation for future research is to conduct probabilistic studies, specifically focusing on structural reliability assessments that incorporate a proper representation of engineering uncertainties. The objective is to determine the probability of failure. A fundamental reality in practical engineering is that our understanding of the world, especially its future aspects, is not exact but can be estimated or predicted by considering the inherent uncertainties associated with incomplete knowledge. This holds true, particularly for the case of Herøysund Bridge, where uncertainties arise concerning the bridge's damaged condition and its impact on structural behaviour.

In this master's thesis, a parametric study was conducted on the post-tensioning system with induced damage, where varying degrees of damage were simulated by removing the tendon at different positions. The study focused on two key variables: the extent variable (E) and the location variable (L). However, for future research, it is recommended to enhance the analysis by incorporating probabilistic models to represent these variables. By doing so, it would be possible to capture the inherent uncertainties associated with the extent and location of the damage.

A potential avenue for future research is to conduct a conditional probability study, which examines the probability distribution of the extent variable given the occurrence of rupture due to corrosion in a tendon. This would allow for a more comprehensive understanding of the bridge's behaviour under uncertain damage conditions. It is important to note that this suggestion is not an envisioned future research direction but rather an example of the potential applications of probabilistic studies, based on the parametric study conducted in this thesis. Such probabilistic studies could provide valuable insights into the bridge's reliability and aid in making informed decisions regarding its maintenance and operational safety.

Bibliography

- Ahlström, J. (2015). *Corrosion of steel in concrete at various moisture and chloride levels*. (Report 2015:133). Energiforsk. Available at: <https://energiforskmedia.blob.core.windows.net/media/21240/corrosion-of-steel-in-concrete-energiforskrapport-2015-133.pdf>.
- BBR (2004). *Innovative Engineering Review*. (Report 1-2004). Switzerland: BBR. Available at: http://bbr-conex.hr/download/brochure/60_years_BBR.pdf.
- Bell, K. (2013). *An Engineering Approach to Finite Element Analysis of Linear Structural Mechanics Problems*. Bergen, Norway: Fagbokforlaget.
- Brekkehus, A. (2023). 'SINTEF: Milliarder å spare med smartere forvaltning av infrastruktur'. In: Available at: <https://www.bygg.no/sintef-milliardere-a-spare-med-smartere-forvaltning-av-infrastruktur/1518112!/>. Visited on 29/03/2023.
- Bureau BBR (1969). *BBRV Tendons of large Capacity with Wires or Strands, for Nuclear-Reactor-Vessels*. (Report 6901). Zürich, Switzerland: BBR VT International.
- Cook, R. D. et al. (2001). *Concepts and Applications of Finite Element Analysis*. 4th ed. United States: John Wiley & Sons, Inc.
- DIANA FEABV (2022). *User's Manual*. Available at: <https://dianafea.com/diana-manuals/>. Visited on 05/06/2023.
- Fuhaid, A. F. A. and A. Niaz (2022). *Carbonation and Corrosion Problems in Reinforced Concrete Structures*. 12 (586). Available at: <https://doi.org/10.3390/buildings12050586>. Visited on 29/01/2023.
- Gilbert, R. I., N. C. Mickleborough, and G. Ranzi (2017). *Design of Prestressed Concrete to Eurocode 2*. 2nd ed. Boca Raton, Florida, United States: CRC Press.
- Hangaard, L. and M. Aasheim (2018). *Analyse av FFB-bru med korrosjonsskadede spennarmering*. Master thesis. Department of Structural Engineering, NTNU.
- HOS (2019). *Kapasitetskontroll for katodisk beskyttelse og påstøp av bruer*. (Report 12019-03-01). Oslo, Norway: Aas Jacobsen.
- Imbsen, A. A. et al. (1985). *Thermal Effects in Concrete Bridge Superstructures*. (Report 276). Washington, D.C., United States: Transportation Research Board, National Research Council. Available at: https://onlinepubs.trb.org/Onlinepubs/nchrp/nchrp_rpt_276.pdf?fbclid=IwAR2aKa0y9S4_m8JCzXMowwwcYTOtEppC67fjINj0uQi0SVW_Bq2cAZYQL3Zc.
- Johnsen, R. (2022). *Herøysund bru, korrosjon av etterspent armering*. (Report 843). Statens Vegvesen. Available at: <https://vegvesen.brage.unit.no/vegvesen-xmlui/handle/11250/3016945>.
- Kristian, T. (2021). *Brua under bygging*. Available at: https://no.wikipedia.org/wiki/Herøysundet_bru#/media/Fil:Herøysundet_bru_under_bygging.jpg. Visited on 05/06/2023.
- Lau, K. and I. Lasa (2016). *Corrosion of prestress and post-tension reinforced-concrete bridges*. In Lau, K. and I. Lasa (red.) *Corrosion of Steel in Concrete Structures*. Florida, United States: Elsevier. Available at: <https://doi.org/10.1016/B978-1-78242-381-2.00003-1>.

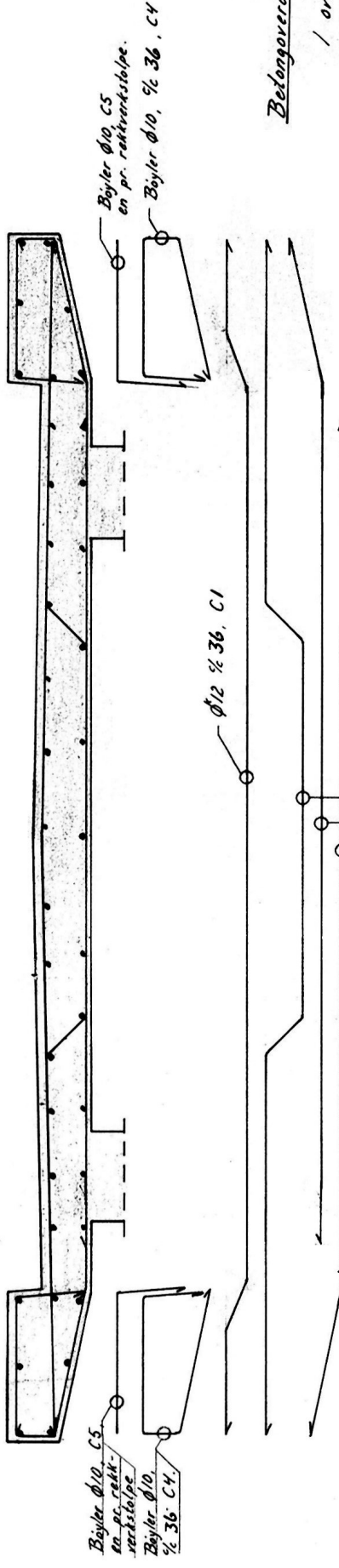
-
- Magar, A. (2021). *Critical Loads for Bridge Substructure as per IRC 6*. Available at: <https://www.midasbridge.com/en/blog/bridgeinsight/critical-load-for-bridge-substructure-as-per-irc-6#none>. (Visited on 24/03/2023).
- Musach, M. T. (2020). *Post-tension concrete beam modelling and analysis in DIANA via Python*. Bachelor thesis. Department of Structural Engineering, NTNU.
- PCA (2023). *Corrosion of Embedded Metals*. Available at: <https://www.cement.org/learn/concrete-technology/durability/corrosion-of-embedded-materials>. (Visited on 25/02/2023).
- Pinto, G. and D. Cantero (2022). *Modelling post-tensioned structures with DIANA FEM software*. (ISBN: 978-82-7482-201-6). Trondheim, Norway: NTNU. Available at: <https://ntnuopen.ntnu.no/ntnu-xmlui/handle/11250/3034405>.
- Saksberg, B. (1998). *Herøysund bru - Statisk beregning og kapasitetskontroll*. (Report 110-98). Oslo, Norway: Aas Jacobsen.
- Siem, B. (2022). *5600 bruer har skadar som reduserer trafikktryggleiken: - Det er skummelt*. NRK. Available at: <https://www.nrk.no/vestland/5600-bruer-har-skader-som-reduserer-trafikktryggleiken-1.15921518>. Visited on 29/03/2023.
- Skoglund, J. (2022). *100 millioner FoU-kroner til to veirelaterte prosjekter for reduserte klimautslipp*. Veier24.no. Available at: <https://www.veier24.no/artikler/100-millioner-fou-kroner-til-to-veirelaterte-prosjekter-for-reduuerte-klimautslipp/524567>. Visited on 29/03/2023.
- Sørensen, S. I. (2013). *Betong-Konstruksjoner, Bergning og dimensjonering etter Eurocode 2*. 2nd ed. Bergen, Norway: Fagbokforlaget.
- Staberg, M. and S. R. Olaisen (2022). *Skal la brua kollapse for hindre nye brukollapser*. NRK. Available at: https://www.nrk.no/nordland/forskning-kan-forhindre-brukollapser_-vil-spare-100-milliarder-1.16146940. Visited on 27/01/2023.
- Standard Norge (2003). *Eurocode 1: Laster på konstruksjoner - Del 2: trafikklast på bruer*. Available at: <https://online.standard.no/ns-en-1991-2-2003na-2010>.
- Strängbetong (n.d.). *BBRV Spennarmering*. Strängbetong.
- Sveen, A. (2020). *18-1069 Herøysund bru. Bæreevneberegninger*. (Report 18-1069). Aas Jacobsen.
- (2021). *18-1069 Herøysund bru. Oppfølging av instrumentering og bæreevne*. (Report 19-1069). Aas Jacobsen.
- Vegdirektoratet (2021a). *Håndbok V412, Bæreevneklassifisering av bruer, laster*. Available at: <https://store.vegnorm.vegvesen.no/v412>. Visited on 05/06/2023.
- (2021b). *Håndbok V413, Bæreevneklassifisering av bruer og materialer*. Available at: <https://store.vegnorm.vegvesen.no/v413>. Visited on 05/06/2023.
- Vestad, H. and M. Vestad (2021). *Non-linear Behaviour of Insufficiently Grouted Post-Tensioned Concrete Members*. Master thesis. Department of Structural Engineering, NTNU.
-

Appendix

A Drawings

Appendix containing drawings from Norwegian Public Roads Administration, Brutus.

- **Drawing 1:** Bridge geometry with coordinates for center line and beam heights.
- **Drawing 2:** Geometry of main piers, at axis 4 and 5, and pressure plate.
- **Drawing 3:** Reinforcement drawing of passive reinforcement in bridge deck.
- **Drawing 4:** Reinforcement drawing of passive reinforcement in main piers, at axis 4 and 5, and pressure plate.
- **Drawing 5:** Reinforcement drawing depicting the active and passive reinforcement in the western approach span.
- **Drawing 6:** Reinforcement drawing depicting the active and passive reinforcement in the eastern approach span.
- **Drawing 7:** Post-tension tendon drawing of tendons located in the beams (1).
- **Drawing 8:** Post-tension tendon drawing of tendons located in the beams (2).
- **Drawing 9:** Post-tension tendon drawing of tendons located in the beams (3).
- **Drawing 10:** Post-tension tendon drawing of tendons located in the deck.

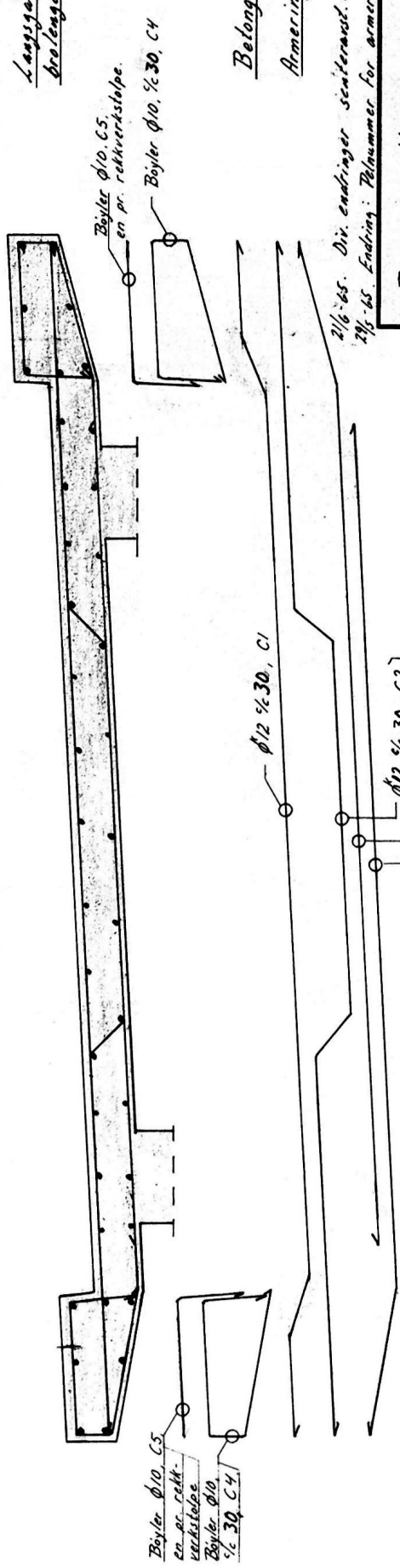


Armering brobane med symmetrisk takfall
 Pel 62 + 90 - pel 72 + 10 M. 1/20

Ø12 1/2 36, C2 }
 Ø12 1/2 36, C3 } Vekslende 1/2 12
 Ø12 1/2 36, C3 }

Betongoverdeknning:

/ overkant : 40mm
 / underkant + sider : 20mm.



Armering brobane med dosering M. 1/20
 Pel 61 + 05 - pel 62 + 90 og Pel 72 + 10 - pel 76 + 50

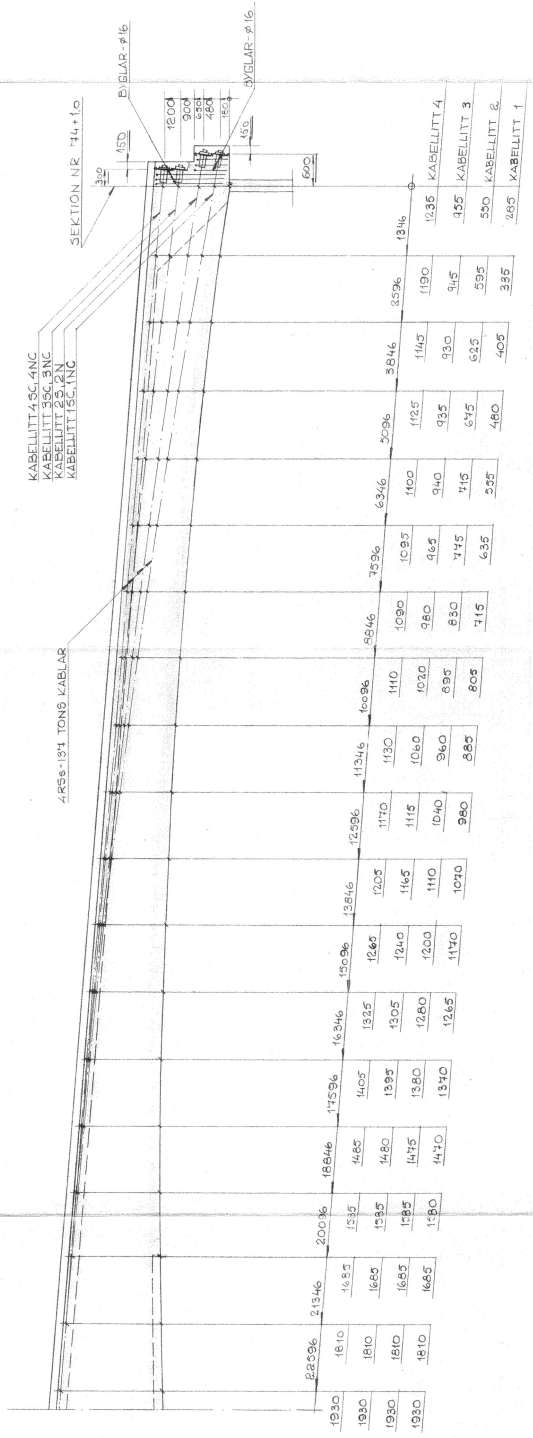
Laggende armering hele brolangden:
 / gøybner 2.7 - 14p/10
 / fjærebane 24 Ø12.

Betong i dekket: B400
Armering: Ks. 40 og st. 00.

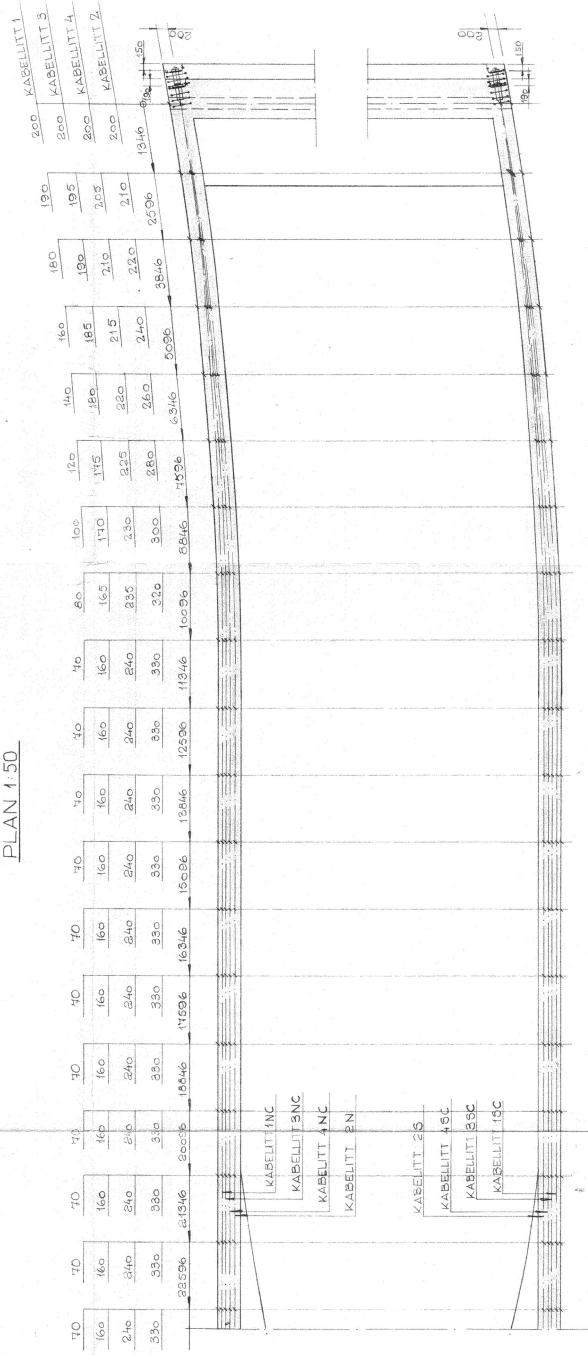
21/6-65. Div. endringer senterst. m.m. - pelnummer, stk.
 29/5-65. Endring: Pelnummer for armering i tverrfall, bøyings stk.

Målestokk	Tegn. 1/5-65	Stk.
	Trec. 1/5-65	Stk.
	Rt.	Stk.
Erstatning for: 7559-5 og 7559-6		
Bro over Herøysundet Armering brodekke		7559 - 56
Bodø 18.5-1965 INGENIØR PER GULBRANSEN A/S E. Gulbransen		Erstatte av:

LÄNGDSEKTION 1:50



PLAN 1:50



ANMÄRKNING

BETONG:

- I HITTSPANNET BTG K 400
- I ÄNDSPANNEN BTG K 450 MIN
- MÄTT I BRONS LÄNGDIRIKTNING MÄTES
- LÄNGS U.K. FARBANNEPLATTA
- MÄTT I HÖJDLID FRÅN U.K. HUVUDBALK
- TILL CENTRUM KABEL.

BETECKNINGAR

- STÖTFLUGE
- RÖRLIG FÖRBÄNDRING TYP R-137
- SKARVKOPPLING TYP S65-107
- BÄNKARE TYP FB-137

BETR. KOORDINATER TILL BRON SE
INGENJÖR PER GULBRANSEN A/S
RITN. NR. 7599-2A
KABELPLACERINGEN ÄR SYMMETRISK I
BÅDA HUVUDBALKARNA

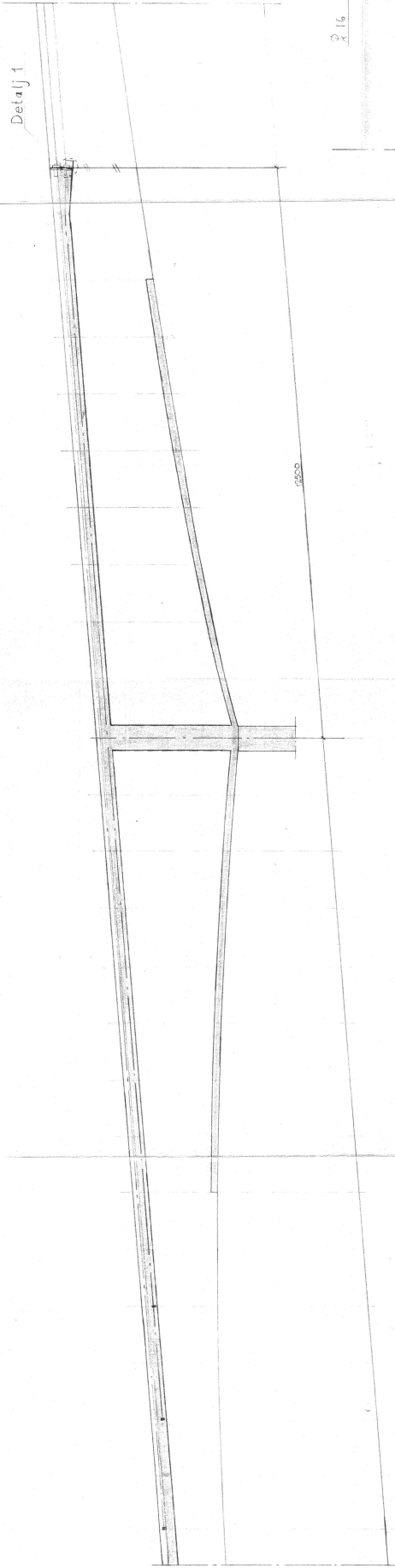
BRÖ ÖVER HERÖYSUNDET
KABELPLACERING I HUVUDBALKAR

AB STRÅNDBETONG
Västra
Kungälv
412 00
031 43 10 00

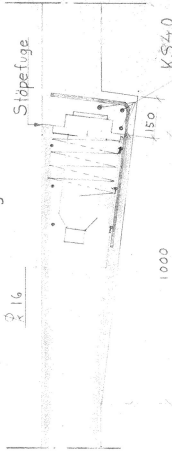
KABELCOORDINATER
KABELHÖJDLID
KABELLÖSLAST

STHJ 04-77-19-1004
RITN. NR. 65-4604-2
RITN. NR. 65-4604-3

LÅNGDSEKTION C-C, 1:50

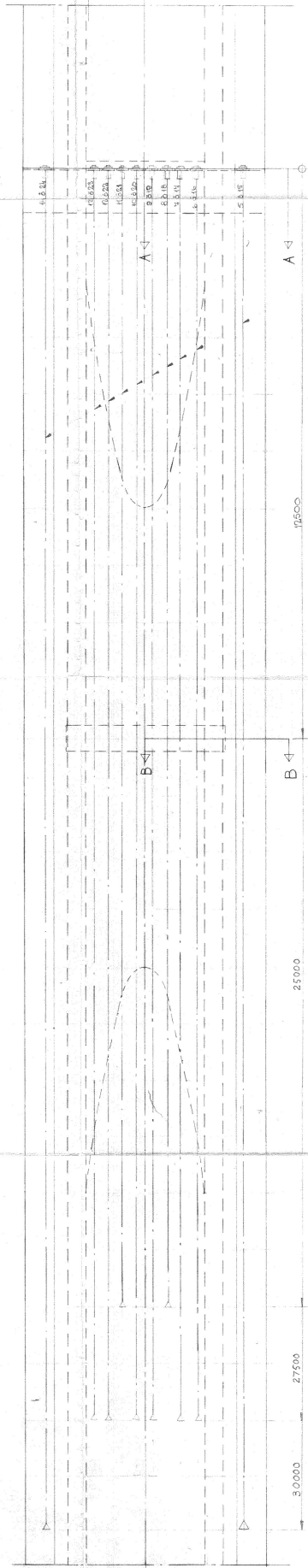


Detalj 1, 1:110



En byggl placeras mellan varje stödpatta

PLAN, 1:50



B-B, 1:10

A-A, 1:10

RFb-137

Bueankret för list 1:10 legges skrävt i platen

KABELLIT 5-14 PLACERAS ÖVER STÖD SEKTION NE 65*10
 KABELLIT 15-24 PLACERAS ÖVER STÖD SEKTION NE 74*10
 TEXT: ÖVDET SE RITNNE 65-4604-2

-// -// Slöjpfuge

Text, se rit nr 65-4604-2

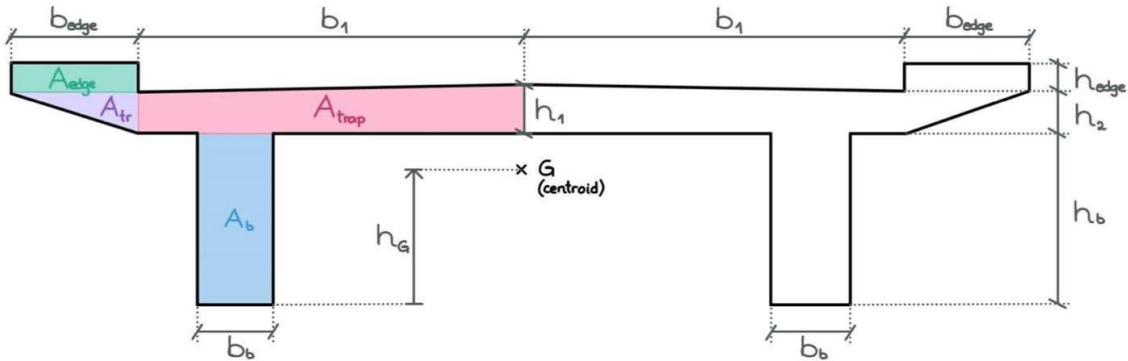
AS STÅNGBENTONG	Stångbentong AB	Stångbentong AB	Stångbentong AB	Stångbentong AB	Stångbentong AB	Stångbentong AB	Stångbentong AB	Stångbentong AB	Stångbentong AB
STÅNGBENTONG	STÅNGBENTONG	STÅNGBENTONG	STÅNGBENTONG	STÅNGBENTONG	STÅNGBENTONG	STÅNGBENTONG	STÅNGBENTONG	STÅNGBENTONG	STÅNGBENTONG

BRO ÖVER HERÖYSUNDET
 Kablar i platta över stöd

Stångbentong AB
 RITN. NR. 65-4604-2
 Utskrift från rit nr 65-4604-2
 T. Lindstrand

B Cross-Section Parameters

This worksheet shows the cross section parameters for a section in the middle of the main span.



$$\begin{aligned} h_1 &:= 230 \text{ mm} \\ h_2 &:= 200 \text{ mm} \\ h_{edge} &:= 200 \text{ mm} \end{aligned}$$

$$\begin{aligned} b_1 &:= 2000 \text{ mm} \\ b_b &:= 400 \text{ mm} \\ b_{edge} &:= 650 \text{ mm} \end{aligned}$$

$$hyp := \sqrt{b_1^2 + (h_1 - h_2)^2} = 2000.22 \text{ mm}$$

The height of the beam, which is varying along the entire bridge length:

$$h_b := 1200 \text{ mm} - h_1 = 970 \text{ mm}$$

Calculation of the cross section area:

$$A_b := h_b \cdot b_b$$

$$A_{trap} := \frac{(h_1 + h_2) \cdot b_1}{2}$$

$$A_{tr} := \frac{1}{2} \cdot h_2 \cdot b_{edge}$$

$$A_{edge} := h_{edge} \cdot b_{edge}$$

$$A_c := 2 \cdot (A_{trap} + A_b + A_{edge} + A_{tr}) = 2756000 \text{ mm}^2$$

Circumference:

$$u := 4 \cdot h_b + 2 \cdot b_1 + 2 \cdot (hyp + b_{edge} + 2 \cdot h_{edge} + \sqrt{h_2^2 + b_{edge}^2}) = 15341 \text{ mm}$$

Centroid location, calculated from the bottom of the cross section:

$$h_G := \frac{2 \left(A_b \cdot \frac{h_b}{2} + A_{trap} \cdot \left(h_b + \frac{h_2}{2} + \frac{h_1 - h_2}{3} \right) + A_{tr} \cdot \left(h_b + \frac{h_2}{3} \right) + A_{edge} \cdot \left(h_b + h_2 + \frac{h_{edge}}{2} \right) \right)}{A_c}$$

$$h_G = 642 \text{ mm}$$

C Calculation of Loads

Appendix C includes important load calculations that are relevant to the analysis. Specifically, it provides calculations for the shrinkage strain and creep effect.

C.1 Calculation of the Shrinkage Strain

The total shrinkage strain is calculated according to clause 3.1.4(6) of Eurocode 2.

Characteristic compressive strength of concrete (MPa):	$f_{ck} := 28$
Mean compressive strength (MPa):	$f_{cm} := f_{ck} + 8 = 36$
Ambient relative humidity (%):	$RH := 80$
Coefficients dependent on the type of cement:	$\alpha_{ds1} := 4$ $\alpha_{ds2} := 0.12$
Concrete age (days) at the beginning of drying shrinkage:	$t_s := 14$
Concrete age at the moment considered, in days:	$t := 57 \cdot 365 = 20.805 \cdot 10^3$
Concrete cross-sectional area (mm ²):	$A_c := 2756000$
The part of the cross section perimeter exposed to drying:	$u := 15341$
The notional size (mm) of the cross-section:	$h_0 := \frac{2 \cdot A_c}{u} = 359.299$

The basic drying shrinkage strain ϵ_{cd_0} is calculated in accordance with Annex B.2 in Eurocode 2:

$$\beta_{RH} := 1.55 \cdot \left(1 - \left(\frac{RH}{100}\right)^3\right) = 756.4 \cdot 10^{-3}$$
$$\epsilon_{cd_0} := 0.85 \cdot \left((220 + 110 \cdot \alpha_{ds1}) \cdot e^{-\alpha_{ds2} \cdot \frac{f_{cm}}{10}} \right) \cdot 10^{-6} \quad \beta_{RH} = 275.486 \cdot 10^{-6}$$

Calculation of the drying shrinkage ϵ_{cd}

$$k_h := 0.85 + \frac{h_0 - 200}{300 - 200} \cdot (0.75 - 0.85) = 0.691$$

The k_h coefficient depending on the notional size h_0 is found by interpolation of values provided in Table 3.3.

$$\beta_{ds} := \frac{t - t_s}{t - t_s + 0.04 \cdot \sqrt{h_0^3}} = 987.067 \cdot 10^{-3}$$

$$\epsilon_{cd} := \beta_{ds} \cdot k_h \cdot \epsilon_{cd_0} = 187.817 \cdot 10^{-6}$$

Calculation of the autogenous shrinkage strain ϵ_{ca}

$$\beta_{as} := 1 - e^{-0.2 \cdot t^{0.5}} = 1000 \cdot 10^{-3}$$

$$\epsilon_{ca_inf} := 2.5 \cdot (f_{ck} - 10) \cdot 10^{-6} = 45 \cdot 10^{-6}$$

$$\epsilon_{ca} := \beta_{as} \cdot \epsilon_{ca_inf} = 45 \cdot 10^{-6}$$

The total shrinkage strain: $\epsilon_{cs} := \epsilon_{cd} + \epsilon_{ca} = 233 \cdot 10^{-6}$

C.2 Creep Effect

On this sheet, the creep coefficient and effective modulus of elasticity are calculated for the permanent load/self weight and post-tensioning load according to Annex B.1 of Eurocode 2.

$$E_{cm} \equiv 32300 \text{ MPa}$$

Calculation of the creep coefficient $\varphi(t, t_0)$

Mean compressive strength in MPa:

$$f_{cm} := 28 + 8 = 36$$

Concrete age at loading in days:

$$t_0 := 14$$

Concrete age in days at the moment considered:

$$t := 57 \cdot 365 = 2.081 \cdot 10^4$$

Ambient relative humidity (%):

$$RH := 80$$

Concrete cross-sectional area (mm²):

$$A_c := 2756000$$

The perimeter of the member in contact with the atmosphere:

$$u := 15341$$

The notional size (mm) of the cross-section:

$$h_0 := \frac{2 \cdot A_c}{u} = 359.299$$

Coefficients to consider the influence of the concrete strength:

$$\alpha_1 := \left(\frac{35}{f_{cm}} \right)^{0.7} = 0.98$$

$$\alpha_2 := \left(\frac{35}{f_{cm}} \right)^{0.2} = 0.994$$

$$\alpha_3 := \left(\frac{35}{f_{cm}} \right)^{0.5} = 0.986$$

$$\varphi_{RH} := \left(1 + \frac{1 - \frac{RH}{100}}{0.1 \cdot \sqrt[3]{h_0}} \cdot \alpha_1 \right) \cdot \alpha_2 = 1.269$$

$$\beta_H := 1.5 \cdot (1 + (0.012 \cdot RH)^{18}) \cdot h_0 + 250 \cdot \alpha_3 = 1.044 \cdot 10^3$$

$$\beta_c := \left(\frac{t - t_0}{\beta_H + t - t_0} \right)^{0.3} = 0.985$$

$$\beta_1 := \frac{16.8}{\sqrt{f_{cm}}} = 2.8$$

$$\beta_2 := \frac{1}{0.1 + t_0^{0.20}} = 0.557$$

$$\varphi := \varphi_{RH} \cdot \beta_1 \cdot \beta_2 \cdot \beta_c = 1.95$$

The effective modulus of elasticity:

$$E_{c_eff} := \frac{E_{cm}}{1 + \varphi} = 10950 \text{ MPa}$$

D Calculation of Prestress Losses

Appendix D includes the calculation of prestress losses caused by steel relaxation and elastic shortening. It should be noted that the calculation of the prestress loss due to elastic shortening in this appendix pertains to the tendons assumed to experience the maximum elastic shortening.

D.1 Relaxation

The relaxation loss is calculated according to Eurocode 2, clause 3.3.2.

Characteristic value of the tensile strength of the prestressing steel:

$$f_{pk} := 1770 \text{ MPa}$$

Characteristic 0.2 % proof-stress:

$$f_{p0.2k} := 1570 \text{ MPa}$$

Characteristic 0.1 % proof-stress:

$$f_{p0.1k} := 1670 \text{ MPa}$$

Cross sectional area of a tendon:

$$A_p := 1244 \text{ mm}^2$$

Jacking force:

$$\sigma_{p,max} := 0.7 \cdot f_{p0.2k} = 1099 \text{ MPa}$$

The initial prestress:

$$\sigma_{pi} := \sigma_{p,max} = 1099 \text{ MPa}$$

Time (in hours) after tensioning:

$$t := 57 \cdot 365 \cdot 24 = 499320$$

Relaxation loss 1000 hours after post-tensioning:

$$\rho_{1000} := 8$$

$$\mu := \frac{\sigma_{pi}}{f_{pk}}$$

The relaxation loss for a time t equal to 57 years:

$$\Delta\sigma_{pr,max} := 5.39 \cdot \rho_{1000} \cdot e^{6.7 \cdot \mu} \cdot \left(\frac{t}{1000}\right)^{0.75 \cdot (1 - \mu)} \cdot 10^{-5} \cdot \sigma_{pi} = 178 \text{ MPa}$$

According to clause 5.10.6 (1) of Eurocode 2, the prestress loss due to relaxation should be reduced by a factor 0.8 in order to account for the relaxation of steel being dependent on the concrete deformation due to creep and shrinkage.

$$\Delta\sigma_{pr} := 0.8 \cdot \Delta\sigma_{pr,max} = 142 \text{ MPa}$$

D.2 Elastic Shortening

Mean value of concrete cylinder compressive strength:	$f_{cm} \equiv 36 \text{ MPa}$
Secant modulus of elasticity of concrete:	$E_{cm} \equiv 32300 \text{ MPa}$
Cross-sectional area of concrete:	$A_c := 2070000 \text{ mm}^2$
Design value of modulus of elasticity of prestressing steel:	$E_p := 205000 \text{ MPa}$
The jacking force:	$P_{max} := 1370 \text{ kN}$
Number of tendons:	$n := 18$
Coefficient dependent on the cement type:	$s := 0.25$
Instant in time of the first loading:	$t_0 := 14$
Age of the concrete in days:	$t := t_0 = 14$

The mean concrete compressive strength and the secant modulus of elasticity at an concrete age of 14 days, which is time where the prestressing force is applied:

$$f_{cm,t} := f_{cm} \cdot e^{s \cdot \left(1 - \left(\frac{28}{t}\right)^{\frac{1}{2}}\right)} = 32.5 \text{ MPa}$$
$$E_{cm,t} := \left(\frac{f_{cm,t}}{f_{cm}}\right)^{0.3} \cdot E_{cm} = 31312 \text{ MPa}$$
$$E_{cm,0} := E_{cm,t} = 31312 \text{ MPa}$$

The average prestress loss in the tendons located in a section located above the main piers, i.e., at axis 4 and 5:

$$\Delta\sigma_{pe} := \frac{(n-1)}{2n} \cdot \frac{E_p}{E_{cm,0}} \cdot \frac{18 P_{max}}{A_c} = 36.8 \text{ MPa}$$

E Transfer of Prestress - Transmission Length

The transfer of prestress for tendon 4NB is calculated according to clause 8.10.2.2 of Eurocode 2.

Calculation of the constant bond stress, f_{bpt}

Concrete age, in days:	$t := 57 \cdot 365 = 2.081 \cdot 10^4$
Characteristic compressive strength of concrete, in MPa:	$f_{ck} := 28$
Mean value of axial tensile strength of concrete:	$f_{ctm} := 0.3 \cdot f_{ck}^{2 \div 3} = 2.8$
Partial factor for concrete:	$\gamma_c := 1.5$
Cross section area of tendon, in mm ² :	$A_p := 1244$

Coefficients:

Effects on tensile strength:	$\alpha_{ct} := 0.85$
Type of cement (Class N):	$s := 0.25$
Tendon type:	$\eta_{p1} := 3.2$
Not good bond conditions:	$\eta_1 := 0.7$
After 28 days:	$\alpha := 2 \div 3 = 0.667$

Design tensile value of strength at time of release, $f_{ctd}(t)$, in MPa:

$$\beta_{cc} := e^{s \cdot \left(1 - \left(\frac{28}{t}\right)^2\right)} = 1.3$$

$$f_{ctm,t} := (\beta_{cc})^\alpha \cdot f_{ctm} = 3.2$$

$$f_{ctd,t} := \alpha_{ct} \cdot 0.7 \cdot \frac{f_{ctm,t}}{\gamma_c} = 1.3$$

The bond stress, in MPa: $f_{bpt} := \eta_{p1} \cdot \eta_1 \cdot f_{ctd,t} = 2.9$

Calculation of the basic value of the transmission length, l_{pt}

Sudden release:	$\alpha_1 := 1.25$
Strands:	$\alpha_2 := 0.19$
Nominal diameter of tendon, approximated by:	$\phi := 2 \cdot \sqrt{\frac{A_p}{\pi}} = 39.8$
Tendon stress at release, in MPa:	$\sigma_{pm0} := 873$

Basic transmission length, in meter:

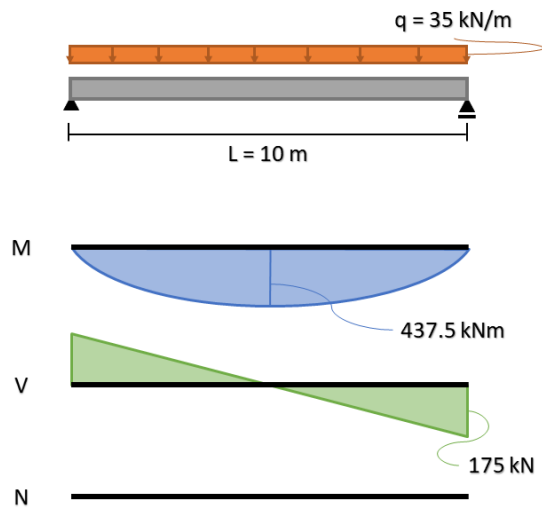
$$l_{pt} := \alpha_1 \cdot \alpha_2 \cdot \phi \cdot \frac{\sigma_{pm0}}{f_{bpt}} \cdot \frac{1}{1000} = 2.9$$

The design value, in meter: $l_{pd2} := 1.2 \cdot l_{pt} = 3.4$

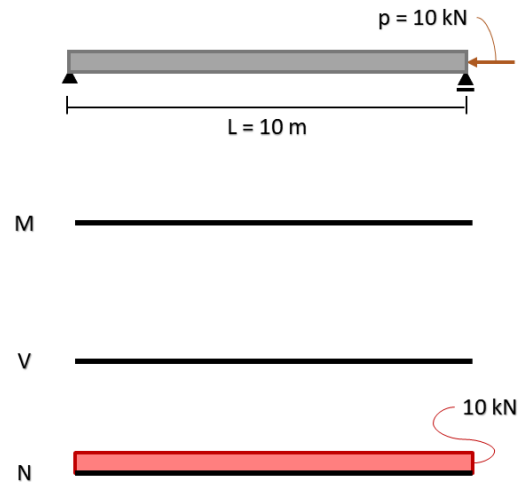
F Simple Beam - Cross-Section Forces

This appendix presents the load effects on a simply supported beam under different load cases.

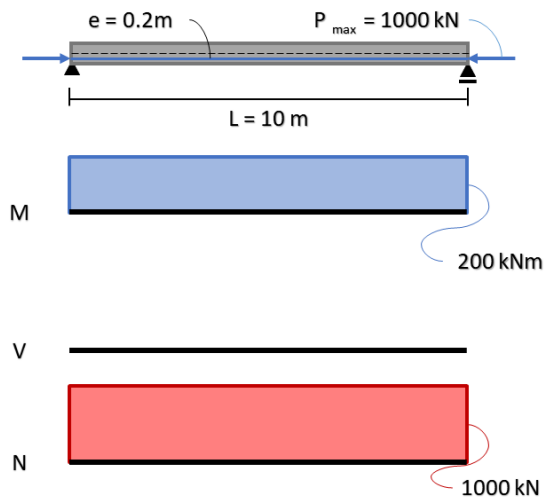
Distributed Load



Axial Load



Post-Tension Load



G The Python Script for the Post-tensioning System

Here, the Python script that effectively models the post-tensioning system is provided. It encompasses the implementation and application of the script specifically to tendon 1NA and 1NB. An example is given to demonstrate the removal of the central 10 m of tendon 1NB in the model, from $x = 55\text{m}$ to $x = 65\text{m}$.

```
import csv
import math
#####
#Specify where the placement of your script is:
#Add a folder called "TendonLayouts" in this place,
#containing csv. files with the coordinates for the tendons
work_directory = "C:/Users/simen/OneDrive - NTNU/V2023/Finished Model/"
#####

###GEOMETRIES
#Holding different geometries
geometries = {}

###CLASSES
#Class defining a tendon with coordinates
class Tendon:
    def __init__(self, name, coordinateList, anchoredLeft, anchoredRight, area,
↵ load):
        self.frictionCoefficient = 0.2
        self.wobbleFactor = 2*10**(-6) + averageChangeInAngle(coordinateList)
        self.retentionLength = 0
        self.load = load
        self.name = name
        self.coordinateList = coordinateList
        self.anchoredLeft = anchoredLeft
        self.anchoredRight = anchoredRight
        self.endPoints = [coordinateList[0],coordinateList[-1]]
        self.area = area
        self.materialName = "Prestress-Steel"
        self.loadSetName = "Post-tension"
        self.drawTendon() # Drawing tendon
        self.applyParameters() # Applying parameters
        self.loadTendon() # Applying load

# Making geomtry of tendon
def drawTendon(self):
    if(len(self.coordinateList) == 2):
        createLine(self.name,self.coordinateList[0],self.coordinateList[1])
    else:
        createCurve(self.name,self.coordinateList)

# Assigning parameters to the tendon, geometry and material
def applyParameters(self):
```

```

if(not self.area in geometries):
    tendonGeometryName = "Tendon "+str(self.area)+"mm^2"
    geometries[self.area] = tendonGeometryName
    addGeometry(tendonGeometryName, "RELIN", "REBAR", [])
    setParameter( "GEOMET",tendonGeometryName, "REIEMB/CROSSE",self.area)
    setParameter( "GEOMET",tendonGeometryName, "REIEMB/RDITYP", "RCROSS"
        ↪ )
    setShapeType( "REINFORCEMENTSHAPE", self.name )
    setReinforcementType( "REINFORCEMENTSHAPE", self.name, "BAR" )
    assignMaterial(self.materialName, "REINFORCEMENTSHAPE", [ self.name ] )
    assignGeometry(geometries[self.area], "REINFORCEMENTSHAPE", [self.name] )

# Assigning a post-tension load to the tendon
def loadTendon(self):
    if(self.anchoredLeft or self.anchoredRight):
        loadName = "Post-tension load "+self.name
        createShapeLoad(loadName, self.loadSetName )
        setParameter( "GEOMETRYLOAD", loadName, "LODTYP", "POSTEN" )
        if(self.anchoredLeft and self.anchoredRight):
            setParameter( "GEOMETRYLOAD", loadName, "POSTEN/BOTHEN/FORCE1",
                ↪ self.load )
            setParameter( "GEOMETRYLOAD", loadName, "POSTEN/BOTHEN/FORCE2",
                ↪ self.load )
            setParameter( "GEOMETRYLOAD", loadName, "POSTEN/BOTHEN/RETLE1",
                ↪ self.retentionLength )
            setParameter( "GEOMETRYLOAD", loadName, "POSTEN/BOTHEN/RETLE2",
                ↪ self.retentionLength )
            attachTo( "GEOMETRYLOAD", loadName, "POSTEN/BOTHEN/PNTS1",
                ↪ self.name, [ self.endPoints[0] ] )
            attachTo( "GEOMETRYLOAD", loadName, "POSTEN/BOTHEN/PNTS2",
                ↪ self.name, [ self.endPoints[1] ] )
        elif(self.anchoredLeft and not self.anchoredRight):
            setParameter( "GEOMETRYLOAD", loadName, "POSTEN/TENTYP", "ONEEND"
                ↪ )
            setParameter( "GEOMETRYLOAD", loadName, "POSTEN/ONEEND/FORCE1",
                ↪ self.load )
            setParameter( "GEOMETRYLOAD", loadName, "POSTEN/ONEEND/RETLE1",
                ↪ self.retentionLength )
            attachTo( "GEOMETRYLOAD", loadName, "POSTEN/ONEEND/PNTS1",
                ↪ self.name, [ self.endPoints[0] ] )
        elif(not self.anchoredLeft and self.anchoredRight):
            setParameter( "GEOMETRYLOAD", loadName, "POSTEN/TENTYP", "ONEEND"
                ↪ )
            setParameter( "GEOMETRYLOAD", loadName, "POSTEN/ONEEND/FORCE1",
                ↪ self.load )
            setParameter( "GEOMETRYLOAD", loadName, "POSTEN/ONEEND/RETLE1",
                ↪ self.retentionLength )
            attachTo( "GEOMETRYLOAD", loadName, "POSTEN/ONEEND/PNTS1",
                ↪ self.name, [ self.endPoints[1] ] )
    else:

```

```

        return False
    setParameter( "GEOMETRYLOAD", loadName, "POSTEN/SHEAR",
        ↪ self.frictionCoefficient )
    setParameter( "GEOMETRYLOAD", loadName, "POSTEN/WOBBLE",
        ↪ self.wobbleFactor )
    attach( "GEOMETRYLOAD", loadName, [ self.name ] )

### FUNCTIONS
# Functions to calculate average angle change
def dotProduct(v1,v2):
    d = 0
    for i in range(len(v1)):
        d += v1[i]*v2[i]
    return d

def vecMagnitude(v):
    a = 0
    for i in range(len(v)):
        a += v[i]**2
    return a**(1/2)

def vecAngle(v1,v2):
    cos_φ = dotProduct(v1, v2)/(vecMagnitude(v1)*vecMagnitude(v2))
    return math.acos(cos_φ)

def averageChangeInAngle(lst):
    angleSum = 0
    distance = 0
    if(len(lst)<=2):
        return 0
    else:
        for i in range(len(lst)-2):
            vec1 = [lst[i+1][0]-lst[i][0], lst[i+1][1]-lst[i][1],
                ↪ lst[i+1][2]-lst[i][2]]
            vec2 = [lst[i+2][0]-lst[i+1][0], lst[i+2][1]-lst[i+1][1],
                ↪ lst[i+2][2]-lst[i+1][2]]
            distance += vec1[0]
            angleSum += vecAngle(vec1,vec2)
        distance += vec2[0]
    return angleSum/distance

# Function to read csv file containing coordinates
def readCoordinatesToListFromCsv(filename):
    rows = []
    with open (filename) as file:
        reader = csv.reader(file)
        for row in reader:
            rows.append(row)
    # Removing headers

```

```

dataSet = rows[1:]
# Making values to float
coordinates = []
for row in dataSet:
    c = []
    for i in row:
        c.append(float(i))
    coordinates.append(c)
return coordinates

# Function to get coordinate between two points at given x value
def getCoordinateBetween(c1,c2,x):
    y = (x-c1[0])*(c2[1]-c1[1])/(c2[0]-c1[0])+c1[1]
    z = (x-c1[0])*(c2[2]-c1[2])/(c2[0]-c1[0])+c1[2]
    return [x,y,z]

# Function to add a coordinate to a list according to its x value
def addPlaceToList(lst,xValue):
    new_lst = lst
    for i in range(len(new_lst)):
        xCor = lst[i][0]
        if(xCor > xValue):
            new_lst.insert(i,getCoordinateBetween(lst[i-1], lst[i], xValue))
            return new_lst
        if(xCor == xValue):
            return new_lst

# Function checking if two lists are equal
def isTwoListEqual(lst1,lst2):
    if(len(lst1) == len(lst2)):
        for i in range(len(lst1)):
            if(not lst1[i] == lst2[i]):
                return False
    else:
        return False

    return True

# Function to make tendons from a file containing

def makeTendonsFromFile(filename, tendonName, remove, leftAnchor, rightAnchor,
↪ area, load):
    # Makes coordinates from file
    lst = readCoordinatesToListFromCsv(filename)
    startPt = lst[0]
    endPt = lst[-1]
    # List of tendons
    tendons = []

    # Undamaged tendon, giving only one segment

```

```

if(remove == None):
    tendons.append(Tendon(tendonName, lst, leftAnchor, rightAnchor, area,
        ↪ load))
# Damaged tendon, giving multiple segments
else:
    # Adding damaged areas to the list
    flat_remove = [item for sublist in remove for item in sublist]
    for value in flat_remove:
        lst = addPlaceToList(lst, value)

    damaged = False
    cableNr = 1

    coordinateList = []
    # Iterating coordinate list
    for i in range(len(lst)):
        # LOCATION: not damaged
        if(not damaged):
            # encounters damaged area
            if(lst[i][0] in flat_remove):
                coordinateList.append(lst[i])
                if(len(coordinateList)>1):
                    partName = tendonName+" Part "+str(cableNr)
                    # Left side not original anchored
                    if not isTwoListEqual(coordinateList[0], startPt):
                        # Right side not original anchored
                        if not isTwoListEqual(coordinateList[-1], endPt):
                            tendons.append(Tendon(partName, coordinateList,
                                ↪ False, False, area, load))
                        # Right side original anchored
                        else:
                            tendons.append(Tendon(partName, coordinateList,
                                ↪ False, rightAnchor, area, load))
                    # Left side original anchored
                else:
                    # Right side not original anchored
                    if not isTwoListEqual(coordinateList[-1], endPt):
                        tendons.append(Tendon(partName, coordinateList,
                            ↪ leftAnchor, False, area, load))
                    # Right side original anchored
                    else:
                        tendons.append(Tendon(partName, coordinateList,
                            ↪ leftAnchor, rightAnchor, area, load))
                    cableNr += 1
                    coordinateList = []
                    damaged = True
                    # still healthy tendon
                else:
                    coordinateList.append(lst[i])
            # LOCATION: damaged

```

```

else:
    # encounters healthy area
    if(lst[i][0] in flat_remove):
        coordinateList.append(lst[i])
        damaged = False
#If there is still coordinates that have not made cabel
if(len(coordinateList)>1):
    partName = tendonName+" Part "+str(cableNr)
    # left side not original anchored
    if not isTwoListEqual(coordinateList[0], startPt):
        # Right side not original anchored
        if not isTwoListEqual(coordinateList[-1], endPt):
            tendons.append(Tendon(partName, coordinateList, False, False,
                ↪ area, load))
        # Right side original anchored
    else:
        tendons.append(Tendon(partName, coordinateList, False,
            ↪ rightAnchor, area, load))
# Left side original anchored
else:
    # Right side not original anchored
    if not isTwoListEqual(coordinateList[-1], endPt):
        tendons.append(Tendon(partName, coordinateList, leftAnchor,
            ↪ False, area, load))
    # Right side original anchored
    else:
        tendons.append(Tendon(partName, coordinateList, leftAnchor,
            ↪ rightAnchor, area, load))

#Model without post tension
openProject( "C:/Users/simen/OneDrive - NTNU/V2023/Finished Model/Post-tension No
↪ 4NB/HeroeysundBridge_Missing4NB.dpf" )

### Losses due to elastic shortening and relaxation
# Losses for central tendons
dP_mid = 195.7 * 10**3 #Including elastic shortening and relaxation
# Losses for not central tendons
dP_rest = 222.6 * 10**3 #Including elastic shortening and relaxation
# Losses for tendons in piers
dP_piers = 88.4 * 10**3 #Including relaxation

addSet( "SHAPESET", "Post-tension tendons beam" )

#####
##### NORTH BEAM #####
#####

# Properties

```

```
P = 1370*10**3 #[N]
tendonCrossSectionArea = 1244 #[mm^2]

### Cable 1N
cableNumber = "1N"

## 1NA
segment = "A"
name = "Cable_"+cableNumber+segment
filename = work_directory+"TendonLayouts/"+name+"_Coordinates.csv"
remove = None #None or 2d list
makeTendonsFromFile(filename, name, remove, True, False,
→ tendonCrossSectionArea,P-dP_rest)

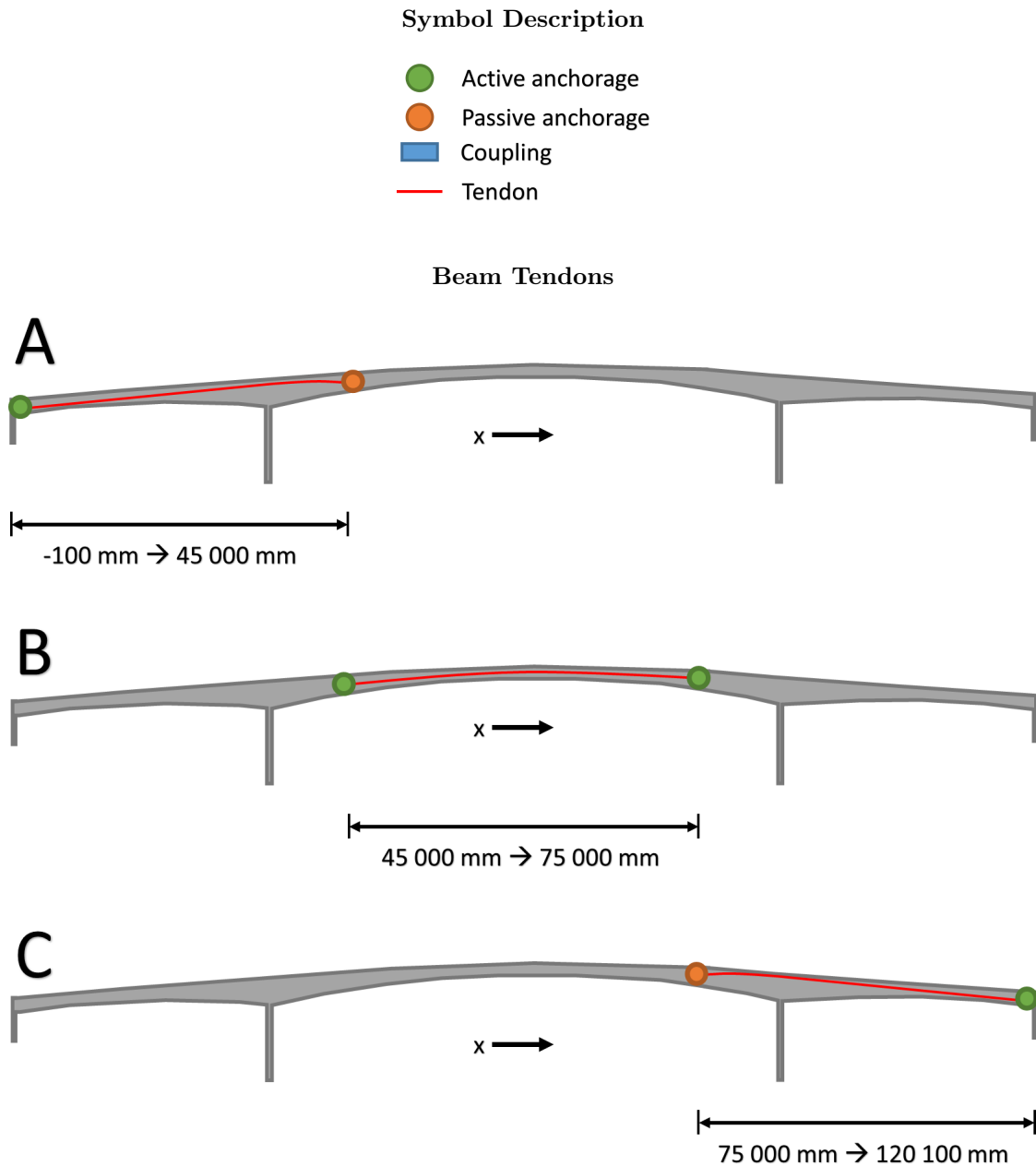
## 1NB
segment = "B"
name = "Cable_"+cableNumber+segment
filename = work_directory+"TendonLayouts/"+name+"_Coordinates.csv"
remove = [[55 000, 65 000]] #None or 2d list
makeTendonsFromFile(filename, name, remove, True, True,
→ tendonCrossSectionArea,P-dP_mid)
```

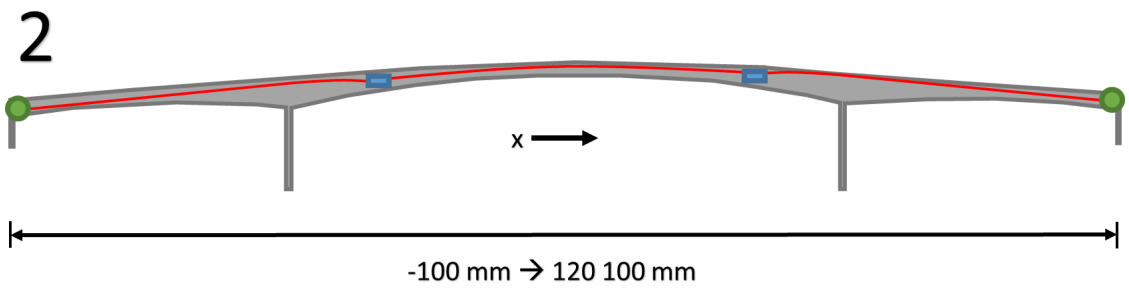
H Reference System for the Post-Tensioning System

Appendix H provides a description and visualization of the reference system used for the post-tensioning system in the bridge model. This reference system is important for accurately removing tendon segments in the model. While the original bridge drawings have their own coordinate systems, the model adopts a modified coordinate system to enhance user intuitiveness. The reference system presented in this appendix indicates the range of x -values for each tendon in the beams.

In the figures below, it can be observed that the bridge starts at $x = -100$ mm and ends at $x = 120\ 100$ mm. This range includes the complete thickness of the outward piers, as the original coordinate system begins and ends in the middle of the piers.

Tendon 1N/1S, 3N/3S, and 4N/4S are divided into three segments labeled as A, B, and C, while tendon 2N/2S consists of a continuous cable.







 **NTNU**

Norwegian University of
Science and Technology